Absorptive optical non-linearities using Rydberg excitations in a Cavity

Rajiv Boddeda

▶ **To cite this version:**

Rajiv Boddeda. Absorptive optical non-linearities using Rydberg excitations in a Cavity. Optics [physics.optics]. Université Paris Saclay (COmUE), 2016. English. ⟨NNT : 2016SACLO021⟩. ⟨tel-01482321⟩

HAL Id: tel-01482321

https://pastel.hal.science/tel-01482321v1

Submitted on 3 Mar 2017

HAL is a multi-disciplinary open access archive for the deposit and dissemination of scientific research documents, whether they are published or not. The documents may come from teaching and research institutions in France or abroad, or from public or private research centers.

L'archive ouverte pluridisciplinaire **HAL**, est destinée au dépôt et à la diffusion de documents scientifiques de niveau recherche, publiés ou non, émanant des établissements d'enseignement et de recherche français ou étrangers, des laboratoires publics ou privés.

HAL Authorization

NNT : 2016SACLO021

THESE DE DOCTORAT
DE L'UNIVERSITE PARIS-SACLAY

préparée à

L'INSTITUT D'OPTIQUE GRADUATE SCHOOL

ÉCOLE DOCTORALE N°572
Ondes et Matière (EDOM)

Spécialité de doctorat : Physique

par

Rajiv BODDEDA

Absorptive optical non-linearities using Rydberg excitations in a cavity

Thèse présentée et soutenue à Palaiseau, le 19 Décembre 2016

Composition du jury :

M. Jean-François Roch	Président du jury	Université d'Orsay
M. Michel Brune	Rapporteur	Collège de France, Paris
M. Aurélien Romain Dantan	Rapporteur	Aarhus University, Denmark
M. Alberto Bramati	Examinateur	Université Pierre et Marie Curie
M. Philippe Grangier	Directeur de thèse	Institut d'Optique

Acknowledgments

First of all, I would like to thank my family, particularly my brother, for always encouraging me in my pursuit of an academic career. I am very thankful to the foundation of École Polytechnique for sponsoring my master studies and especially François Hache for being a great mentor during the course of two years. It was a tough decision to come to a non-Anglophonic country with a very knowledge. But it turned out to be one of the best decisions I have every made, I consider myself quite lucky to be trained under some of the best professors in the world. In addition, I've met some of the nicest people both inside and outside the university and made some very good friends.

I am very grateful to Philippe Grangier for giving me an opportunity to work on such an interesting experiment. I am very honored to work under Philippe whose genuine enthusiasm and enormous experience was necessary to keep our spirits up during the course of the three years of my PhD. Also the weekly meetings with Philippe, Andrey and Etienne helped me a lot to keep up with different theoretical models as well as the current progress in the field.

I would like to appreciate the time taken by Michel Brune, Aurélien Romain Dantan, Jean-François Roch and Alberto Bramati for being part of the jury. I am really grateful to them for evaluating my work and for their invaluable comments on my thesis.

I am quite fortunate to be part of such well versed experimental physicists like Alexei Ourjourmtsev and Erwan Bimbard. With the determined guidance and knowledge of both of them, I understood a great deal of both theoretical and experimental aspects of quantum optics. When I came to work at the institute as an internship student in 2013, the experiment seemed daunting but I felt very much at home with their guidance and patience in welcoming me. There were a number of days we spent late in the evening enthusiastically trying to fix various problems on the experiment which motivated me to further continue working on it for my thesis.

During the final days of the departure of Erwan and Alexei, Imam Usmani joined our team as a postdoc and was of a great help to fill the void. His distinct approach to solving problems and his enormous enthusiasm for sports was a welcoming change. We spent countless days struggling in the lab to make everything work. I would also like to thank Senka, who joined our team about an year ago and made an extensive contribution for the installation of the new cavity system. Her

hardworking nature and her organization skills were an important addition to our team. The experiment is now in the hands of Imam and Senka, I wish you both the very best in the future.

I would also like to acknowledge the quantum optics team for making my stay at Institut d'Optique so much more enjoyable. I am very grateful to Florence Nogrette, her technical expertise on many things related to the experiment were outstanding. In addition, her patience when it comes to listening to my terrible French. Merci Florence, Imam, Martin etc. Vous m'avez beaucoup aidé à apprendre la langue, la culture, l'histoire Française. I really appreciate the help of permanent members - Antoine Browaeys, Yvan Sortais, Thierry Lahaye et Rosa Tualle-Brouri who were always there to ansmer my questions about Physics or even about French culture. I would also like to thank Martin and Sylvain for the motivation to play basketball, a welcoming break from continuously working (Even though we lost most of the matches but the very few times we won was pretty great); Stephen Jennewein for always being there whenever I need to rant about the French bureaucracy; Mauro Persechino for his discussions on how to cook Italian food; Henning for his ever smiling face in the group. In addition, I would like to thank various members of the team with whom I interacted during my time at the institute Daniel Barredo, Guillaume Boucher, Melissa Ziebell, Bashkar Kanseri, Ludovic Brossard, Vincent Lienhard, Nicolas Vitrant, Jean Etesse, Sylvain Ravets, Tom Peyrot and various other people at Institut d'Optique. I know that you are all capable of wonderful things and I will always cherish the time spent with you guys. I wish you all good luck for your future in science and may the force be with you.

I would like to extend my gratitude to André Guilbaud, Patrick Roth, André Villing and Frédéric Moron from the mechanical and the electrical workshop who were very welcoming and always available whenever we needed them. I would also like to thank the administrative department both at the Institut d'Optique and at the École doctorale - Martine Basset, Nathalie Baudry, Charline Joli. It was also quite fun to work on something completely unrelated to science with Nicole Bidoit and her team for the mission doctorale.

Finally, I would like to thank all my friends from Paris: Satya, Anirudh, Kanna, Carolyna, Sviatoslav, Inna. I really enjoyed the countless number of occasions discussing about broad range of topics both inside and outside science. The things I learned from them made me a better person today. My best friend, Mafalda, I have no words to tell you how much I appreciate your presence during the course of my PhD. I have to thank you from the bottom of my heart for all your love and patience. You are my inspiration and you complete me.

Contents

Table of contents v

List of Figures xi

List of Tables xiii

1 Introduction 1

I Theoretical tools 9

2 Theoretical tools for Atom-Light coupling 11
2.1 Light propagation in a dielectric medium . . . 11
2.2 Semi-classical approach of the light-atom system . . . 12
2.3 Quantum mechanical approach . . . 15
2.3.1 Optical Bloch equations . . . 16
2.3.2 Optical bistability using two level atoms . . . 18
2.4 Three level atoms . . . 20
2.4.1 Electromagnetically Induced Transparency . . . 21
2.4.2 Linear response . . . 22
2.4.3 Multilevel system . . . 23
2.5 Non-linearity . . . 24

3 Rydberg-Rydberg Interactions 25
3.1 Introduction . . . 25
3.2 Mean field approach . . . 27
3.3 Rydberg bubble model . . . 28

II Experimental apparatus 31

4 Optical and control system 33
4.1 Trapping and excitation lasers . . . 33
4.2 Frequency stabilization system . . . 35
4.2.1 Transfer cavity . . . 36
4.2.2 Characterization tests . . . 38

4.2.3 Stability of lasers . . . 39
4.3 Control/Acquisition setup . . . 41
4.3.1 Hardware components . . . 41
4.3.2 Software . . . 41

5 Atomic setup **45**
5.1 Atom cloud preparation . . . 45
5.2 Magneto Optical Trap . . . 46
5.3 Low Velocity Intense Source (LVIS) . . . 47
5.4 Main atomic cloud . . . 48
5.4.1 Optical molasses . . . 49
5.4.2 Imaging system . . . 49
5.4.3 Temperature measurements . . . 51

6 Detection system **53**
6.1 Second order correlation measurement . . . 53
6.1.1 Photon statistics . . . 54
6.1.2 Experiment . . . 54
6.2 Homodyne Tomography . . . 56
6.2.1 Phase locked experimental setup . . . 58
6.2.2 Squeezing measurements in transmission . . . 61
6.3 Conclusion . . . 64

III Absorptive Rydberg Non-linearities **65**

7 Measurement of Absorptive Optical Non-linearities **71**
7.1 Main cavity . . . 72
7.2 Preparation of a small cloud . . . 77
7.2.1 Dipole traps . . . 77
7.2.2 Loading the traps . . . 78
7.3 Cooperativity measurement . . . 80
7.4 EIT in a cavity . . . 82
7.4.1 Blue cavity . . . 82
7.4.2 Linear regime . . . 86
7.4.3 Rydberg linewidth . . . 87
7.5 Non-linearity measurements . . . 88
7.5.1 Resonant nonlinearity with Rydberg S state . . . 88
7.5.2 Resonant non-linearity using Rydberg D states . . . 90
7.5.3 Dephasing in Rydberg D-States . . . 92
7.5.4 $\chi^{(3)}$ determination . . . 95
7.6 Conclusion . . . 95

8 Second order correlation effects **97**
8.1 Second order correlation function . . . 98
8.2 Photon statistics in continuous excitation limit . . . 100
8.2.1 Experimental implementation . . . 100
8.2.2 Photon counting measurements . . . 101

8.3 Squeezing measurements using theoretical model . . . 101
8.4 Squeezing measurements on experiment . . . 102
8.5 Conclusion . . . 104

Conclusion **106**

IV Towards Quantum Optical Non-linearities 107

9 Towards quantum optical non-linearities **109**
9.1 Introduction . . . 109
9.2 Quantum regime . . . 110
9.3 A new cavity system . . . 111
9.3.1 Design . . . 112
9.3.2 Installation and alignment of the cavity . . . 114
9.3.3 Characterization of the cavity . . . 115
9.4 Cooperativity and EIT measurements . . . 118
9.4.1 Cooperativity measurement . . . 118
9.4.2 EIT measurement . . . 118
9.5 Possible schemes to exploit . . . 119
9.5.1 Off-resonant excitation . . . 120
9.5.2 On-resonance excitation . . . 121
9.5.3 Cavity phase shift . . . 121
9.6 Photonic controlled-phase gate proposal . . . 123
9.7 Conclusion . . . 125

Conclusion and Outlook 126

V Appendices 129

A Fundamental constants and Energy levels of ^{87}Rb **131**
A.1 Fundamental constants . . . 131
A.2 ^{87}Rubidium reference . . . 131

B Rydberg atoms **133**

C Calculation of Stark shifts for D states **135**

D Wigner Function **137**

References and articles 139

Bibliography **139**

Author's Publications **149**

Abstract 151

List of Figures

1.1 Modular computing . . . 2
1.2 Quantum Control Z gate . . . 3
1.3 Rydberg-Rydberg interaction energy shift vs Interatomic distance . . . 5
1.4 A single photon filter using Rydberg excitations . . . 6

2.1 Two-level susceptibility . . . 13
2.2 Comparison of free space and cavity transmission . . . 14
2.3 Cooperativity measurement in absorptive and dispersive regime 17
2.4 Absorptive bi-stability . . . 18
2.5 Dispersive bistability . . . 19
2.6 EIT Susceptibility . . . 20
2.7 Comparision of two level and three level susceptibility . . . 21
2.8 Cavity vs Free space EIT . . . 22
2.9 Two-photon resonance response . . . 23

3.1 Quantized energy levels of Hydrogen-like atoms . . . 26
3.2 Rydberg-Rydberg Interactions . . . 27
3.3 Rydberg bubble . . . 29

4.1 Transfer cavity . . . 36
4.2 Laser system and the path various optical beams . . . 37
4.3 Locking schemes for the master laser using transfer cavity 38
4.4 Transfer Cavity Stability . . . 39
4.5 Blue laser frequency stability . . . 39
4.6 Schematics of the acquisition system . . . 42
4.7 Experimental sequence . . . 43

5.1 An illustration of LVIS and the main chamber . . . 46
5.2 MOT excitation scheme . . . 47
5.3 LVIS and MOT traps along with the atomic beam . . . 48
5.4 Imaging setup . . . 50
5.5 The imaging scheme . . . 50
5.6 Temperature measurements . . . 51

6.1 Detection path for photons . . . 54

6.2 Hanbury Brown Twiss type Interferometer to measure Intensity correlations . . . 55
6.3 Homodyne Tomography . . . 56
6.4 Measurement of electronic noise level . . . 57
6.5 Homodyne phase locking scheme . . . 58
6.6 Phase measurement in reflection . . . 60
6.7 Squeezing spectrum in transmission . . . 61
6.8 Phase measurements . . . 62
6.9 Phase dependent noise from laser . . . 62
6.10 Phase noise from the laser lock . . . 63
6.11 Intensity dependent phase noise from model . . . 63
6.12 Phase noise through cavity . . . 64
6.13 Dispersive non-linearities using Rydberg excitations . . . 68
6.14 Resonant excitation scheme with experiment . . . 69

7.1 Main cavity setup . . . 72
7.2 Technical drawing of the cavity holder . . . 73
7.3 Cavity locking loop using PDH technique . . . 74
7.4 Cavity lock stability . . . 75
7.5 Cavity with incident and reflected fields . . . 76
7.6 Experimental Setup . . . 76
7.7 Configuration for small cloud preparation . . . 78
7.8 Experimental Sequence . . . 79
7.9 Images of atomic clouds during different stages . . . 80
7.10 Cooperativity measurement . . . 81
7.11 Probe intensity as seen by atoms . . . 82
7.12 A bird's eye view of the blue cavity along with the viewports of the vacuum chamber . . . 83
7.13 Cross-section view of blue cavity along with optical beams 84
7.14 Blue inhomogeneous effects . . . 86
7.15 EIT measurements in linear regime . . . 87
7.16 Rydberg linewidth measurements . . . 88
7.17 Non-linearity using Rydberg S states . . . 89
7.18 Stark effect on Rydberg D states . . . 91
7.19 Transient measurements . . . 92
7.20 Probing long lived Rydberg D states . . . 93
7.21 Rydberg D-state nonlinearity . . . 94

8.1 Excitation scheme for photons . . . 98
8.2 $g^{(2)}(0)$ on resonant in reflection . . . 99
8.3 $g^{(2)}(0)$ in transmission . . . 99
8.4 Excitation scheme . . . 100
8.5 Intensity correlation measurement . . . 101
8.6 Phase dependent quadrature noise induced by Rydberg-Rydberg interactions . . . 102
8.7 EIT-induced quadrature noise at 700 kHz . . . 103
8.8 EIT-induced quadrature noise using a linear model . . . 103

9.1 Rydberg blockade volume . . . 111
9.2 Cavity comparison . . . 112
9.3 Cavity waist size dependence on length . . . 113
9.4 Configuration of the bottom mirror . . . 114
9.5 Waist size of the TEM00 mode as a function of frequency spacing between the higher order TEM modes . . . 115
9.6 Different cavity modes excited . . . 116
9.7 Cavity linewidth measurement . . . 116
9.8 Cavity drifts . . . 117
9.9 EIT measurement . . . 119
9.10 Proposed excitation scheme in dispersive regime . . . 120
9.11 Statistics of transmitted light . . . 121
9.12 Phase gate . . . 122
9.13 Photonic controlled phase gate . . . 123
9.14 Fidelity of the gate . . . 124

A.1 Hyperfine structure of D_2 transition . . . 132

C.1 Stark map of the 85D state . . . 136

D.1 The Wigner function of a coherent state . . . 137
D.2 Cross section of a Wigner function of pure Fock states . . . 138

List of Tables

4.1 **Summary of all required atomic transitions.** 34
4.2 **Summary of all lasers.** 35
4.3 **Transfer cavity** 38

5.1 **LVIS chamber parameters.** 48
5.2 **Main chamber parameters** 49

6.1 **Comparision of the $g^{(2)}$ measurement and the Homodyne detection** 56

7.1 **Main cavity parameters** 72
7.2 **Main cavity lock parameters** 75
7.3 **Final sequence timings** 80
7.4 **Blue cavity paramters** 82
7.5 **Blue locking specifications** 85

9.1 **Main cavity parameters** 117

A.1 **Selected fundamental constants.** 131
A.2 **Properties of ^{87}Rb atoms.** 132

B.1 **Properties of Rydberg atoms** 133

Preface and Overview

List of abbreviations used in this thesis

LVIS	Low Velocity Intense source
MOT	Magneto Optical Trap
EIT	Electromagnetically Induced Transparency
AOM	Acoustic Optic Modulator
EOM	Electro Optic Modulator
LO	Local Oscillator
SPCM	Single Photon Counting Module
PDH	Pound Drever Hall lock
PID	Proportional-Integral-Derivative controller
FALC	Fast Analog Linewidth Control
PZT	Piezo Transducer
UHV	Ultra High Vacuum ($< 10^{-8}$ Torr)
DDS	Direct Digital Synthesizers
Ti:Saph	Titanium-doped Sapphire (Ti:Al_2O_3)
IR	Infrared
RF	Radio frequency
PD	Photo diode
FFT	Fast Fourier Transform

Chapter 1

Introduction

According to Moore's law, the number of transistors per cm^2 would increase exponentially by doubling every 1 to 2 years [1]. Soon enough we will reach a fundamental boundary where the storage of information can no longer be explained by classical laws [2]. The strange effects in the physics of individual quantum objects will start to play role in how the electrons behaves. Hence, it's necessary to understand how we can take these effects into consideration and go beyond the classical systems. Quantum computation is a way of exploiting the special properties of the quantum world to speed up computational process. Richard Feynman speculated that quantum systems can be used to build advanced simulators [3]. This idea has attained a significant interest since Shor developed a quantum algorithm to factorize a large number (N) [4]. Shor's quantum factorization method can run in polynomial time in log(N) whereas the best classical method (general number field sieve) scales exponentially in log(N) [5]. The experimental realization of quantum simulators or computers has motivated many research groups. Numerous interesting algorithms have been proposed but their experimental implementation in large scales is still a long standing goal.

Quantum Computation

In computers, the information is stored in the form of zeros and ones known as bits. The smallest units of a quantum computing machine are known as quantum bits, also referred to as qubits [6]. Unlike classical bits, each qubit can exist in superposition states and qubits can be entangled with one another. This enables quantum computers to perform calculations in a vast Hilbert space at higher speed. These properties give quantum computers an unprecedented advantage over their classical counterpart.

A quantum computer cannot be built like a classical one as it requires a new technology which can enable us to store information in superposition states. There has been a considerable progress in the last decade to make quantum computation a reality. There are many quantum systems such as neutral or charged atoms, superconducting qubits, quantum dots etc., which have many characteristic traits to become a component of a quantum computer. Currently, it is possible to en-

gineer quantum states like Schrödinger cat states using optical systems [7, 8] and microwave photons [9, 10]. However, in most of these schemes realizing a system which has a strong isolation from environment and on demand 'on/off' control over interactions is a technical challenge. Some companies like 'D-wave Systems' claim they invented the first quantum computer, but they use "quantum annealing" for adjusting interactions to shape the final collective quantum state. Upto now this type of approach cannot be scaled up efficiently without overcoming environmental noise.

Modular quantum networks

Scaling up quantum systems without losing their coherence is an ambitious task. The conventional way of connecting every qubit to one another is likely to fail due to buildup of errors. Algorithms like quantum error correction require more qubits to correct for errors which in turn increases the complexity of the system. A promising solution is distributed quantum information processing or modular networks, where the quantum nodes are connected by networks of channels [11, 12]. Instead of entangling all the qubits with one another, few qubits form a node which makes it easier to manage them [13]. Our group's approach is to use cavity enhanced neutral atoms with photons as carriers. In Figure 1.1 cavity systems at nodes are connected to each other via channels like fiber optical links.

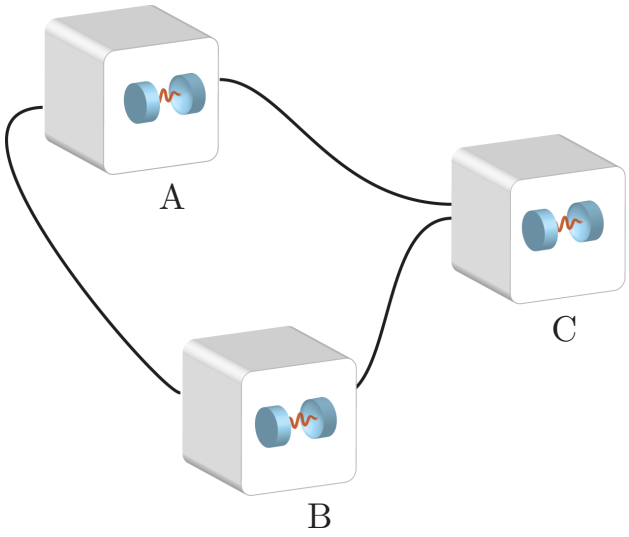

Figure 1.1: **Modular computing**: A quantum network of nodes A, B and C are connected by channels like fiber optic links. Each node consists of cavity systems. In distributed networks, nodes process information and perform quantum operations like quantum gates, etc.

Photons as flying qubits

For the past decade, optical fibers have dominated as information communication channels. Photons are robust against environmental noise which makes them ideal

candidates for information transfer [14]. They can be transported with ease over long distances and can be incorporated into existing communication channels. Photons are also relatively easy to produce using many systems like spontaneous parametric down-conversion or cold atomic memories. Several existing methods such as Hanbury Brown and Twiss effect or homodyne tomography help us to easily characterize the quality of these photons [15, 16].

In conventional optical fiber systems, it is common to use optical amplifiers to boost the signal to transport it over long distances. For quantum networks, a specific system, the quantum repeater, has been designed to counteract the decoherence effects introduced during transmission over long distances. One cannot simply detect or amplify the signal akin to classical communication. A quantum repeater system transports information without actually measuring it. The standard approach involves a source of entangled photons and a quantum repeater node where logical operations take place. In order to project the signal state onto one of the entangled photon, a projective measurement operation is carried out between the signal photon and the other entangled one. In addition, by using an entanglement purification process between different nodes, photonic states can be transferred over long distances with high fidelity [17, 18].

Quantum computation using photons

The main building blocks of quantum networks are non-classical states and coherent manipulation techniques. A gate operation is necessary for the realization of a full scale computational system [19]. One commonly used multi-bit gate is a controlled phase gate where one of the input bits acts as a control. The operations of a controlled phase gate are illustrated in Figure 1.2.

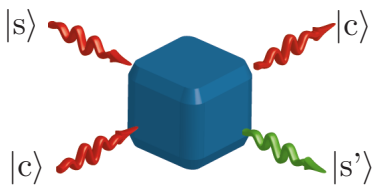

Input	Output
$\|c\rangle\|s\rangle$	$\|c\rangle\|s'\rangle$
$\|0\rangle\|0\rangle$	$\|0\rangle\|0\rangle$
$\|1\rangle\|0\rangle$	$\|1\rangle\|0\rangle$
$\|0\rangle\|1\rangle$	$\|0\rangle\|1\rangle$
$\|1\rangle\|1\rangle$	$-\|1\rangle\|1\rangle$

Figure 1.2: **Quantum Control Z gate**: Control phase or Z gate is a two qubit gate where one of the input qubits acts as a control ($|c\rangle$). The other input qubit is represented as $|s\rangle$. The output state of the gate is the same as the input state except when both the signal and the control qubit are in state '1', then it acquires a phase of π.

In 2001, Knill et. al. [20] proposed a scheme where single photons coupled with linear elements (like beam splitters, phase shifters) can be used for quantum information protocols. However its experimental implementation demands highly

efficient single photon sources and counters. In addition, they are inherently probabilistic [21]. Therefore, we resort to photon-photon nonlinearities for realization of quantum gates.

Since photons interact weakly with one another, it is a challenging task to observe non-linearities at few photon level. To achieve deterministic quantum interactions, we need strongly non-linear systems [22, 23]. For example, if we need an infrared photon wave packet (with a bandwidth of 1 MHz) to attain an optical phase shift of π by propagating in a medium of length equal to Rayleigh range of the photon then the medium's third order susceptibility($\chi^{(3)}$) has to be greater than $10^{-3}\mathrm{V}^{-2}\mathrm{m}^2$ [24]. But conventional optical medias exhibit extremely weak optical susceptibilities and the phase shift obtained is twenty orders of magnitude lower than the desired value [24]. Strong Kerr non-linear effects can be realized by using resonant optical medias like cold atoms or trapped ions [25].

Cold atoms

Quantum optical non-linearities using atomic ensemble as an intermediary medium has gained a significant interest since the proposal by Jaksch et.al. [26]. Cold atoms have well established trapping techniques along with tremendous control over its states which makes them promising candidates for quantum computers. Information can be stored in 'built-in' internal states of atoms which possess long coherence times. In addition, it is possible to use optical lattices to scale up neutral atomic systems [27]. Dipole-dipole interactions between atoms can influence the properties of neighboring atoms and can give rise to collective cooperative behavior like super-radiance [28]. These interactions can be only observable in a very dense atomic ensembles like BEC, etc. Our main objective is to enhance these interactions to achieve quantum optical non-linearity in atomic clouds. Until now, the two main promising approaches to strong photon-photon interactions are Electromagnetically Induced Transparency (EIT) and cavity Quantum Electro-Dynamics (cQED) [29].

To enhance the optical non-linearity one can couple a two-level system to a high finesse optical cavity. The study of this strong coupling between the atoms and cavity is referred to as cQED. Many interesting results have been obtained using cavity QED systems since the demonstration of quantum state manipulation using microwave cQED [9, 10].

Two level atomic media can exhibit strong non-linear response close to resonance, but the photons are lost by scattering. In 1990, Harris et al. proposed that by adding an additional coupling transition, the medium can be rendered transparent while enhancing the optical susceptibilities [30, 31]. In addition, the group velocity of the light is strongly reduced which allows us to store light as polaritons [32]. The reported susceptibilities are still not sufficient to achieve a phase shift of π at few photon level.

Our approach is to use long range dipole-dipole interactions between collective atomic excitations to achieve quantum optical non-linearities. In the next section, we present how one can tune the dipole-dipole interaction strength to achieve few photon non-linearities.

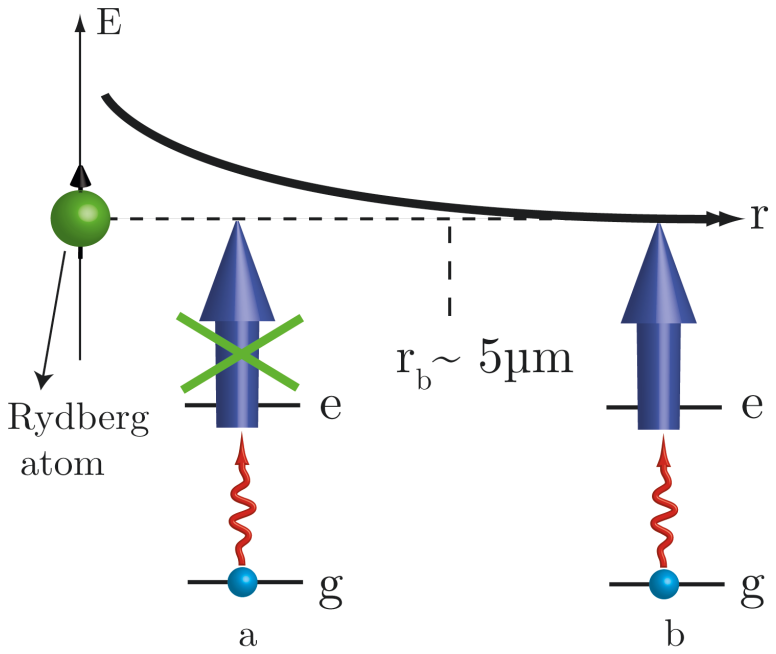

Figure 1.3: **Rydberg-Rydberg interaction energy shift vs Interatomic distance**: When an atom (b) is far from a Rydberg atom then it can be excited to a Rydberg level using resonant lasers. If an atom (a) moves closer then its energy levels are perturbed and it is no longer possible to excite it to Rydberg state. The minimum distance upto which a Rydberg atom can influence another is defined as Rydberg blockade radius (r_b). A typical blockade radius is of the order of $\sim 5\,\mu$m.

Strong photonic non-linearities via Rydberg EIT

The idea is to map the photons onto highly excited atomic states called Rydberg states and then use the long range dipole-dipole interactions between them to enable photon-photon interaction. The idea of using Rydberg atoms has generated substantial interest since the proposal of non-classical state generation using the 'dipole blockade' mechanism in mesoscopic ensembles [22]. However, exciting them directly to Rydberg states using only optical light is inefficient because of their weak transition dipole moments. In 2005, Friedler et. al. proposed exciting to Rydberg states using EIT, where a two photon excitation scheme is used to render the medium transparent [33]. Prior to this, most EIT experiments were carried out using a second ground state as metastable state. They showed that two photon pulses can be converted to dark state polaritons which interact via dipole-dipole interactions and acquire a phase shift of π to realize a photonic gate. Moreover, Rydberg atoms in optical lattices can be used as a simulator for many body interaction systems [34].

Since then, a number of interesting experiments have been carried out to convert photonic excitations to Rydberg polaritons starting with the group of Charles Adams at University of Durham [35] during 2010-13. They demonstrated optical non-linear effects in classical regime using free-space atomic systems. More recently, non-linearities at quantum level have been demonstrated by creating a single photon source [36], a photon blockade where only single photons are transmitted [37], photon bunching in dispersive regime [38]. A Rydberg based photon switch where a

single 'gate' photon forbids the transmission of a 'target' photon was observed [39]. A single-photon transistor where the gain is quantified by how many photons can be scattered by a single photon has been realized using Rydberg EIT [40, 41] and a gain greater than 100 has been achieved by using Förster resonance [42].

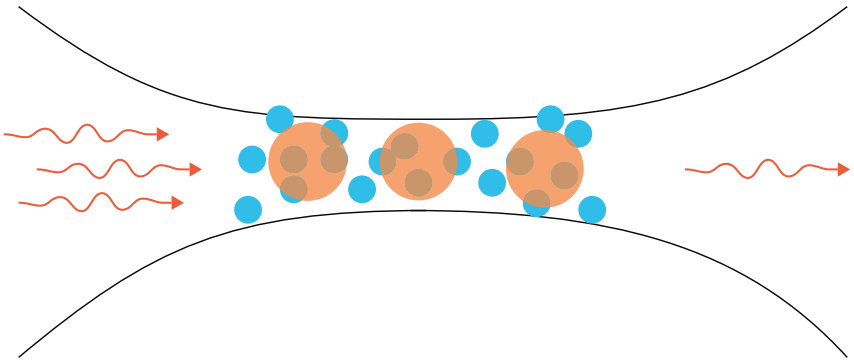

Figure 1.4: **A single photon filter using Rydberg excitations:** Probe field is coupled into a cigar shaped atomic cloud where the Rydberg blockade radius is comparable to the mode waist. When Rydberg polaritons are created in the cloud, the medium becomes opaque for any photons travelling in the medium.

Phase gates using a cavity

The observation of π phase shift per photon has motivated many experimental groups to explore various multilevel atomic systems. A weak phase shift of 18 μrad has been observed in free space using only EIT. It has been shown by Shapiro [43] and also by Gea-Banacloche [44], that locality and causality prohibits high-fidelity π-phase shifting operations between traveling photons. To circumvent the problem, one can store the photons in an atomic media to reduce the group velocity to zero [45].

By combining the advantages of cavity and Rydberg atoms one can create more exotic states without resorting to very high optical/atomic densities. Rydberg excitations in an optical resonator are potential candidates to reach quantum regime even with weak interactions between polaritons. In cavity Rydberg systems quantum effects were predicted [46, 47] though not yet observed, but strong classical non-linearities were demonstrated in the dispersive regime [48].

Thesis Layout

This thesis is a summary of the work carried out at the Institut d'Optique in an attempt to observe quantum optical non-linearities. We use a cold atomic cloud trapped in the mode of a low finesse optical cavity. This system has been chosen for its ability to combine the advantages of cavity and atomic cloud systems. This manuscript is organized in the following manner

- In part 1, we establish a standard notation for the computation of various relevant parameters of our system. We show why optical interactions induced by two level and three level non-interacting EIT systems is not sufficient to move to the quantum regine. We also introduce two models to explain Rydberg induced optical non-linearities in the classical regime.

- In part 2, we describe various parts of our experimental setup, and present the necessary lasers and hardware required to trap atoms. We conclude with various atomic cloud characterization methods.

- In part 3, we begin with various detection methods available on our setup and go on to present the Rydberg non-linearity measurements for S and D states. We also describe higher order correlation effects predicted for the measured non-linearity. We conclude the chapter with second order correlation measurements using a Hanbury Brown Twiss setup and squeezing spectrum measurements using a homodyne setup.

- In part 4, we present how a new high finesse cavity with a small mode-waist designed to move towards the quantum regime. We describe the new cavity design and its properties. We include details on how the new cavity is mounted and characterized on our setup. We present the recent EIT measurements along with some numerical calculations of squeezing spectrum expected with the new setup. We also present some theoretical ideas which could be implemented with the new setup, which would allow us to observe quantum optical non-linearities.

Part I

Theoretical tools

Chapter 2

Theoretical tools for Atom-Light coupling

Contents

2.1 Light propagation in a dielectric medium 11

2.2 Semi-classical approach of the light-atom system . . . 12

2.3 Quantum mechanical approach 15

2.3.1 Optical Bloch equations 16

2.3.2 Optical bistability using two level atoms 18

2.4 Three level atoms 20

2.4.1 Electromagnetically Induced Transparency 21

2.4.2 Linear response 22

2.4.3 Multilevel system 23

2.5 Non-linearity 24

In this chapter we will present the framework to describe our atom-cavity system. We will establish basic notions of light propagation through a cavity enhanced cold atomic media by deriving the expressions for susceptibility. We will show how to quantify the non-linearity arising from two-level and multi level atoms. Finally, we show why one needs to go beyond these systems to have quantum optical non-linearities.

2.1 Light propagation in a dielectric medium

Here we introduce expressions for a classical field propagating in a dielectric medium. The optical waves propagate through a dielectric medium by continuous absorption and re-emission of wave energy by atoms in the medium. This light-matter interaction can be quantified by defining a parameter called polarizability of the medium. It is related to the induced polarization $\vec{P}(\vec{r},t)$ by the propagating electromagnetic

wave $\vec{E}(\vec{r},t)$ [49]

$$\vec{P}(\vec{r},t) = \int_{-\infty}^{t} dt' \alpha_1(t-t')\vec{E}(\vec{r},t')dt' + \int_{-\infty}^{t}\int_{-\infty}^{t} dt'' \alpha_2(t-t',t-t'')\vec{E}(\vec{r},t')\vec{E}(\vec{r},t'') + ... \tag{2.1}$$

Where α_i is the polarizability of the medium of order i. This induced polarization in turn affects both the phase and the amplitude of the propagating electromagnetic waves. If we expand the incoming field in the frequency domain, then the polarization can be written as

$$P(\omega) = \varepsilon_0 \chi(\omega) E(\omega) \tag{2.2}$$

$$\chi(\omega) \quad = \chi_1(\omega) + \chi_2(\omega)E(\omega) + \chi_3(\omega = \omega_1 + \omega_2)E_1(\omega_1)E_2(\omega_2)... \tag{2.3}$$

The real part of the susceptibility contributes to the dispersion of light, and the imaginary part to the absorption of light. From the above expression we can evaluate the effect of matter on light using the the expression $n = \sqrt{1+\chi}$. Most materials and gases exhibit centro-symmetry and it can be shown that the second order term vanishes in these media. In linear systems, one can neglect all the higher order terms and the susceptibility term is independent of the field strength. In non-linear systems, the third order term is the lowest contributing one and the susceptibility depends on the incoming field's intensity. In the following sections we will describe how one can evaluate the susceptibility term in atomic systems.

2.2 Semi-classical approach of the light-atom system

A monochromatic wave incident on an atomic medium close to the resonance of two-levels can be described by a semi-classical approach, where the atoms are considered as two level quantum systems. We denote the two levels of the atom as g (ground state) and e (excited state). The energy difference between the levels is represented by $E_e - E_g = \hbar\omega_{ge}$. We introduce atomic operators that are denoted by $\hat{\sigma}_{kl}^{(n)} = |k\rangle\langle l|$ for atom n. The atomic Hamiltonian for atom 'n' can then be denoted by $\mathcal{H}_a^{(n)} = \hbar\omega_{ge}(\hat{\sigma}_{eg}^{(n)}\hat{\sigma}_{ge}^{(n)})$. The light-atom system can be described by evaluating

$$\mathcal{H}_s = \mathcal{H}_a + \mathcal{H}_i \tag{2.4}$$

As we treat light classically ($\vec{E}(\omega) = \mathcal{E}_0\vec{u}\,(e^{i\omega t} + e^{-i\omega t})$), we consider that the only role of light is to create an interaction potential. An atom driven close to the resonance of an optical transition can be considered as an oscillating dipole. The transition moment operator of the atom 'n' for $|g\rangle \rightarrow |e\rangle$ is given by

$$\hat{\vec{d}}^{(n)} = d_0\vec{u}(\hat{\sigma}_{ge}^{(n)} + \hat{\sigma}_{eg}^{(n)}) \tag{2.5}$$

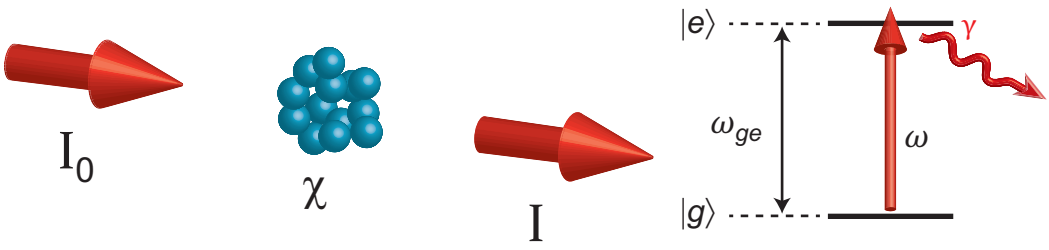

Figure 2.1: **Two-level excitation scheme**: Each atom is considered as a two-level system with ground state 'g' and excited state 'e'. An optical beam with intensity I_0 is incident on the atomic media with frequency ω, and we denote the susceptibility of the atoms as χ. The energy difference between the two levels is denoted by ω_{ge}.

By using the rotating wave approximation[1], one can neglect the rapidly oscillating terms and rewrite the interaction Hamiltonian as $\mathcal{H}_{int} = \sum_n -\hat{\vec{D}}^{(n)}.\vec{E}(r_a) = \sum_n d_0\mathcal{E}_0\left(e^{-i\omega t}\hat{\sigma}_{ge}^{(n)} + e^{i\omega t}\hat{\sigma}_{eg}^{(n)}\right)$. The total Hamiltonian of the system can be expressed as

$$\hat{\mathcal{H}}_s = \hbar\Delta_e\sum_n^N \hat{\sigma}_{ee}^{(n)} + \sum_n \hbar\Omega\left[e^{-i\omega t}\hat{\sigma}_{ge}^{(n)} + e^{i\omega t}\hat{\sigma}_{eg}^{(n)}\right] \tag{2.6}$$

where $\Omega = -(d_0\mathcal{E}_0)/\hbar$, N is total number of atoms and $\Delta_e = \omega - \omega_{ge}$. One can then use Heisenberg equations to evaluate the evolution of any operator $\hat{A}$ using [51].

$$\frac{d}{dt}\hat{A} = \frac{i}{\hbar}[\hat{\mathcal{H}}_s, \hat{A}] - \gamma_{\hat{A}}\hat{A} + F_a \tag{2.7}$$

where γ_e is the decay rate of the excited state and F_a is the Langevin noise operator associated with the operator $\hat{A}$. Using the steady state approximation, we obtain the following expression for the average value of the coherence term ($\hat{\sigma}_{ge}$)

$$\begin{aligned}\left\langle\hat{\sigma}_{ge}^{(n)}\right\rangle &= \frac{i\Omega(\left\langle\hat{\sigma}_{ee}^{(n)}\right\rangle - \left\langle\hat{\sigma}_{gg}^{(n)}\right\rangle)}{2(\gamma_e + i\Delta_e)} = -\frac{i\Omega}{2(\gamma_e + i\Delta_e)}\frac{1}{(1+\frac{\Omega^2}{2(\gamma_e^2+\Delta_e^2)})};\\ &= \frac{\Omega}{2}\frac{\Delta_e - i\gamma_e}{\gamma_e^2 + \Delta_e^2 + \Omega^2/2}\end{aligned} \tag{2.8}$$

where $\gamma_e = \frac{d_0^2k^3}{6\pi\varepsilon_0\hbar}$ is half of the natural linewidth of the excited state.

We can define an average coherence term using $\hat{\sigma}_{ge} = \frac{1}{N}\sum_n \hat{\sigma}_{ge}^{(n)}$. If the medium has a uniform density ρ then one can estimate the induced polarization density

$$P(\omega) = \rho\langle\hat{D}\rangle = \rho d_0\left\langle\hat{\sigma}_{ge}e^{-i\omega t} + \hat{\sigma}_{eg}e^{i\omega t}\right\rangle = \frac{1}{2}\varepsilon_o\mathcal{E}_0\left(\chi(\omega)e^{-i\omega t} + \chi^*(\omega)e^{i\omega t}\right) \tag{2.9}$$

which gives the following expression for the atomic susceptibility

$$\chi(\omega) = \frac{\rho d_0^2}{\hbar\varepsilon_0}\frac{\langle\hat{\sigma}_{ge}\rangle}{\Omega/2} = -\frac{\alpha_0\gamma_e}{k}\frac{\langle\hat{\sigma}_{ge}\rangle}{\Omega/2} \tag{2.10}$$

[1]Complete derivation can be found in many standard textbooks, for example [50]

In the above equation we used the standard expressions for resonant optical cross-section for a two-level atom $\sigma_{\text{eff}} = \frac{3\lambda^2}{2\pi}$ and $\alpha_0 = \rho\sigma_{\text{eff}}$ [52]. The optical susceptibility is proportional to the term $\langle\hat{\sigma}_{ge}\rangle/\Omega \propto (\Delta_e - i\gamma_e)/2(\gamma_e^2 + \Delta_e^2)$ in the weak feeding approximation ($\gamma_e^2 + \Delta_e^2 \gg \Omega^2$). It is worth noting that the susceptibility doesn't depend on input intensity, hence the response of the system is linear in this regime.

Classical field in an optical cavity

We consider a linear cavity of length 'L' with an enclosed atomic medium. We represent the reflectivities of its mirrors by $R_1 = 1 - T_1 \approx 1$ and $R_2 = 1 - T_2$ and its resonant frequency by ω_c. The normalized transmission of the cavity is given by $\frac{T_1 T_2}{|(1-\sqrt{R_1 R_2}e^{i\Delta_c/\omega_f})|^2}$ where $\omega_f = \frac{c}{L}$ and the cavity detuning $\Delta_c = \omega - \omega_c$.

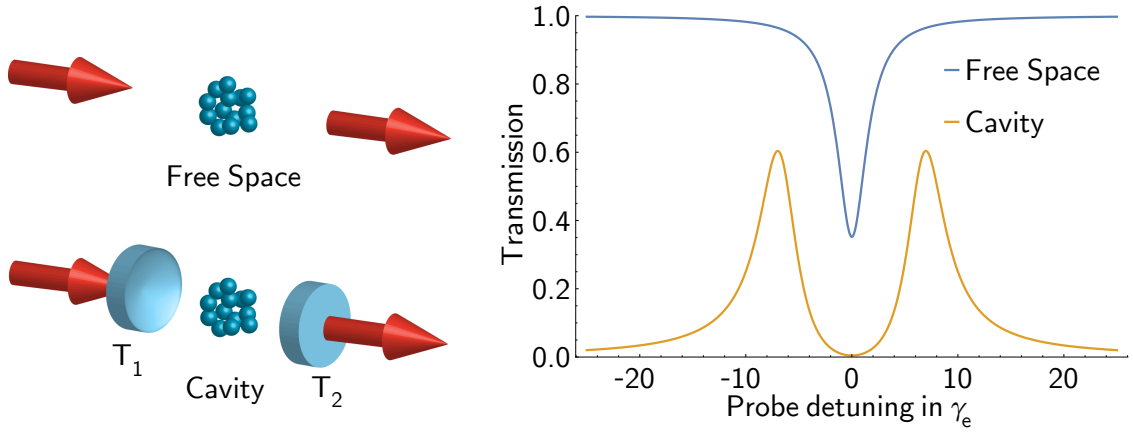

Figure 2.2: **Comparison of free space and cavity transmission**. **On the left**: We observe the transmission of a probe beam close to atomic resonance. We assume the cavity to be resonant with the atoms and the transmission coefficients of input and output mirrors are T_1 and T_2 respectively. **On the right**: The normalized transmission as a function of probe detuning when scanned around the atomic resonance. The blue line denotes the transmission of atoms in free space, whereas the red line represents the transmission through a cavity finesse of 100 and a cooperativity of 8.

If we have a medium of length l inside the cavity with refractive index $n = \sqrt{1+\chi} \approx 1+\chi/2$, then the light acquires a complex phase $e^{i\frac{\pi}{\lambda}\chi l}$ per single pass. The transmission through the cavity in this case can be written as $\frac{T_1 T_2}{|(1-\sqrt{R_1 R_2}e^{i\Delta_c/\omega_f}e^{i\frac{2\pi}{\lambda}\chi l})|^2}$ which can be approximated to

$$\begin{aligned} T = \frac{I_t}{I_i} &\approx \frac{T_1 T_2}{(1-\sqrt{R_1 R_2} + \frac{2\pi}{\lambda}\Im(\chi)l)^2 + R_1 R_2 \sin^2(\Delta_c/\omega_f + 2\pi\Re(\chi)/\lambda l)} \\ &\approx \frac{4T_1/T_2}{(1+\frac{4\pi}{T_2\lambda}\Im(\chi)l)^2 + (\Delta_c/\gamma_c + 4\pi\Re(\chi)/T_2\lambda l)^2} \end{aligned} \tag{2.11}$$

where $\gamma_c = T_2\omega_f/2$ by using $R_1, R_2 \approx 1$ and $|\chi| \ll \lambda/2\pi l$. In the case of atoms trapped in the cavity mode, by using the Eq. 2.10 the cavity transmission can be

rewritten as

$$\begin{aligned} T &= \frac{T_0}{\left(1-\frac{4\alpha_0 l\gamma_e}{T_2\Omega}\Im(\langle\hat{\sigma}_{ge}\rangle)\right)^2+\left(\frac{\Delta_c}{\gamma_c}-\frac{4\alpha_0 l\gamma_e}{T_2\Omega}\Re(\langle\hat{\sigma}_{ge}\rangle)\right)^2} \\ &= \frac{T_0}{\left(1-\frac{2C}{\Omega/2\gamma_e}\Im(\langle\hat{\sigma}_{ge}\rangle)\right)^2+\left(\frac{\Delta_c}{\gamma_c}-\frac{2C}{\Omega/2\gamma_e}\Re(\langle\hat{\sigma}_{ge}\rangle)\right)^2} \\ &= \frac{T_0}{\left(1-\frac{2C}{1+\Delta_e^2/\gamma_e^2+\Omega^2/2\gamma_e^2}\right)^2+\left(\frac{\Delta_c}{\gamma_c}-\frac{2C\Delta_e/\gamma_e}{1+\Delta_e^2/\gamma_e^2+\Omega^2/2\gamma_e^2}\right)^2} \end{aligned} \tag{2.12}$$

where $T_0 = 4T_1/T_2$ and $C = \frac{\alpha_0 l}{T_2}$ is the ratio of the absorption of the media (also known as optical depth) to the transmission of the lossy mirror. The term C is commonly referred to as the cooperativity of the medium and corresponds to a collective phenomena exhibited by the atoms.

As shown in Figure 2.2, the cavity transmission contains two normal modes when the detuning of the probe light is scanned around the atomic resonance. The position of the modes corresponds to those detunings for which the second term in the denominator goes to zero. In the weak feeding approximation, for large cooperativities the modes are separated by $\sqrt{8C\gamma_c\gamma_e}$ when the cavity is resonant with the atoms.

2.3 Quantum mechanical approach

In order to more accurately describe the system evolution we use a fully quantum mechanical approach to describe the light-atom coupling. We quantize the electromagnetic field in the cavity mode in the Schrödinger picture. By using the second quantization, we can describe the Hamiltonian of the single mode light field by

$$\mathcal{H}_l = \hbar\omega_c\left(\hat{a}^\dagger\hat{a}+\frac{1}{2}\right) \tag{2.13}$$

where ω_c is the cavity resonance frequency. We restrict ourselves to excitations only in the fundamental mode of the cavity. We can then write the quantized electromagnetic field operator in a cavity by using the boundary conditions for a cavity placed along the z axis [53]

$$\begin{aligned} \hat{E}(x,y,z) &= \vec{\mathcal{E}}(x,y,z)\left[\hat{a}e^{ikz}+\hat{a}^\dagger e^{-ikz}\right] \\ &= \vec{\mathcal{E}}(x,y,z)\left(\cos(kz)\left[\hat{a}+\hat{a}^\dagger\right]+i\sin(kz)\left[\hat{a}-\hat{a}^\dagger\right]\right) \end{aligned} \tag{2.14}$$

where $k = \omega_c/c$. We also assume that all the atoms are restricted within the Rayleigh range of the cavity mode, and hence the waist is assumed to be constant $\omega(z) \approx \omega_0$. The electric field term can be written as $\vec{\mathcal{E}}(x,y,z) = \mathcal{E}_0\vec{u}e^{-\frac{x^2+y^2}{2w_0^2}}$, where $\mathcal{E}_0 = \sqrt{\frac{\hbar\omega_c}{2V\varepsilon_0}}$ is the electric field per photon and the mode volume is $V = \int\cos^2(kz)e^{-\frac{x^2+y^2}{2w_0^2}}d^3r$.

Our system is composed of N atoms interacting with a single cavity mode. One can describe such a system using the Dicke model [28], where the atomic dipoles are coherently interacting with the electromagnetic field. The cavity is pumped with a coherent feeding rate α. Here we work in the open cavity limit ($\lambda \ll L$), where the spontaneous emission rate (γ_e) for an atom is close to its value in free space. The total Hamiltonian is given by

$$\begin{aligned}\hat{\mathcal{H}}_s &= \hat{\mathcal{H}}_l + \hat{\mathcal{H}}_a + \hat{\mathcal{H}}_{int} + \hat{\mathcal{H}}_f \\ &= \hbar\Delta_c \hat{a}^\dagger \hat{a} + \sum_n \hbar\Delta_e \hat{\sigma}_{ee}^{(n)} - \sum_n \hbar g(r_n)\left[\hat{a}\hat{\sigma}_{ge}^{(n)} + \hat{a}^\dagger \hat{\sigma}_{eg}^{(n)}\right] + \hbar\alpha(\hat{a} + \hat{a}^\dagger)\end{aligned} \tag{2.15}$$

In the above expression, the position dependent atom-light coupling term is given by $g(r_n) = g_0\mathcal{S}(r_n)$ where $g_0 = d_0\sqrt{\frac{\omega_c}{2\hbar\varepsilon_0 V}}$ is the vacuum Rabi frequency term and the function $\mathcal{S}(r_n) = \cos(kz)e^{-\frac{x^2+y^2}{2w_0^2}}$ depends on position of each atom r_n.

2.3.1 Optical Bloch equations

The dynamics of the system can be described by using the density matrix formalism (Schrödinger picture) or by Heisenberg-Langevin equations (Heisenberg picture). As our system exhibits dissipation, it is easier to describe using master equation in the Lindblad form. We must take into account both the dissipation of the cavity ($\hat{a}$) and atoms $\hat{\sigma}_{ge}$ to establish the evolution of the system. The evolution of the density matrix(ρ_s) can be expressed using Liouvillian terms ($\mathcal{L}(\hat{A})_{\rho_s}$) in the following form

$$\begin{aligned}\dot{\hat{\rho}}_s = &-\frac{i}{\hbar}\left[\hat{\mathcal{H}}_s, \hat{\rho}_s\right] - \gamma_c(\hat{a}^\dagger\hat{a}\hat{\rho}_s + \hat{\rho}_s\hat{a}^\dagger\hat{a} - 2\hat{a}\hat{\rho}_s\hat{a}^\dagger) \\ &- \gamma_e(\hat{\sigma}_{ge}\hat{\sigma}_{eg}\hat{\rho}_s + \hat{\rho}_s\hat{\sigma}_{ge}\hat{\sigma}_{eg} - 2\hat{\sigma}_{eg}\hat{\rho}_s\hat{\sigma}_{ge})\end{aligned} \tag{2.16}$$

From the above master equation we can extract the expectation values of the operators using the expression $\langle\hat{A}\rangle = \mathrm{Tr}(\hat{A}\hat{\rho}_s)$. The evolution of operators can be evaluated from $\frac{d}{dt}\langle\hat{A}\rangle = \mathrm{Tr}(\dot{\hat{\rho}}\hat{A})$ which gives the Heisenberg equations for the operators $\frac{d}{dt}\langle\hat{A}\rangle = \frac{i}{\hbar}\langle[\hat{\mathcal{H}}_s, \hat{A}]\rangle - \gamma_{\langle\hat{A}\rangle}\hat{A}$ [51]. The evolution of the intracavity field and the coherence terms can be calculated using

$$\frac{d}{dt}\langle\hat{a}\rangle = (i\Delta_c - \gamma_c)\langle\hat{a}\rangle + \sum_n g(r_n)\langle\hat{\sigma}_{ge}^{(n)}\rangle - i\alpha \tag{2.17}$$

$$\frac{d}{dt}\langle\hat{\sigma}_{ge}^{(n)}\rangle = (i\Delta_e - \gamma_e)\langle\hat{\sigma}_{ge}^{(n)}\rangle + ig(r_n)\langle\hat{a}(\hat{\sigma}_{ee}^{(n)} - \hat{\sigma}_{gg}^{(n)})\rangle \tag{2.18}$$

where the term α denotes the feeding rate into the cavity. In the steady state condition, we observe that

$$\frac{\langle\hat{\sigma}_{ge}^{(n)}\rangle}{\langle\hat{a}\rangle} = \frac{ig(r_n)}{(\Delta_e + i\gamma_e)}f(\langle\hat{a}\rangle^2) \tag{2.19}$$

$$\langle\hat{a}\rangle = \frac{\alpha}{\left(\Delta_c + i\gamma_c - i\sum_n g(r_n)\frac{\langle\hat{\sigma}_{ge}^{(n)}\rangle}{\langle\hat{a}\rangle}\right)} = \frac{\alpha}{\left(\Delta_c + i\gamma_c + \sum_n \frac{g^2(r_n)}{\gamma_c\gamma_e}\chi_n\right)} \tag{2.20}$$

where $\chi_n = \frac{\gamma_e}{g(r_n)}\frac{\langle\hat{\sigma}_{ge}^{(n)}\rangle}{\langle\hat{a}\rangle}$ is the susceptibility of each atom n. In a linear regime the function f($\langle\hat{a}\rangle^2$) is a constant and can be shown to be equivalent to the semi-classical description for coherent fields.

Cavity transmission

The normalized transmission of the cavity is proportional to the intracavity intensity. In steady state, for a weak feeding rate the normalized cavity transmission can be evaluated from

$$T = \frac{\langle \hat{a} \rangle^2 \gamma_c^2}{\alpha^2} = \frac{T_0}{\left(1 + \Im(\sum_n \frac{g^2(r_n)}{\gamma_c \gamma_e} \chi_n)\right)^2 + \left(\frac{\Delta_c}{\gamma_c} + \Re(\sum_n \frac{g^2(r_n)}{\gamma_c \gamma_E} \chi_n)\right)^2} \tag{2.21}$$

$$\approx \frac{T_0}{\left(1 - \frac{2C}{1+\Delta_e^2/\gamma_e^2}\right)^2 + \left(\frac{\Delta_c}{\gamma_c} - \frac{2C\Delta_e/\gamma_e}{1+\Delta_e^2/\gamma_e^2}\right)^2} \tag{2.22}$$

where T_0 is a proportionality constant and $C = \sum_n \frac{g^2(r_n)}{2\gamma_c \gamma_e}$. It must be noted here that the cooperativity parameter is equivalent to the one we derived in section : 2.2. It is an important figure of merit across various systems to quantify the coherent atom-light coupling. It is the ratio of the square of the coherent coupling to the product of the dissipation rates (cavity and atoms). The effective volume over an atomic medium of length l can be evaluated by

$$V = \frac{\int d^3\vec{r} \langle \hat{\vec{E}}_+(\vec{r})^2 \rangle}{\langle \hat{\vec{E}}_{max}(\vec{r})^2 \rangle} = \int\int\int dx dy dz \, \cos^2(kz) e^{-2\frac{x^2+y^2}{\omega_0^2}} = \frac{\pi}{4} L \omega_0^2$$

where the $\hat{\vec{E}}_+$ is one of the propagating field components. If we assume the medium has a uniform density ρ then we can write $\sum_n g^2(r_n) = g_0^2 \rho \pi l \omega_0^2/4$. Using the expressions for g_0, γ_c, γ_e, we can write cooperativity as $C = \frac{N'}{T_1} \frac{3\lambda^2}{2\pi\omega_0^2}$ where $N' = \rho\pi l\omega_0^2/4$ is the effective number of atoms coupled to the cavity.

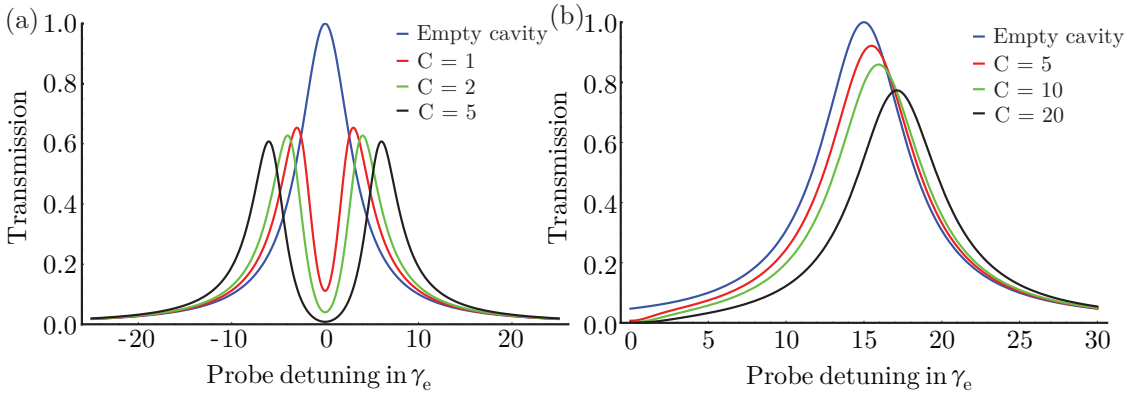

Figure 2.3: **Cooperativity measurement in absorptive and dispersive regime**: The normalized cavity transmission versus probe detuning normalized to γ_e for a cavity with a decay rate $\gamma_c = 3.3\gamma_e$ (a) When the cavity is on resonance with atoms the cavity transmission is split into two normal modes where the splitting is given by $\sqrt{8C\gamma_c\gamma_e}$. (b) When the cavity is detuned from the resonance of the atoms by $\Delta_e = 15\gamma_e$. The cavity transmission curve is shifted with a shift proportional to the cooperativity.

To increase the cooperativity one needs to have a very high atomic density or a very high finesse cavity. In this thesis, we are going to concentrate on scenarios where the atom-light coupling $g_0 \ll \gamma_c, \gamma_e$ and $\sqrt{N} g_0 > \gamma_c, \gamma_e$.

2.3.2 Optical bistability using two level atoms

Optical non-linearity has acquired tremendous interest since the prediction of optical bistability in resonator systems with non-linear media in the 1970s and has been well studied by many groups [54–56]. Optical bistability or multistability is the presence of more than one possible value for transmission for a given input intensity. This phenomenon can be observed only when the imaginary part or the real part of the susceptibility is a function of the intensity. This phenomena can be used to create an optical switch where one can alternate between two stable points deterministically [51, 57].

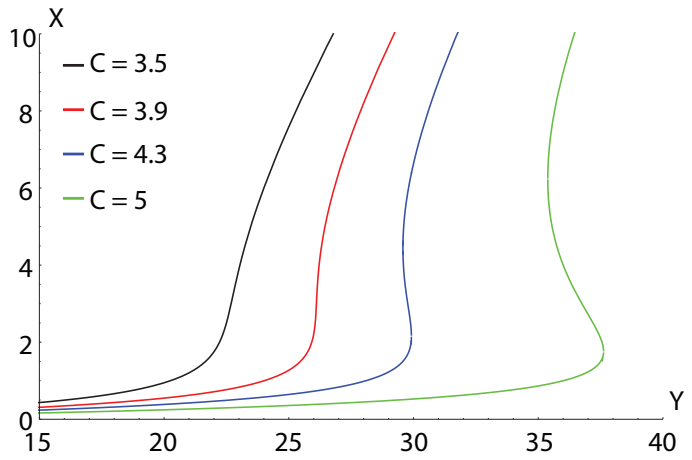

Figure 2.4: **Absorptive non-linearity**: The transmitted light (X) is plotted as a function of incident light (Y). We can see that for cooperativities higher than 4 there is a range of input intensities where the output light is multivalued.

Until now we have dealt with the situation where the susceptibility doesn't depend on the intensity of the incident light. It is a valid approximation for weak intensities, where the excited level population is not saturated. As soon as we reach a regime where $\Omega^2 \sim \gamma_e^2 + \Delta_e^2$ then the susceptibility depends on the intracavity field and vice versa.

We will show how the bistable behavior is originated in absorptive and dispersive regimes. The incident and transmitted light are normalized using saturation intensity (I_{sat}) and expressed as $X = \frac{I_t}{T_2 I_{sat}} = \frac{\Omega^2}{2\gamma_e^2}$ and $Y = \frac{I_i}{I_{sat}}$ [57, 58]. We can rewrite the stationary transmission functions of the cavity as

$$X = Y \left[\left(1 - 2C \frac{\Im\langle \hat{\sigma}_{ge} \rangle}{\Omega/2\gamma_e} \right)^2 + \left(\frac{\Delta_c}{\gamma_c} - 2C \frac{\Re\langle \hat{\sigma}_{ge} \rangle}{\Omega/2\gamma_e} \right)^2 \right]^{-1} \tag{2.23}$$

where the term $\frac{\langle \hat{\sigma}_{ge} \rangle}{\Omega/2\gamma_e}$ is a function of X. If both the cavity and the atoms are on resonance then we are in purely absorptive regime and we can evaluate the probe

transmission from

$$Y = X\left[\left(1+\frac{2C}{1+X}\right)^2\right] \tag{2.24}$$

The system can exhibit bistability when the cooperativity $C > 4$ as shown in Figure 2.4.

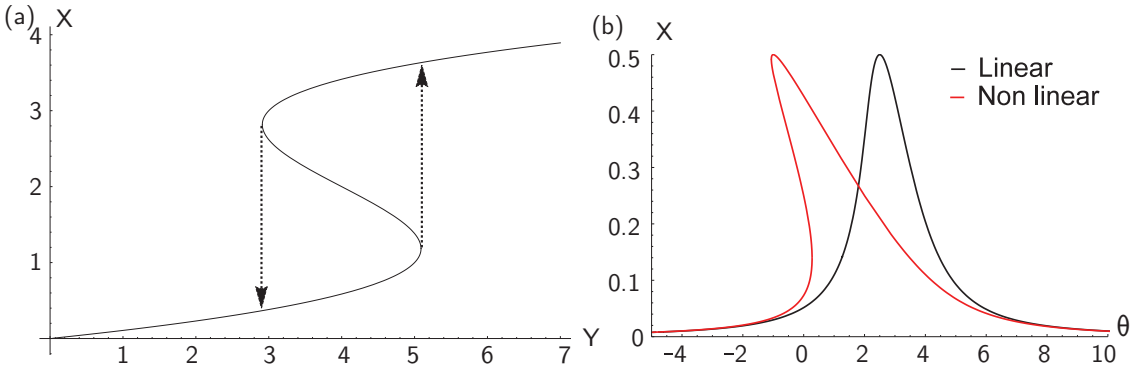

Figure 2.5: **Dispersive non-linearity**: (a) The transmitted light vs incident intensity when $A = 1$ and $B = 3$ (b) Transmitted light vs the detuning of the probe from the cavity in a linear case when $X = 0.1$ and non-linear when $X = 4$.

On the contrary, if the detunings are much larger than the incident probe intensity ($\Delta \gg \Omega$), then we are in the dispersive regime.

In the latter case the transmission function can be simplified to the following expression when $\Delta_e \gg 1$ and $\Delta_e \gg \frac{\Delta_c}{\gamma_c}$

$$X = \frac{Y}{1+(\theta - 2C\Re f(X))^2} \tag{2.25}$$

$$\approx \frac{Y}{1+(\theta - \frac{2C}{\Delta_e} + \frac{2C}{\Delta_e^3}X)^2} \tag{2.26}$$

where we replaced $\frac{\Delta_c}{\gamma_c}$ by θ. The above expression is in the form of $Y = X(1 + (B - AX)^2)$ where $A = \frac{2C}{\Delta_e^3}$ and $B = \frac{2C}{\Delta_e} - \theta$. It has more than one solution when $3A^2X^2 + -4ABX + B^2 + 1 = 0$. It exhibits bistability when the term B is greater than $\sqrt{3}$. In Figure 2.5(a) we see how the transmitted light varies with the incident probe intensity when $B = 3$ and $A = 1$.

In both cases of absorptive or dispersive bistability one needs to have X $>$ 1 which corresponds to an intracavity intensity comparable to I_{sat}. To achieve strong non-linearity for few photons, one needs to have a small mode volume and large cavity bandwidth. This can be achievable in the cavity-QED, regime but for our cavity atomic system where the mode-waist is of the order of 10 - 100 microns and cavity decay rate of tens of MHz, one needs few thousands of photons to reach non-linear regimes.

2.4 Three level atoms

In order to further enhance the optical non-linearities one must move to multi-level systems where phenomena like Electromagnetically Induced Transparency allows us to move closer to resonance, without losing photons by scattering [30, 59]. In addition to the attenuated absorption window, the steep dispersion curve increases the effective interaction time between the probe pulses and atoms [60, 61]. In the past two decades many groups have attempted, both theoretically and experimentally to lower the threshold to reach quantum regime [62–64].

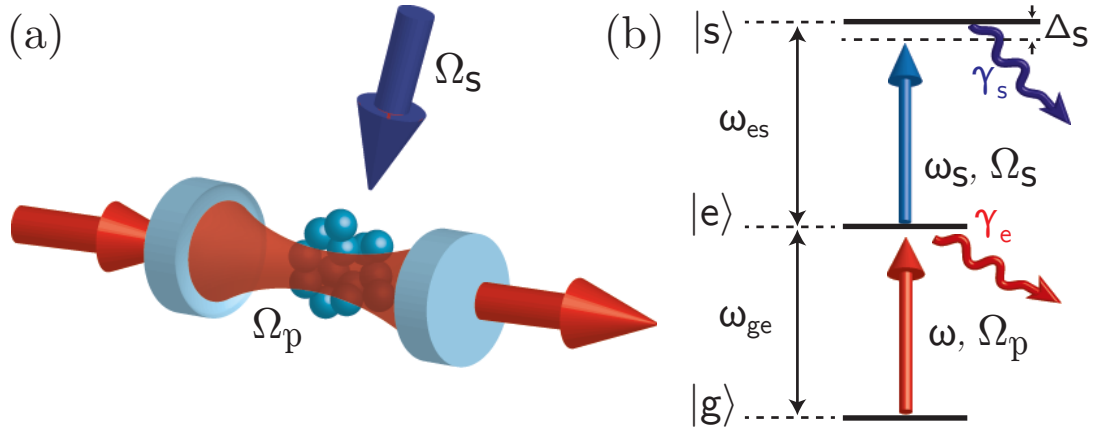

Figure 2.6: **Illustration of the excitation scheme for three level atoms in a cavity**: (a) The atoms are enclosed in a cavity with the probe coupled to the fundamental mode of the cavity and the control field incident from the side. (b) The three level excitation scheme is presented here along with the probe and the control fields.

In this section we will describe the optical response of three level atoms in a cavity. Consider an atom with a ground state (g), intermediate state (e), and a metastable state (s) separated by ω_{ge} and ω_{es} respectively. The two atomic transitions $|g\rangle \rightarrow |e\rangle$ and $|e\rangle \rightarrow |s\rangle$ are driven by a probe beam at ω and a control coherent beam at ω_s respectively. The detunings of probe and control beam are denoted by $\Delta_e = \omega - \omega_{ge}$, $\Delta_s = \omega_s + \omega - \omega_{gs}$. The additional Hamiltonian term for three level atoms is

$$\hat{\mathcal{H}}_s = -\Delta_s \sum_n \hat{\sigma}_{ss}^{(n)} + \frac{\Omega_s}{2} \sum_n (\hat{\sigma}_{se}^{(n)} + \hat{\sigma}_{es}^{(n)}) \tag{2.27}$$

Here we introduce a complex detuning term $D_i = \Delta_i + i\gamma_i$. The optical Bloch equations for the system at steady state when the cavity is coupled with coherent

feeding rate of α are

$$\begin{aligned}\langle\hat{a}\rangle &= \frac{1}{D_c}(g\sum_n\langle\hat{\sigma}_{ge}^{(n)}\rangle + \alpha)\\ \langle\hat{\sigma}_{ge}^{(n)}\rangle &= \frac{1}{D_e}\left(\frac{\Omega_s}{2}\langle\hat{\sigma}_{gs}^{(n)}\rangle - g\langle\hat{a}(\hat{\sigma}_{ee}^{(n)} - \hat{\sigma}_{gg}^{(n)})\rangle\right)\\ \langle\hat{\sigma}_{gs}^{(n)}\rangle &= \frac{1}{D_s}\left(\frac{\Omega_s}{2}\langle\hat{\sigma}_{ge}^{(n)}\rangle\right)\end{aligned} \tag{2.28}$$

From these equations we obtain the optical response of the system. In the next subsection we show some interesting effects which arise with three level system.

2.4.1 Electromagnetically Induced Transparency

In order to have a strong two level non-linear susceptibility one needs to move closer to resonance but the medium becomes opaque due to strong scattering by atoms. One way to circumvent this problem is by using Electromagnetically Induced Transparency, otherwise known as EIT. As the name indicates, the medium attains a narrow transparency band in the absorption spectrum and the dispersion spectra exhibits a steep slope when excited in certain conditions. Since the first observation of EIT [65], many groups have performed interesting experiments such as slow light [61], lasing without inversion [66], etc.

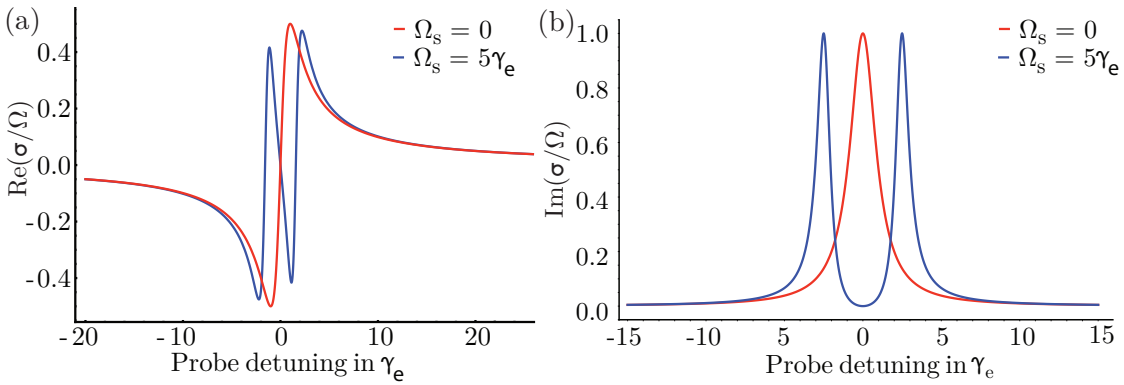

Figure 2.7: **Comparision of susceptibility of two level (red) and three level systems (blue)**: We assume that the linewidth $\gamma_s = 0.1\gamma_e$ (a) The real part of the susceptibility shows the dispersion spectra. It shows a sharp response for the medium at zero detuning. (b) The absorption peak at resonance splits into two peaks creating a transparency window.

To understand how the transparency works, lets consider a system of three level atoms which are weakly driven ($\Omega_p \ll \Omega_s, \gamma_e$) and all the transitions are resonant ($\Delta_i = 0$ for i $= e, s, c$) then the eigenstates of the system are $(|s\rangle \pm |e\rangle)/\sqrt{2}$ and $|g\rangle$. The probe couples to the $\pm|e\rangle$ components of the two eigenstates, which have equal magnitude and opposite sign. Hence it leads to destructive interference of both excitation pathways and therefore diminished absorption [30, 59].

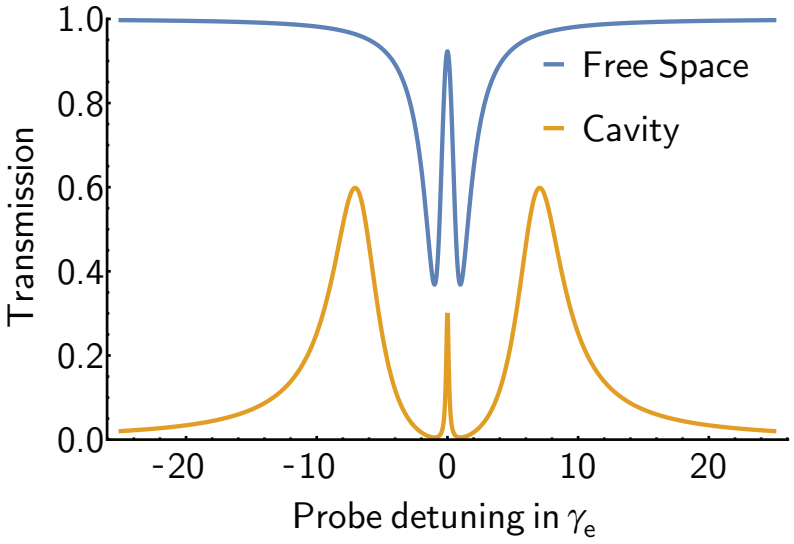

Figure 2.8: **Electromagnetically induced transparency curves in the presence and the absence of the cavity**. The transmission of the system is plotted with respect to probe detuning normalized to γ_e. We have assumed a low finesse (100) one-sided cavity. The frequency of the probe beam is sweeped around the resonance and the control beam is incident on resonance with the secondary transition ($\Delta_s = 0$). The value of control field Rabi frequency is assumed to be $2\gamma_e$ and the linewidth it taken to be $\gamma_s = 0.06\gamma_e$.

2.4.2 Linear response

The response of three level atoms can be simplified using the Bloch equation under weak feeding approximation and assuming all the atoms have equal coupling. If we neglect the atomic excitation ($\langle \hat{\sigma}_{ee}^{(n)} - \hat{\sigma}_{gg}^{(n)} \rangle \ll 1$) then the coherence term for any atom n is

$$\begin{aligned} \langle \hat{\sigma}_{ge}^{(n)} \rangle &\approx \frac{1}{D_e} \left(\frac{\Omega_s}{2} \langle \hat{\sigma}_{gs}^{(n)} \rangle + g \langle \hat{a} \rangle \right) \\ &= \frac{g\alpha}{\tilde{D}_e D_c - \sum_n g^2} = \frac{g\alpha}{\tilde{D}_e D_c - 2\gamma_e \gamma_c C} \end{aligned} \tag{2.29}$$

The above expression is the same as two level susceptibility except that the term D_e is replaced by $\tilde{D}_e = \Delta_e - \frac{\Omega_s^2}{4D_s}$.

One can obtain an analytical expression to the transmission in steady state:

$$T = \left| \frac{\gamma_c \tilde{D}_e}{\tilde{D}_e D_c - 2\gamma_c \gamma_e C} \right|^2 \tag{2.30}$$

In Figure 2.8 we compare the EIT in cavity systems with free space. We can observe that the EIT transmission peak is lower in cavity systems due to multiple reflections inside the cavity.

On resonance excitation

If the detuning of the control beam is zero ($\Delta_s = 0$) and the probe is on resonance with atoms ($\Delta_e = \delta = 0$) then the imaginary part of the susceptibility goes to zero. The probe is transmitted by the system as if the medium is transparent. In the absence of control field, even for moderate cooperativities (C ≈ 5) the transmission drops below 1%. When the control field is $\Omega_s \approx 2\gamma_e$ and the linewidth of the state $|s\rangle$ $\gamma_s \sim 0.06\gamma_e$ then the on-transmission is close to 30%.

In Figure 2.7, the dispersion curve in EIT exhibits a steep slope which leads to the phenomena of slow light [61] and the imaginary part of the susceptibility drops to zero on resonance.

Off-resonance excitation

If we excite the atoms off-resonantly on the probe transition, then interesting features are observed near the two photon resonance [67,68]. The resonant absorption line remains almost unaffected while a second absorption/dispersion response is observed at $\Delta_e \approx -\Delta_c$. This corresponds to a two-photon resonance, where the atomic population is transfered from ground state to the meta stable one.

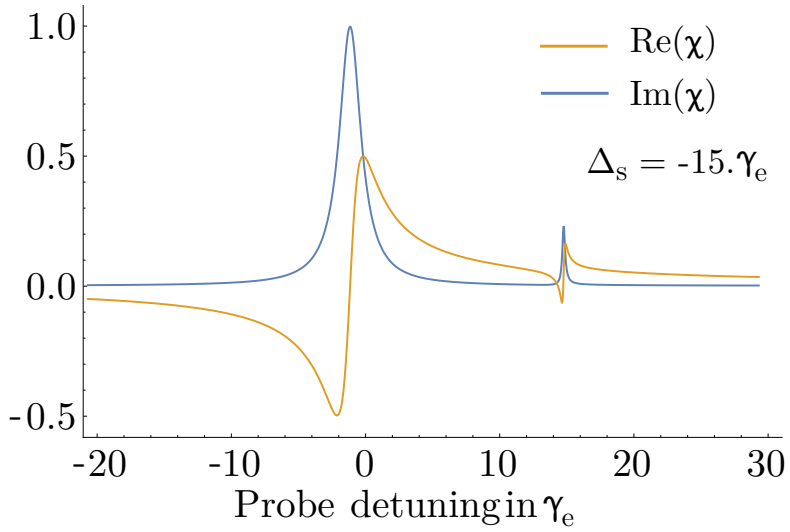

Figure 2.9: **Two-photon resonance response**: The real and the imaginary part of the susceptibilities of a system when the control field is detuned by -15γ_e, its Rabi frequency is set to 5γ_e and the linewidth is taken as 0.1γ_e. This creates a sharp medium response at two photon resonance.

2.4.3 Multilevel system

In degenerate energy systems like Rydberg D states where multiple magnetic sublevels are degenerate any weak electric fields can lead presence of more than three levels in the system refer Sec:7.5.2. Here we calculate how the transmission of the system is modified in the presence of more than one metastable state. We assume

that we are in a linear excitation regime (where $\langle\sigma_{gg}^{(i)}\rangle \gg \langle\sigma_{ee}^{(i)}\rangle$). The extra Hamiltonian terms are

$$\hat{\mathcal{H}}_{ext} = \frac{\Omega_{s'}}{2}\sum_n(\hat{\sigma}_{s'e}^{(n)} + \hat{\sigma}_{es'}^{(n)}) + \frac{\Omega_{s''}}{2}\sum_n(\hat{\sigma}_{s''e}^{(n)} + \hat{\sigma}_{es''}^{(n)})... \tag{2.31}$$

We can define a new intermediate detuning term which can be written as $\tilde{D}_e = D_e - \frac{\Omega_s^2}{4\delta} - \frac{\Omega_{s'}^2}{4\delta} - \frac{\Omega_{s''}^2}{4\delta}$. By evaluating the above expression we can evaluate the EIT spectrum for multilevel atoms.

2.5 Non-linearity

The presence of a third level modifies the optical response in a non-trivial way. The two photon resonance in off-resonant excitation scheme exhibits a narrow response. This allows us to easily saturate the medium which gives rise to a non-linear optical response. Large non-linearities have been observed experimentally based on these schemes [63, 68, 69].

If we look at the expression for susceptibility, we can observe that the intracavity intensity is rescaled by the factor $1+\frac{\Omega_s^2}{8\delta^2}$. One can observe large non-linearities with even weaker probe fields by having a strong control field Rabi frequency. However, the effects cannot be described as "true" non-linearities because they are manifested from saturation of $|s\rangle$. The photons are just converted into atomic excitations in the other ground state. Even though compared to two level systems the number of photons required to observe the non-linearity has decreased, the number of atomic excitations are still of the same order. So, in order to observe strong non-linear effects we need an extra feature which doesn't convert the photons into atomic excitations. As we will see in the next chapter, atoms excited to $|s\rangle$ must exhibit long range interactions, which will render the remaining atoms further detuned from the optical fields.

Chapter 3

Rydberg-Rydberg Interactions

Contents

3.1 Introduction 25
3.2 Mean field approach 27
3.3 Rydberg bubble model 28

3.1 Introduction

As we have shown in the previous chapter that non-linearities obtained using multi-level or EIT schemes are not strong enough to be observed at single photon level. To achieve this we need some kind of interaction between the atoms which can modify the behavior of the cloud even with few polaritons in the system. The promising solution is to use highly excited Rydberg atoms. The remarkably properties exhibited by atoms excited to Rydberg states will help us in realizing strong interatomic interactions [70].

Atoms excited to a very high principal quantum number, higher than 30 are referred as Rydberg atoms. They have long lifetimes (few 100 μs) and large dipole moments, which makes them sensitive to weak perturbations in their environments [71]. This large dipole moment creates a dipole potential through which it can interact with neighbouring atoms over long distances (few microns). Rydberg-Rydberg interactions have several degrees of freedom, one can control the type of interactions, the distance and the direction by selecting a Rydberg state. By mapping photons onto Rydberg excitations one can achieve exotic states of photons or strong non-linear interactions.

The dipole-dipole interaction energy between neutral dipoles separated by a distance 'R' is given by

$$V_{d_1,d_2}(R) = \frac{1}{4\pi\varepsilon_0}\left[\frac{d_1.d_2}{|R|^3} - 3\frac{(d_1.R).(d_2.R)}{|R|^5}\right] \tag{3.1}$$

In order to evaluate the interacting two-atom system, one needs to take into account mainly the neighboring Rydberg energy levels which contribute the signifi-

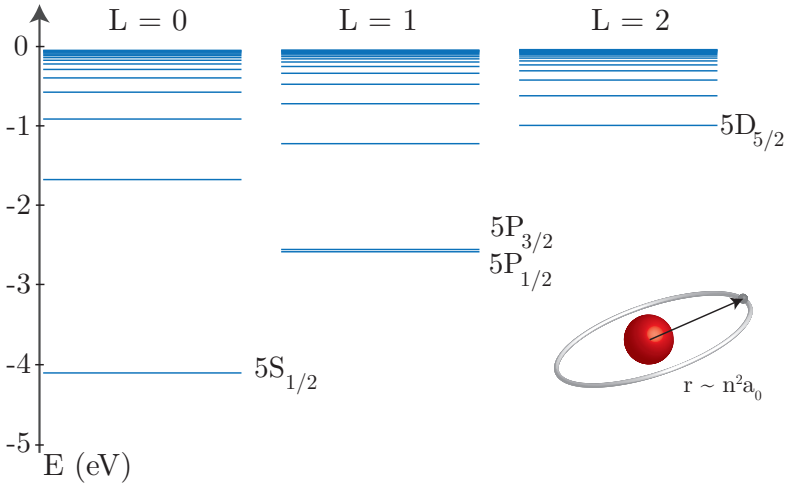

Figure 3.1: **Quantized energy levels of Hydrogen-like atoms**: The electronic energy levels for low angular momentum states are plotted. The valence electrons for low angular momentum states spend more time closer to the nucleus, hence need more energy to ionize. **In the inset**: The Rydberg atomic radius increases with the square of principal quantum number (n^2). The valence electron can move up to few microns away from the nucleus for n = 140.

cantly to the interaction. If we consider two atoms with atomic states $|r_1\rangle$, $|r_2\rangle$ and $|r_3\rangle$. We assume that the pair states $|r_2 r_2\rangle$ and $|r_1 r_3\rangle$ are separated by Δ and the state $|r_2 r_2\rangle$ is coupled to $|r_1 r_3\rangle$ by $V(R)$. The eigenenergies of pair system can be written as

$$E_{\pm} = \frac{\Delta \pm \sqrt{\Delta^2 + 4V(R)^2}}{2}$$

The eigenenergies of the total Hamiltonian can be described in two different regimes: the Van der Waals regime, and the dipole-dipole regime. One in which the interaction term is much smaller than the energy difference ($V(R) \ll \Delta$) it is referred to as off-resonant Van der Waals interactions, and at the other extreme where the interaction term is much larger than the detuning ($V(R) \gg \Delta$) are called as resonant dipole-dipole interactions.

In the Van der Waals regime the eigenenergies are shifted by ($\Delta E \propto C_6/R^6$) and in the resonant dipole-dipole regime they are shifted by ($\Delta E \propto C_3/R^3$). This dipole interaction strength C_3 and C_6 scales as $(n^*)^4$ and $(n^*)^{11}$ respectively.

These interactions lead to a Rydberg level detuned out of resonance and the control field is no longer resonant with the secondary transition, this effect is known as Rydberg blockade effect. The medium then acts as two-level atoms and the absorption dominates. They are currently one of the most actively researched candidates in quantum optics for generating non-classical states or quantum effects using dipole-dipole interactions [72].

The Rydberg-Rydberg interaction Hamiltonian term between atoms in Rydberg state $|r\rangle$ is [47]

$$\mathcal{H}_{int} = \frac{1}{2} \sum_{m \neq n} \kappa_{m,n} \hat{\sigma}_{rr}^{(m)} \hat{\sigma}_{rr}^{(n)} \tag{3.2}$$

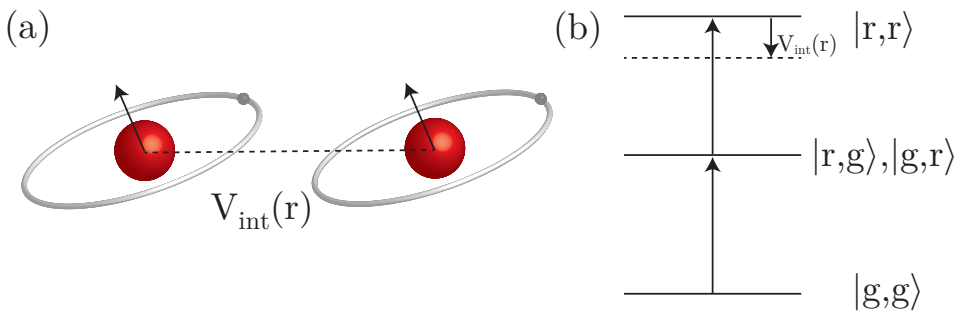

Figure 3.2: **Rydberg-Rydberg Interactions**: (a) Two interacting Rydberg atoms separated by a distance r. (b) The energy levels of the combined two atom system. If the excitation linewidth is lower than the $V_{int}(r)$ then it is not possible to reach the $|r,r\rangle$ state.

The Bloch equations for the coherence terms can be derived from the total Hamiltonian along with the interaction term, leading to the following equations.

$$\begin{aligned}
\frac{d}{dt}\hat{\sigma}_{ge}^{(n)} &= i(\Delta_e + i\gamma_e)\hat{\sigma}_{ge}^{(n)} + ig\hat{a}(\hat{\sigma}_{ee}^{(n)} - \hat{\sigma}_{gg}^{(n)}) - i\frac{\Omega_{cf}}{2}\hat{\sigma}_{er}^{(n)} + \hat{F}_{ge}^{(n)} \\
\frac{d}{dt}\hat{\sigma}_{er}^{(n)} &= i(\delta + i\gamma_{er})\hat{\sigma}_{er}^{(n)} + iga^{\dagger}\hat{\sigma}_{gr}^{(n)} + i\frac{\Omega_{cf}}{2}(\hat{\sigma}_{rr}^{(n)} - \hat{\sigma}_{ee}^{(n)}) - i\hat{\sigma}_{er}^{(n)}\sum_{m\neq n}\kappa_{m,n}\hat{\sigma}_{rr}^{(m)} + \hat{F}_{er}^{(n)} \\
\frac{d}{dt}\hat{\sigma}_{gr}^{(n)} &= i(\Delta_r + i\gamma_r)\hat{\sigma}_{gr}^{(n)} + ig\hat{a}\hat{\sigma}_{er}^{(n)} - i\frac{\Omega_{cf}}{2}\hat{\sigma}_{ge}^{(n)} - i\hat{\sigma}_{gr}^{(n)}\sum_{m\neq n}\kappa_{m,n}\hat{\sigma}_{rr}^{(m)} + \hat{F}_{gr}^{(n)}
\end{aligned} \tag{3.3}$$

where $F_{ij}^{(n)}$ is the Langevin noise operator corresponding to the operator $\hat{\sigma}_{ij}^{(n)}$, $\delta = \Delta_e + \Delta_s$ is two photon detuning term and Ω_{cf} is the control field Rabi frequency ($|e\rangle \rightarrow |r\rangle$). The interaction term is restricted to the symmetric subspace, where states are invariant under the permutation of two particles and $\kappa_{m,n}$ is interaction energy between atoms m and n in Rydberg state. This interaction term is a function of C_6 in the case of Van der Waals interaction and C_3 for resonant dipole-dipole interaction.

The interaction term in the Hamiltonian is an N body problem and it cannot be solved without making some approximations like the mean field approach. Here we will describe two such methods which we use to explain our Rydberg non-linearity measurements. The models have been developed by Andrey Grankin and Etienne Brion, they are well described in A. Grankin's thesis [73].

3.2 Mean field approach

The computation of the non-linear response of N body interactions scales exponentially and becomes intractable for even few atoms. One way to circumvent this problem is by using a mean field approach [74, 75] where each atom's response is modified by a mean field it experiences from its neighboring atoms.

We introduce two new collective atomic operators corresponding to the transi-

tions $|g\rangle \rightarrow |e\rangle$ and $|g\rangle \rightarrow |r\rangle$

$$\begin{aligned}\hat{b} &= \tfrac{1}{\sqrt{N}} \textstyle\sum_i \hat{\sigma}_{ge}^{(i)} \\ \hat{c} &= \tfrac{1}{\sqrt{N}} \textstyle\sum_i \hat{\sigma}_{gr}^{(i)}\end{aligned}$$

which are governed by the following dynamical equations:

$$\begin{aligned}\frac{d}{dt}\langle\hat{a}\rangle &= (i\Delta_c - \gamma_c)\langle\hat{a}\rangle - ig\sqrt{N}\langle\hat{b}\rangle - i\alpha \\ \frac{d}{dt}\langle\hat{b}\rangle &= (i\Delta_e - \gamma_e)\langle\hat{b}\rangle - i\sqrt{N}g\langle\hat{a}\rangle - i\tfrac{\Omega_{cf}}{2}\langle\hat{c}\rangle \\ \frac{d}{dt}\langle\hat{c}\rangle &= (i\Delta_r - \gamma_r)\langle\hat{c}\rangle - i\tfrac{\Omega_{cf}}{2}\langle\hat{b}\rangle - i\kappa\langle\hat{c}^\dagger\hat{c}\hat{c}\rangle\end{aligned}$$

The complex constant κ characterizes the effect of dipole-dipole Rydberg interactions, and was found to be

$$\kappa = -2\left(\frac{V_b}{V - V_b}\right)\left(\frac{\Omega_{cf}^2}{4(D_e + D_r - \frac{\Omega_{cf}^2}{4(D_e)})} - (D_r)\right) \tag{3.4}$$

$$V_b = \frac{\sqrt{2}\pi^2}{3}\sqrt{\frac{C_6}{D_e - \frac{\Omega_{cf}^2}{4(D_e + D_r - \frac{\Omega_{cf}^2}{4D_e})}}} \tag{3.5}$$

where $D_k \equiv \Delta_k + i\gamma_{gk}$ for $k = e, r$, V_b is the blockaded volume of a single blockade, and V is the total volume of the cloud.

In steady state conditions when all the transitions are resonant, the ratio $\frac{V_b}{V} \ll 1$. Hence, we can use the mean field approximation where the state of the system is approximated to be coherent. We can replace the operators with complex numbers which leads to a simplified interaction term $V_{int} = |\langle\hat{c}\rangle|^2\kappa\langle\hat{c}\rangle$. This simplifies the response of the system in steady state to

$$\begin{aligned}\langle\hat{a}\rangle &= -\tfrac{\langle\hat{b}\rangle g\sqrt{N}}{\Delta_c + i\gamma_c} - \tfrac{\alpha}{\Delta_c + i\gamma_c} \\ \langle\hat{b}\rangle &= -\tfrac{\langle\hat{a}\rangle g\sqrt{N}}{\Delta_e + i\gamma_e} - \tfrac{\langle\hat{c}\rangle i\Omega_{cf}}{2(\Delta_e + i\gamma_e)} + \tfrac{g\sqrt{N}\langle\hat{a}\rangle}{\Delta_e + i\gamma_e} \\ \langle\hat{c}\rangle &= -\tfrac{\langle\hat{b}\rangle i\Omega_{cf}}{2(\Delta_r + i\gamma_r)} - \tfrac{|\langle\hat{c}\rangle|^2\kappa\langle\hat{c}\rangle^*}{\Delta_r + i\gamma_r}\end{aligned}$$

The average interaction term κ can be calculated in the large volume approximation ($V \gg V_b$). The cavity transmission is then evaluated from the cavity field $\langle\hat{a}\rangle$ with the expression:

$$T = \frac{\gamma_c^2 . |\langle\hat{a}\rangle|^2}{\alpha^2}$$

3.3 Rydberg bubble model

For Rydberg interactions in D-states, one needs to take into account an additional dephasing mechanism due to the presence of degenerate magnetic sublevels [76].

This mechanism creates stray Rydberg excitations which are no longer coupled to control field. These long lived excitations inhibit creation of any new Rydberg excitations upto a certain distance (blockade radius r_b) around them. This blockaded sphere is commonly referred to as Rydberg bubble, or Rydberg superatom, and is frequently used to explain the Rydberg blockade effect [77]. This bubble picture puts an upper limit on the number of Rydberg excitations ($\mathcal{N}_b$) one can have in a finite volume cloud which allows us to calculate the number of atoms per bubble from

$$n_b = \frac{N}{\mathcal{N}_b} = \frac{2\pi^2 \rho_{at}}{3} \sqrt{\frac{|C_6|}{\Delta_r - \Omega_{cf}^2/4\Delta_e}} \tag{3.6}$$

Here, we give details about the phenomenological model we used to account for the dynamical behavior of the cavity transmission, in the case of samples excited to Rydberg D states.

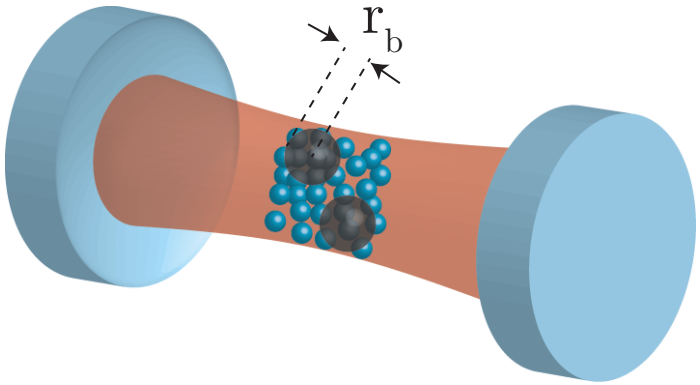

Figure 3.3: **Rydberg bubble**: The atomic cloud is divided into spheres where each of them can at most have a single Rydberg excitation.

We assume that the Rydberg blockade phenomenon effectively splits the atomic sample into independent and equivalent "bubbles" which can at most accommodate for one Rydberg excitation. Accordingly, the two-photon transition towards the Rydberg level $|r\rangle$ essentially couples the two collective symmetric states

$$\begin{aligned} |G\rangle &\equiv |g\cdots g\rangle \\ |R\rangle &\equiv \frac{1}{\sqrt{n_b}} \sum_{n=1}^{n_b} \hat{\sigma}_{rg}^{(n)} |G\rangle = \frac{1}{\sqrt{n_b}} \left(|rg\cdots g\rangle + \cdots |g\cdots gr\rangle\right) \end{aligned}$$

where n_b denotes the number of atoms in a Rydberg bubble, and the corresponding lowering operator is the Pauli-like matrix $\hat{\sigma}_{GR} \equiv |G\rangle\langle R|$ (we also define $\hat{\sigma}_{RR} \equiv |R\rangle\langle R|$ and $\hat{\sigma}_{RG} \equiv |R\rangle\langle G|$). Note that n_b can be evaluated by $n_b = N \times \left|\frac{V_b}{V}\right|$, where N is the total number of atoms in the sample, V is the total volume of the sample and V_b is the volume of a Rydberg bubble whose expression is given in Eq. 3.4.

In a Rydberg bubble, the intermediate state can, by contrast, be arbitrarily populated; we will further assume that we remain in the low excitation regime (corresponding to moderate cavity feeding rates) so that the transition to the intermediate state is never saturated. In this approximation scheme, the collective lowering operator

$$\hat{\beta} \equiv \frac{1}{\sqrt{n_b}} \sum_{n=1}^{n_b} \hat{\sigma}_{ge}^{(n)} \tag{3.7}$$

can be considered bosonic, i.e. $\left[\hat{\beta}, \hat{\beta}^\dagger\right] \approx 1$.

In order to account for the dynamical behavior observed experimentally, we introduce an extra Rydberg state, denoted by $|s\rangle$, to which the state $|r\rangle$ decays: this implies that, in a bubble, the collective states $|R\rangle$ and $|S\rangle \equiv \frac{1}{\sqrt{n_b}} \left(|sg\cdots g\rangle + \cdots |g\cdots gs\rangle\right)$ are coupled by a Lindblad-like operator.

To simplify the treatment, we furthermore assume the cavity mode to be classical, that is we replace a by its expectation value $\langle a \rangle$ whose time evolution is ruled by the equation

$$\frac{d}{dt}\langle a \rangle = \mathrm{i}\left(\Delta_c + \mathrm{i}\gamma_c\right)\langle a \rangle - \mathrm{i}\left(\frac{N}{n_b}\right) g\sqrt{n_b}\left\langle \hat{\beta} \right\rangle - \mathrm{i}\alpha$$

Note that the second term of this equation arises from the coupling of the cavity mode with the ensemble of $\left(\frac{N}{n_b}\right)$ Rydberg bubbles with the magnified coupling strength $g\sqrt{n_b}$. The first term accounts for the detuning and decay of the cavity, while the last one results from the feeding by the probe field. In this semi-classical approximation, bubbles do not entangle with the cavity mode and therefore cannot get entangled with each other. The atomic sample can hence be described by the tensor product density matrix $\rho \otimes \cdots \otimes \rho$, where ρ is the density matrix of any of the bubbles (they are all equivalent). The dynamic semi-classical equation for ρ now writes $\frac{d}{dt}\rho = -\mathrm{i}\left[H, \rho\right] + \mathcal{D}_l\left(\rho\right) + \mathcal{D}_{nl}\left(\rho\right)$ where

$$\begin{aligned}
H &= -\Delta_r \left|R\right\rangle\left\langle R\right| - \Delta_e \hat{\beta}^\dagger\hat{\beta} \\
&\quad + \left\{\left(\frac{\Omega_{cf}}{2}\hat{\sigma}_{RG} + g\sqrt{n_b}\left\langle a\right\rangle^*\right)\hat{\beta} + \mathrm{h.c.}\right\} \\
\mathcal{D}_l\left(\rho\right) &= \gamma_e\left(2\hat{\beta}\rho\hat{\beta}^\dagger - \hat{\beta}^\dagger\hat{\beta}\rho - \rho\hat{\beta}^\dagger\hat{\beta}\right) \\
&\quad + \gamma_r\left(2\hat{\sigma}_{GR}\rho\hat{\sigma}_{RG} - \hat{\sigma}_{RR}\rho - \rho\hat{\sigma}_{RR}\right) \\
&\quad + \gamma_s\left(2\hat{\sigma}_{GS}\rho\hat{\sigma}_{SG} - \hat{\sigma}_{SS}\rho - \rho\hat{\sigma}_{SS}\right) \\
\mathcal{D}_{nl}\left(\rho\right) &= \xi\left\langle\hat{\sigma}_{RR}\right\rangle\left(2\hat{\sigma}_{SR}\rho\hat{\sigma}_{RS} - \hat{\sigma}_{RR}\rho - \rho\hat{\sigma}_{RR}\right)
\end{aligned}$$

Note that the phenomenological extra nonlinear decay $\mathcal{D}_{nl}\left(\rho\right)$ we introduced is time dependent through $\left\langle\hat{\sigma}_{RR}\right\rangle\left(t\right)$; its rate is moreover governed by the ad hoc free parameter ξ, whose value can be tuned so as to reproduce the experimental results. This model will be used in Sec: 7.5.3.

Part II

Experimental apparatus

Chapter 4

Optical and control system

Contents

4.1 Trapping and excitation lasers 33

4.2 Frequency stabilization system 35

4.2.1 Transfer cavity 36

4.2.2 Characterization tests 38

4.2.3 Stability of lasers 39

4.3 Control/Acquisition setup 41

4.3.1 Hardware components 41

4.3.2 Software 41

In this chapter, we will present various elements which constitute our experimental setup. The primary requirement of a cold atomic experiment is a Magneto-Optical trap (MOT), where the atoms are trapped using optical beams in magnetic field. The setup has been comprehensively described by Erwan Bimbard's thesis [78]. Here we will recall the setup along with some additional characterization tests. We will describe the experiment in three parts - in the first part we describe the laser table, where we prepare the optical beams; in the second part we describe the acquisition/control setup, and in the final part we describe the main table, where we trap and manipulate the atoms.

4.1 Trapping and excitation lasers

Introduction

We use a dedicated optical table to prepare the laser beams necessary for our experiment. These beams are later coupled into various fibers and then sent to the main table where we trap our atoms. In this section we describe how we lock and prepare the optical beams for our experiment. We use a mixture of diode and Titanium-Sapphire lasers. The diode lasers are very compact and can be modified

to have extremely narrow linewidths, while the Ti-Sa lasers have a large tuning range with high output power.

Master laser

The main reference laser on our system is a Toptica DL Pro diode laser which is used to trap, cool and probe the D2 transition of Rb^{87} at 780 nm. The diode is mounted on an aluminum plate with a collimator lens and an output coupler. An anti-reflection coating at the back of the diode makes the system act like a resonator. A grating is mounted on a piezo inside the resonator to tune the resonance. The frequency of the laser diode can also be adjusted by changing the driving current. The temperature and the current of the diode is controlled by using the commercial control modules Toptica DTC110 and Toptica DCC110, respectively. The temperature of the diode is maintained at $20°C$. The power of the diode is later amplified using a tapered amplifier and at the output we can achieve up to 1W. We split the output power into various arms for trapping and probing.

The master laser is frequency stabilized using a stabilization system which will be discussed further in section 4.2. We use dedicated double pass Acoustic Optic Modulators (AOMs), which enables us to shift the frequency of the laser without losing coupling to fibers.

Repumper and dipole trap lasers

Due to the hyperfine splitting of $5S_{1/2}$ in Rb^{87}, the atoms are lost to a dark state when trapped using an open transition. To recapture the lost atoms, we employ a DL pro Toptica laser (referred to as repumper) with an output of 30 mW. It is frequency stabilized on a crossover transition $5S_{1/2}\,F = 1 \rightarrow 5P_{3/2}\,F' = 1 - 2$ by using standard absorption saturation spectroscopy. The laser is then frequency shifted to be on resonance with atoms using an AOM.

Recently, we installed a new diode laser at 810 nm to optically trap the atoms and to lock the newly installed optical cavity around the atoms.

Laser	Transition
Trapping	$5S_{1/2}\,F = 2 \rightarrow 5P_{3/2}\,F' = 3$
Repumper	$5S_{1/2}\,F = 1 \rightarrow 5P_{3/2}\,F' = 2$
Depumper	$5S_{1/2}\,F = 2 \rightarrow 5P_{1/2}\,F' = 2$
Optical pumping	$5S_{1/2}\,F = 2 \rightarrow 5P_{1/2}\,F' = 2$
Probe	$5S_{1/2}\,F = 2 \rightarrow 5P_{3/2}\,F' = 3$

Table 4.1: **Summary of all required atomic transitions**.

Titanium-Sapphire traps

We have two Coherent MBR-110 Titanium doped Sapphire lasers which can be tuned between wavelengths of 750 to 900 nm using an etalon in a built-in cavity. The lasers are pumped by two Verdi V10 lasers at 532 nm with a maximum possible

power of 16 W. The power at the output of these systems can reach upto 2 W. We use one of them at 810 nm for creating a dipole trap, as well as for other purposes where we need a beam far from all optical transitions. The second one at 795 nm is used to address D1 transition. Unlike the diode lasers, Ti-Sa lasers are stabilized to an internal reference cavity. The cavity length can be adjusted to fine tune the frequency. Our laser stabilization system has a Free Spectral Range (FSR) of 110 MHz which lets us to stabilize our lasers to any frequency we want with the help of double pass AOMs with a range of 50 MHz.

Blue laser

In order to excite the atoms to Rydberg state the transition frequencies are in ultraviolet regime. It is possible to coherently excite using a single photon transition [79], however it is technically challenging to work with lasers at ∼297 nm. Hence we use a two photon transition, where the secondary atomic transition $5P_{3/2} \rightarrow nS$ or nD is used to excite to Rydberg S or D states. For this purpose, we need a tunable laser at 480 nm which is generated using a Toptica SHG pro laser of ≈ 400 mW output. It consists of a diode at 960 nm which is amplified to 1 W. It is later up-converted to 480 nm using a resonant doubling cavity. We extract a part of 960 nm to stabilize the frequency.

Laser	Power
Master laser	1 W 780 nm
Repumper	30 mW at 780 nm
Blue laser	400 mW at 480 nm
TiSa 1	2 W at 810 nm
TiSa 2	2 W at 795 nm

Table 4.2: **Summary of all lasers**.

4.2 Frequency stabilization system

It is not always possible to find a suitable atomic transition to lock a laser for e.g. dipole trap lasers. The most convenient way is to lock all the lasers on an optical cavity known as transfer cavity. This type of locking technique provides a convenient way to lock all the lasers and at the same time gives enough flexibility to tune the frequency to whatever value we need. One can either employ a very high finesse ($> 10^4$) passive optical cavity [80] or an actively stabilized cavity locked onto an atomic reference [81]. We use a transfer cavity stabilized to a crossover transition $5S_{1/2}\, F = 2 \rightarrow 5P_{3/2}\, F' = 2 - 3$ in Rb^{87}. We extract a part of the master laser and modulate it using an Electro-Optic Modulator (EOM) at $\simeq 21$ MHz, which provides the sidebands necessary for the Pound Drever Hall error signals.

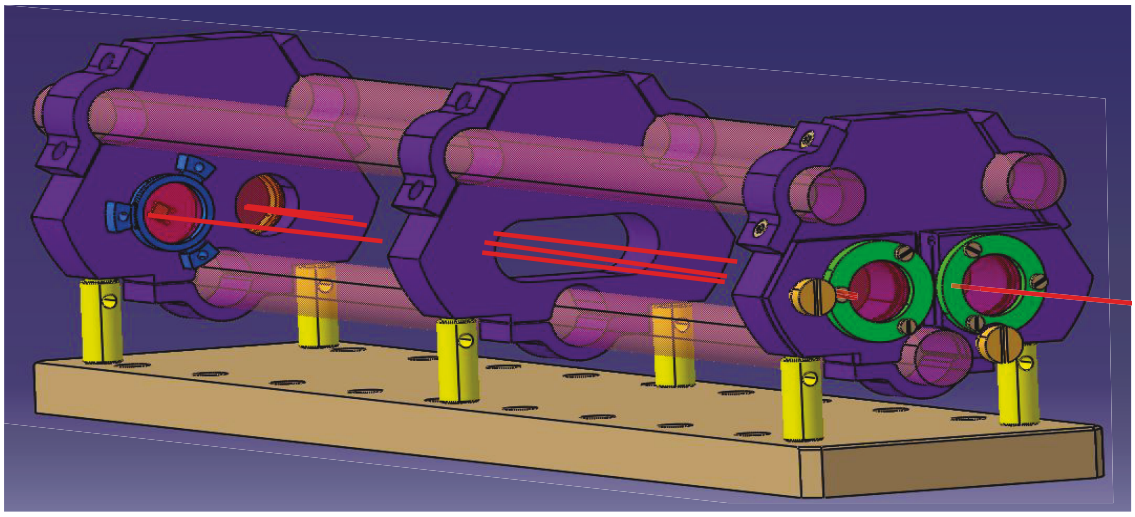

Figure 4.1: **Transfer cavity**: A 3D view of the transfer cavity sealed in a box. We can see the externally adjustable screws along with Invar mounts with very low coefficient of thermal expansion. The cavity is sealed under vacuum to minimize perturbations from temperature and moisture fluctuations.

4.2.1 Transfer cavity

The transfer cavity has a Z type configuration with a total expanded length of 1.5 m. A free spectral range of only 110 MHz means one can lock the laser to any frequency with the help of double pass AOMs with 50 MHz range. The mirrors have broadband coating to be able to use over a large range of infrared wavelengths from 780-960 nm. The finesse of the cavity is about ∼1000 at 780 nm and varies with wavelength. The whole cavity is placed in a hermetically sealed Dural frame under primary vacuum to minimize refractive index fluctuations due to humidity and temperature perturbations in air. The mirrors are mounted on Invar mounts linked by three Ultra Low Expansion (ULE) glass rods making the cavity insensitive to thermal variations (as shown in Figure 4.1). Each mirror has one-axis adjustment to align the cavity from outside through small apertures. The resonator is stable against high frequency noise but has to be stabilized using a reference signal. A low-voltage piezo stack is mounted on one of the mirrors for low-frequency stabilization.

Stabilizing the length of Transfer cavity

The cavity has a finesse of 1000 at 780 nm and the linewidth is measured to be $\approx 150\,kHz$. The reference signal is provided by a saturated absorption signal on the D2 crossover transition $5S_{1/2}\,F = 2 \rightarrow 5P_{3/2}\,F' = 1 - F' = 3$ of a Rb cell at 40° C. There are two ways of locking the cavity length on the reference signal. We can either lock the laser at high frequencies on the cavity by feedback mechanism. To compensate for low frequency drifts the laser is locked onto the saturated absorption signal which stabilizes the length of the cavity at the same time. We can also lock the cavity length by using the reference from the atomic transition and then lock the laser completely on the cavity. We found the first mechanism more stable over long term and hence we used the two way lock Figure 4.3.

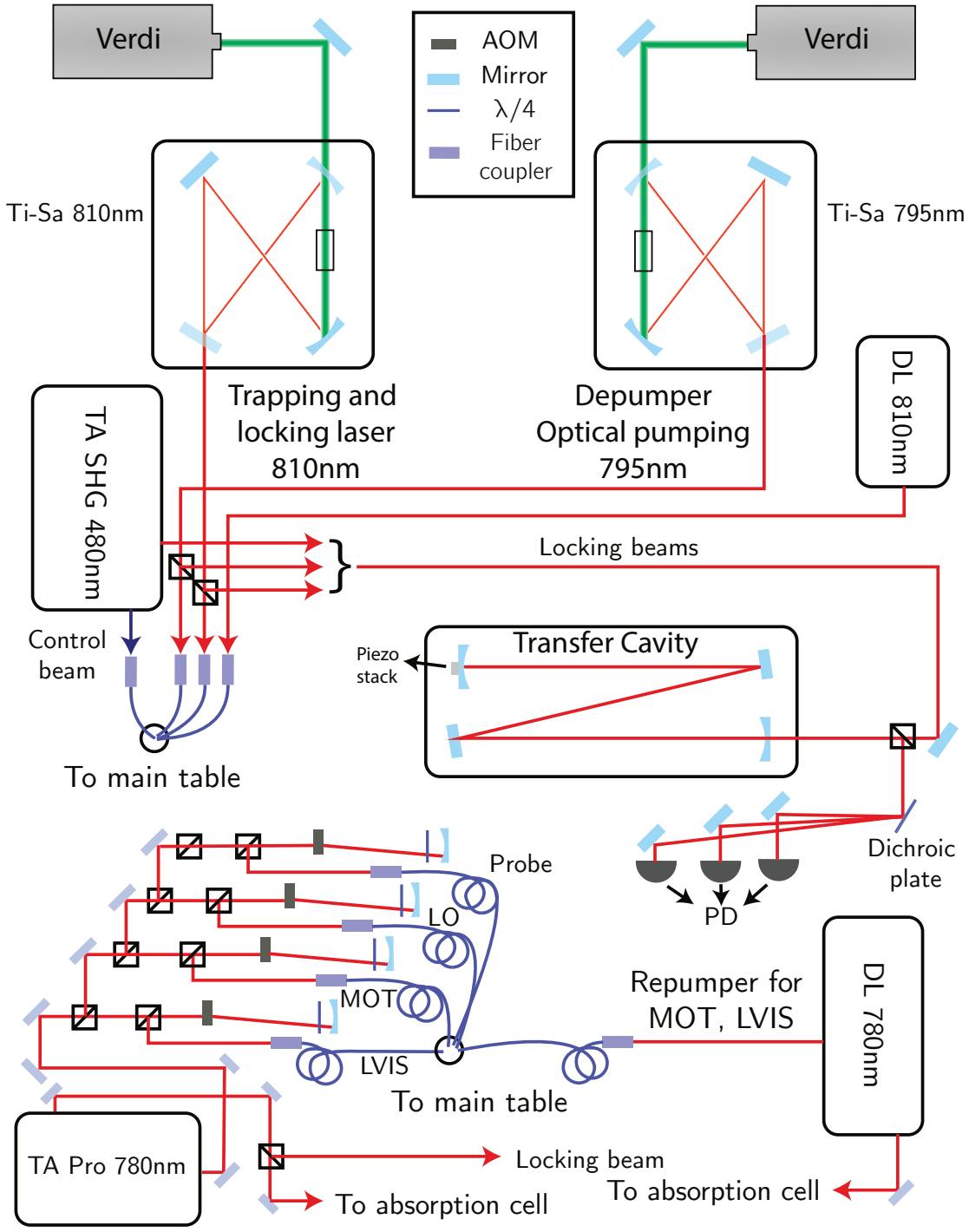

Figure 4.2: **Laser system and the path various optical beams**: Schematic representation of various lasers present on the laser table. All the optical beams are transferred to the experiment via fibers.

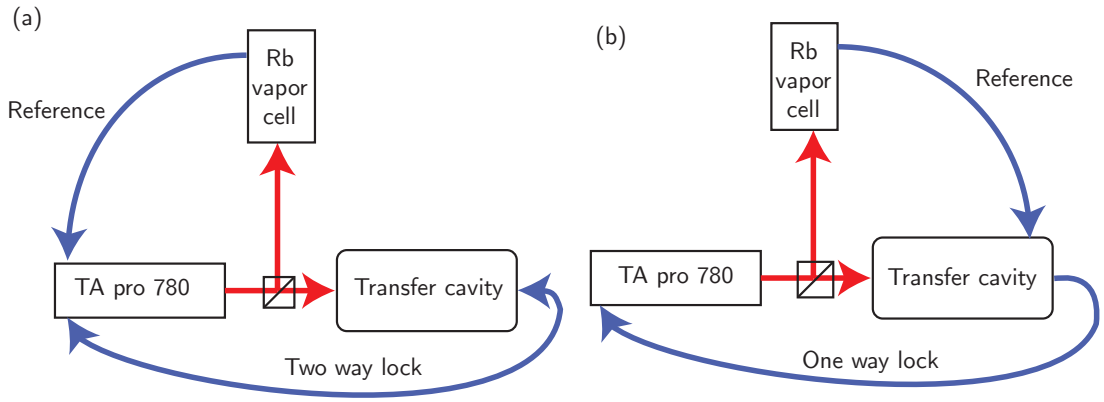

Figure 4.3: **The locking schemes for transfer cavity and master laser** (a) The master laser is locked using both the transfer cavity and the saturated absorption signal to compensate for high frequency and low frequency drifts, respectively. (b) The master laser is locked only on the transfer cavity, which is stabilized with saturated absorption signal.

Parameter	Value
Auxilary beam for locking	780 nm
Modulation frequency	21 MHz
FSR	110 MHz
Finesse	1000 @ 780 nm
Cavity frequency stability	± 15 kHz

Table 4.3: **Transfer cavity**

4.2.2 Characterization tests

In this section, we will describe the various characterization tests performed to measure the stability of the transfer cavity locking scheme. This method has been chosen and designed for its flexibility to freely lock at any required frequency simply by using AOMs. However, the linewidth of the transfer cavity is only 150 kHz which limits the precision we can achieve on the laser frequency.

Stability of the transfer cavity

To measure the stability of the transfer cavity's length, we use a reference laser which is frequency stabilized on a very high finesse cavity. The reference laser has a linewidth of < 10 kHz and drifts about 10 kHz/day. We measure the reflection signal from our transfer cavity when its resonant frequency is about 100 kHz (half the transfer cavity's linewidth) away from the laser. The half power points on the side of resonance are most sensitive to any fluctuations in resonator's length. The histogram of the reflected intensities fits well for a cavity whose resonance has a

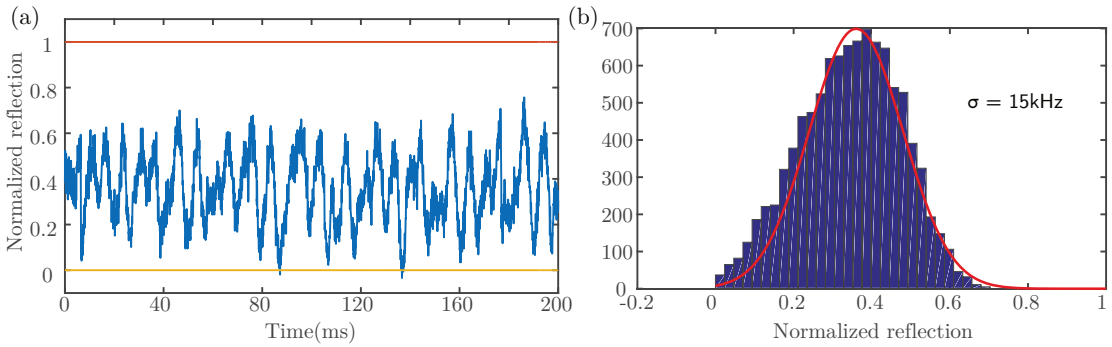

Figure 4.4: **Transfer Cavity Stability**: (a) We used a laser whose frequency is stabilized using a very high finesse cavity from another experiment. We measure the reflection signal of the transfer cavity on resonance and about half linewidth away from it to quantify the stability.(b) The histogram of the normalized reflection signal was compared with an emulated (red curve) reflection from a cavity whose resonance is fluctuating with a standard deviation of 15 kHz.

standard deviation of 15 kHz.

4.2.3 Stability of lasers

We measured the stability of our blue laser lock by interfering with another one locked on a very high finesse cavity. The results indicate that the locked blue frequency is fluctuating between two values. The presence of two near-by resonant

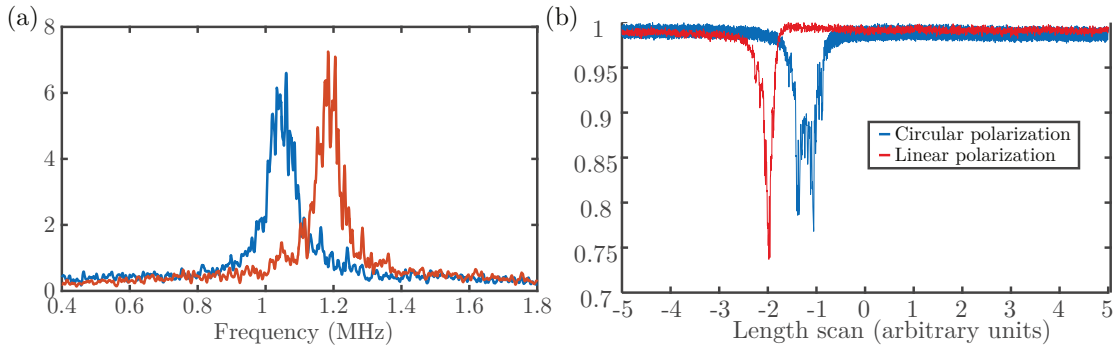

Figure 4.5: **Blue laser frequency stability**: (a) The spectrum of beating between the blue laser in our system with another one locked on a very high finesse cavity. The two curves correspond to two different instants which indicate that blue frequency is oscillating between two frequency points. (b) **The reflection signal from transfer cavity.** The red curve indicates the signal observed using a linear polarized light. The blue curve was observed using a circular polarized light and it explains why the beating spectrum is fluctuating between two frequency points.

frequencies (separated by ∼150 kHz) is caused by the non-orthogonal incidence of light on the dielectric mirrors of the cavity. Due to this the S and P polarizations don't experience the same phase shifts, which results in two different eigen modes

of transfer cavity. In the Figure 4.5 (a) we plot the spectrum of the beating signal between our blue laser and a reference one. We observed that the frequency of the blue laser was oscillating between two values. The origin of the problem can be seen in Figure 4.5 (b), where we can see that the reflected light (blue) from the transfer cavity exhibits bimodal reflection.

The problem is caused due to the specific way we separate the reflected light from the incoming one. We use a quarter wave plate and a PBS to separate them, which couples a circularly polarized light to the cavity. To circumvent this issue, we replace the quarter wave plate with a Faraday isolator which rotates the polarization by $\pi/4$ but maintains the polarization linear. With the new system, the measured linewidth of the blue laser is 50 kHz. Since we use 960 nm to stabilize the frequency, the linewidth is larger after the doubling system.

4.3 Control/Acquisition setup

Cold atomic experiments require a precise control of the timing, frequency and power of various lasers. The preparation and manipulation of atoms take place at vastly different time scales, from few seconds for atom loading to few microseconds for pumping. In this section we will describe the control software and data acquisition system which are necessary to synchronize various elements of our setup.

4.3.1 Hardware components

The frequency and the power of lasers are controlled by acoustic optical modulators (AOMs) before being coupled to a fiber. Each optical beam typically passes twice through a dedicated AOM (MT-80 or MT-110 from AA Opto-Electronic) to minimize power losses while changing its frequency settings. They are supplied by radio frequency signals (RF) from two different kinds of digital synthesizers - one with static control of power and frequency, while the other one is equipped with active control of the power and frequency. The static RF supply is handled by two modules of Novatech 409B (0.0 Hz to 171 MHz, in 0.1 Hz steps) with 4 RF channels each. The active RF frequency is produced using 4 Acquitek Synth300 cards with advanced control operations. Each card consists of two Direct Digital Synthesizer (DDS) outputs (100 kHz-300 MHz, in steps of 0.233 MHz). Each of them can be programmed to ramp or switch between various frequencies, which are essential for cooling and probing atoms. The RF signals are then sent through RF attenuation control box before being sent to a fixed amplifier, which allows us to switch them on/off and control its powers through digital and analog inputs, respectively.

To generate a control sequence we use a custom made National Instruments PXI controller. The analog control signals are generated using a DAQ analog PXI-6713 (1 MHz),6722(180 kHz). Analog acquisition is carried out using a DAQ: PXI-6143 (250 kHz) card. The slow analog input is used for monitoring the powers in probe and the trapping beams. The digital control is provided by FlexRIO FPGA PXIe-7962R bases with a resolution time of 10 ns. We use a fast input module (AI NI 5761, 4x250 MHz analog inputs, 14bits) to acquire fast analog data like homodyne detection signal of small scale photon data. A fast digital input/output module (DIO NI 6581, 54x100 MHz) is used to store various waveforms which allows us to create pulses of different shapes, and also to acquire data from Single Photon Counting Modules (SPCMs). In addition, we use 8 PID boxes to actively stabilize the lasers and different resonators on the setup.

4.3.2 Software

Cold atom experiments require complex set of instructions to control various elements over very short time scales. The resolution times for various elements is different and care has to be taken to optimize the control sequence without running into problems like overflowing the buffer space of the computer while saving large amounts of data. We use two different Labview programs to control the DDS channels and to design the experimental sequence.

RF control software

To control the RF sources a Labview program based on client-server type architecture is used. Using the client interface, we can input the static as well as dynamic frequency settings for Synthia and Novatech synthesizers. The server converts the settings to machine coded signals which creates the required frequency at the DDS channels.

Experiment software

Given the specific settings of our experiment we must have control over times scales from few nanoseconds until few minutes during which the atoms are loaded and probed over thousand times. The experiment is automated from the loading of atoms until the data acquistion using a Labview software. This program was developed specifically for our experiment by M.H. Pottier from Arcale, and further improved by us to suit our experimental requirements.

The program has several modules which are integrated on an Field-Programmable Gate Array (FPGA) chip which enables fast input/output data processing. The program has two main stages - in the first stage the FPGA circuit is hard coded with the instructions along with any conditional loops, and in the second stage the

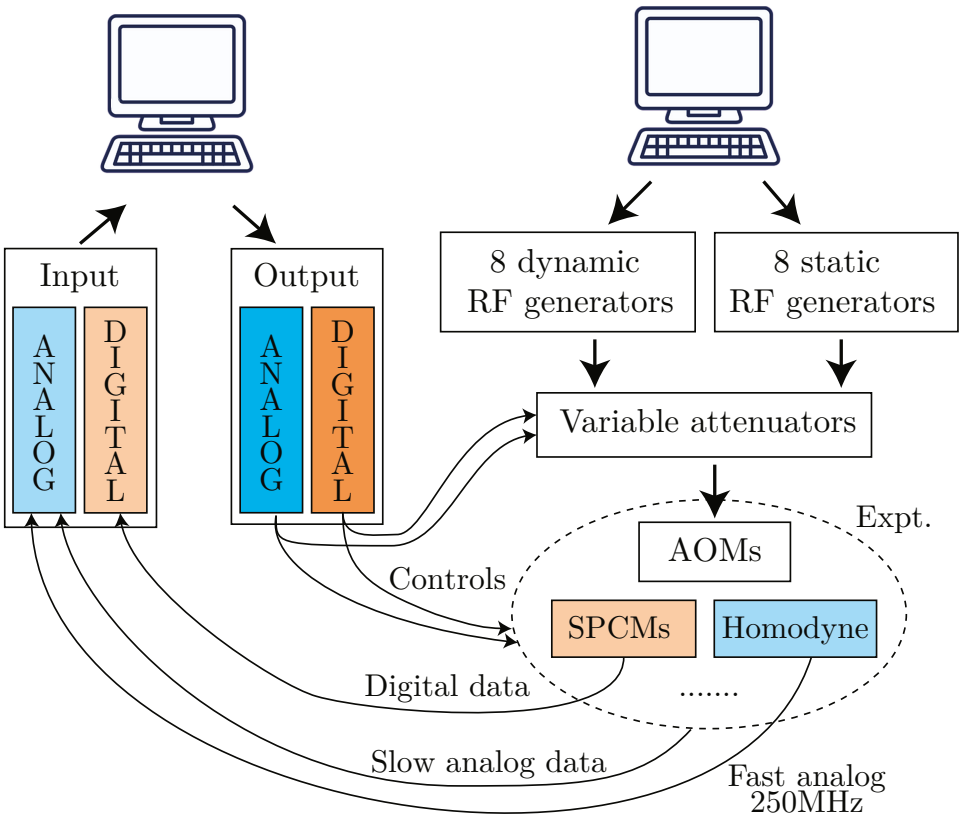

Figure 4.6: **Schematics of the acquisition system**: Two different computers are used to provide complete control over various elements. One of them is used to control the Direct Digital Synthesizers(DDS) while the other one generates/acquires the data from the experiments.

program can be executed in a set of cycles either for a specific number of times or continuously without any delay within the cycles.

The software provides graphical user interface where the sequence can be configured in three main steps. The main steps in cold atomic experiments consists of atomic cloud trapping (using magneto-optical traps, dipole traps), cooling (molasses), preparation in a specific configuration and measurement.

1. In the first step, the digital/analog channels which are necessary for the experiment are selected. The physical addresses are mapped to virtual names using a configuration file which is loaded with the software. The sequence only runs the necessary channels which are required for the experiment.

2. A typical experimental sequence may not necessarily be unidirectional for e.g. some measurement steps might need to be executed multiple times once the atoms are prepared. The atomic cloud preparation can take upto 100 milliseconds and doesn't require further loading until the lifetime of the cloud (upto 10 ms). During this time the measurement and preparation steps might have to be repeated a large number of times like as illustrated in Figure 4.7.

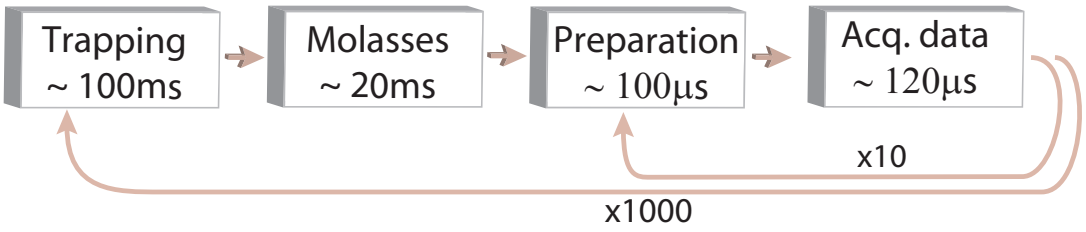

Figure 4.7: **Experimental sequence**: A typical experimental sequence which can be programmed to run where certain parts are executed under logical conditions, and others are executed a certain number of times before the whole cycle is repeated

3. Finally each channel has to be configured for each step individually. The digital channels can be programmed using Time High (TH), Time Low (TB), delay time (dt) and Number of times (Nb) settings. In each step the following sequence is generated for 'Nb' times (high for TH and low (TB+dt) ...). The analog channels are equipped with ramp, constant and waveform inputs which can be used to create arbitrary functions easily.

All the operations are then converted into FPGA code which can then handle all channels simultaneously with 100 MHz update rate. This enables us to create logical operations which are otherwise hard to implement. For e.g. it would allow us to implement a sequence which must be executed upon a trigger like a detection event on a photon counter. In addition, there are some necessary features for proper functioning of the experiment such as virtual digital controllers, which are important when one needs to perform logical gating operations like triggering data acquisition

upon detection of certain event. As the single photon detectors cannot be switched on/off at time scales smaller than few ms, the virtual digital channels provide us with necessary control with minimum noise from the background signals.

Chapter 5

Atomic setup

Contents

5.1 Atom cloud preparation 45
5.2 Magneto Optical Trap 46
5.3 Low Velocity Intense Source (LVIS) 47
5.4 Main atomic cloud 48
5.4.1 Optical molasses 49
5.4.2 Imaging system 49
5.4.3 Temperature measurements 51

The main experimental requirement to observe strong non-linear effects with Rydberg EIT setup is to have large atomic density to achieve significant optical depth on photonic fields. In hot vapor cells it is possible to achieve high atomic densities but the blockade effect is significantly affected by rapidly moving atoms [82]. Hence, we chose a cold atomic system capable of going below the Doppler limit. To have the frozen gas approximation valid, the Doppler broadening mechanism should be much smaller than the Rydberg induced energy shifts. To fulfil the above criteria, we trap a cold atomic cloud which can reach densities of 10^{10} cm^{-3} at temperatures below 50 μK. In this chapter, we will describe how we prepare and characterize our cold atomic cloud.

5.1 Atom cloud preparation

We work with Rubidium Rb^{87} atoms because of easily available diode lasers for addressing its optical transitions. We create Rb vapor by heating a Rb salt upto 50° C. The atoms are first trapped using a magneto optical trap (MOT) and can be easily cooled down to ≈1 mK.

The experimental apparatus consists of two vacuum chambers - auxiliary and science chamber connected by a differential tube. This tube helps to maintain a pressure ratio of 100 between the two chambers. The auxiliary chamber acts as a source of low velocity atoms for the main trap in the science chamber and is

significantly smaller than the other one. The experimental chambers are illustrated in Figure 5.1. In typical MOT systems, where the atoms are loaded from background pressure, it can take upto few minutes to load a significant number of atoms. By using an auxiliary trap we can achieve upto 10^9 atoms in a few seconds.

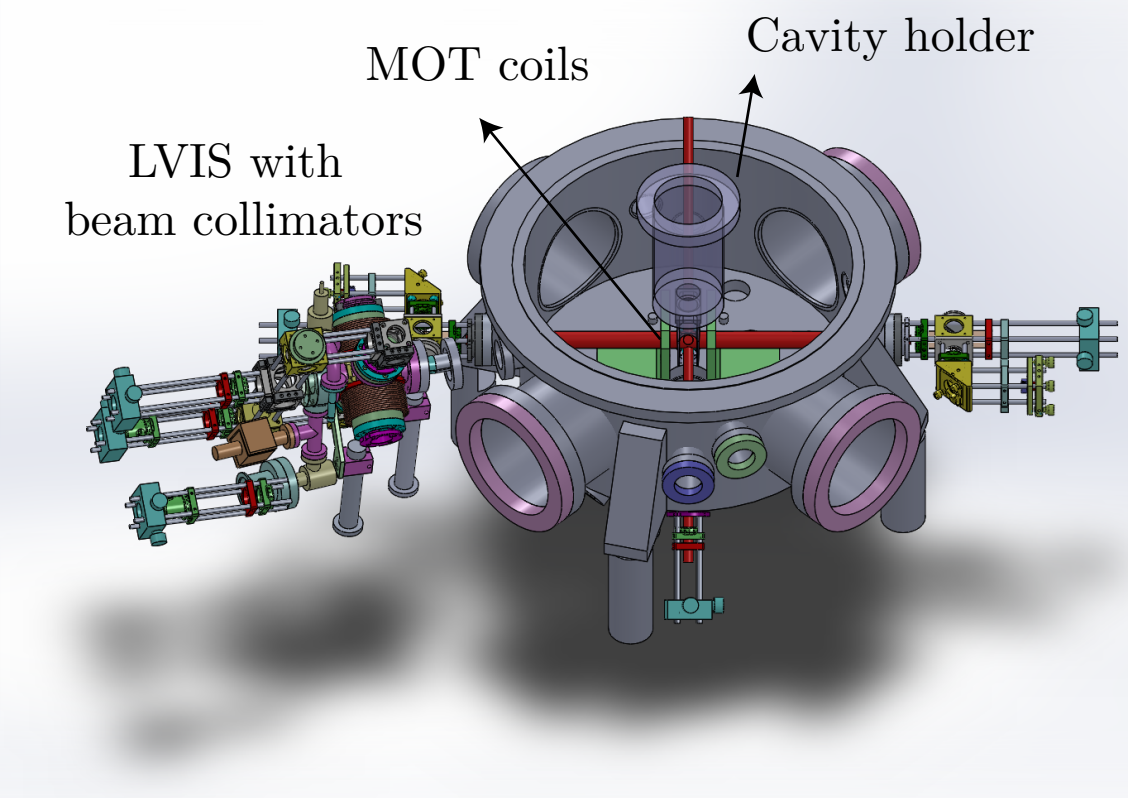

Figure 5.1: **An illustration of LVIS and the main chamber**: The LVIS chamber consists of auxiliary MOT where the atoms are trapped and transfered to the main chamber trap. Here we illustrate the LVIS trap beam collimators along with the position of the cavity holder and MOT coils in the main chamber.

5.2 Magneto Optical Trap

Atoms are captured and trapped using a standard magneto optical trap (MOT) [83,84]. The atoms are laser cooled using a cooling laser tuned to near resonance on D2 transition $5S_{1/2}\,F = 2 \rightarrow 5P_{3/2}\,F' = 3$ while the resonant repumper $5S_{1/2}\,F = 1 \rightarrow 5P_{3/2}\,F' = 2$ is used to bring the atoms back to $5S_{1/2}\,F = 2$. Both the beams are locked on crossover resonances and then frequency shifted close to resonance using AOMs (The schematics of the locking transitions are illustrated in Appendix A). All the cooling beams are red-detuned by 18 MHz ($3\Gamma_e$) and each one of them has an intensity of $5\,\mathrm{mW/cm^2}$ at the center.

The trap consists of six large independent beams of $\sim 1\,\mathrm{cm}$ diameter created using beam collimators mounted on a Thorlab 30 mm optical cage system. The beams are produced using two stable Schäfter-Kirchoff variable fiber splitters with

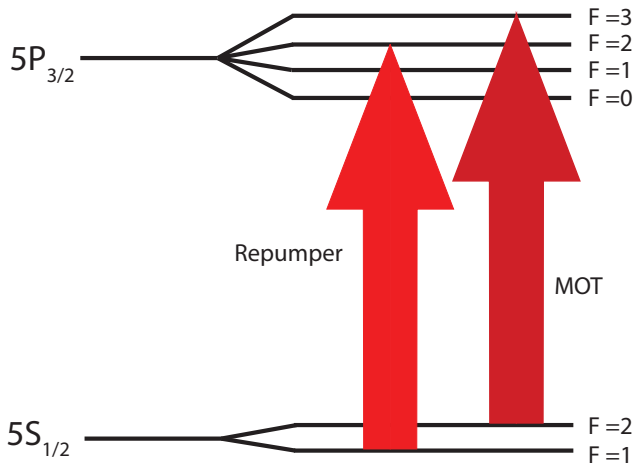

Figure 5.2: **Excitation scheme for MOT**: The trapping beams are excited on the D2 transition at 780 nm. The MOT trapping beam is red detuned by 18 MHz on transition $5S_{1/2}$ F= 2 $\rightarrow$ $5P_{3/2}$ F=3. The repumper beam is on resonance with the transition $5S_{1/2}$ F= 1 $\rightarrow$ $5P_{3/2}$ F=2.

six outputs. Both the repumper and the cooling laser are coupled into the same optical fiber and split equally into each beam. A magnetic trap is created using two trap coils to create a field gradient of 5-10 G/cm in anti-Helmholtz configuration. A set of three pairs of compensation coils are used to cancel any stray field and helps in positioning the center the trap on the cavity mode.

5.3 Low Velocity Intense Source (LVIS)

The experiments we performed are schematically described in Figure 5.1. The pressure in the LVIS chamber is maintained at 10^{-8} mbar using a small ion pump of 2 l/s (Agilent Model 919-0520) later on replaced with a 3 l/s ion pump (Gamma vacuum model 3S). We load atoms into the auxiliary trap called Low Velocity Intense Source (LVIS) [85], where the atoms are trapped in a similar way as a Magneto-optical trap using three pairs of orthogonally polarized laser.

As shown in Figure 5.3 one pair of trapping beams are created using retro-reflection from a mirror (and a quarter wave plate) with a small orifice. The atoms are not trapped in the cylindrical hole of the retro-reflected beam and are pushed through the differential tube on the chamber wall. The former beam acts as a pusher to create a steady stream of atoms. The position of the LVIS trap is set in such a way that the atoms are pushed towards the main optical trap region.

This way of creating atomic beam has several advantages over conventional background loading such as fast loading and easy tunability of atom number. In typical MOT system one needs to change the power in the trapping beams or the gradient of the magnetic field to increase the loading. But using this setup, we can control the number of atoms by keeping the main trap parameters constant by increasing the magnetic field gradient of the LVIS trap.

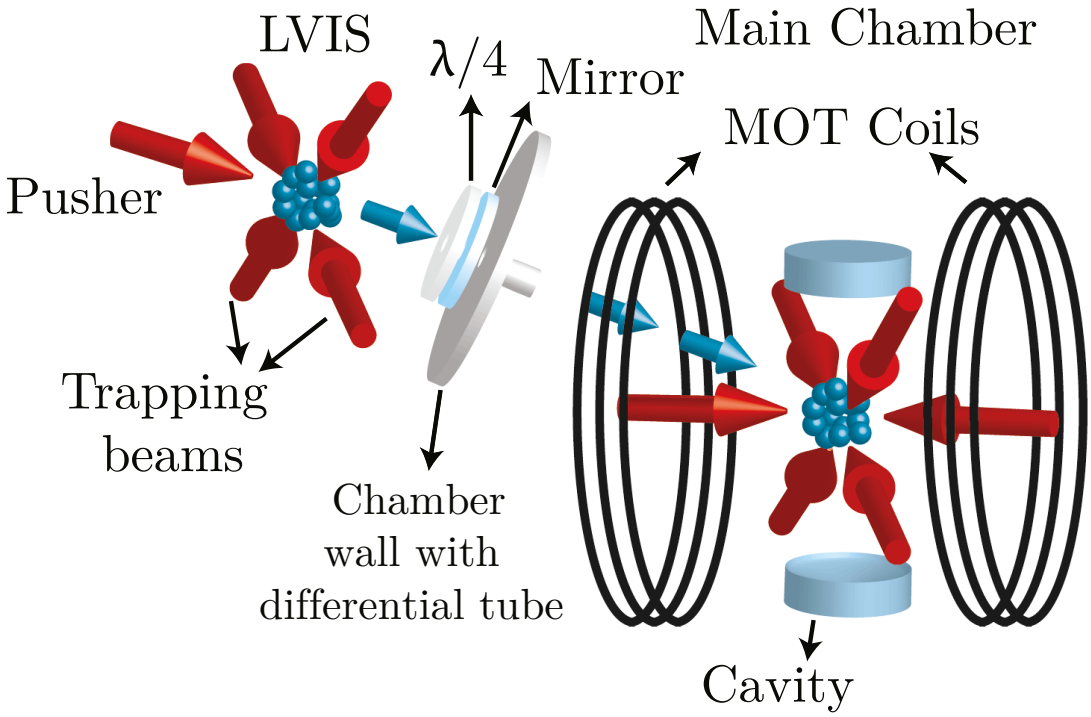

Figure 5.3: **LVIS and MOT traps along with the atomic beam:** The atoms are trapped using LVIS trap where one of the beams is a retro reflected beam with a hole in the center. The atomic beam enters the main chamber through a differential tube and loads the main atomic trap. The cavity is positioned vertically parallel to the MOT coils.

In addition, we can control the position of the LVIS cloud by changing the balancing of the beams. If the atomic position is not on the axis of the differential tube then the transfer efficiency is low. Hence, its position is adjusted based on the number of atoms in the main trap.

Parameter	Value
LVIS trap beam size	1 cm
LVIS trap detuning	-18 MHz
Chamber pressure	$\sim 10^{-8}$ mbar
LVIS trap to main trap distance	30 cm

Table 5.1: **LVIS chamber parameters.**

5.4 Main atomic cloud

The primary trap is located in the science chamber which is pumped down to 10^{-10} mbar using an ion pump (Varian VacIon Plus 300, model 919-2641 fitted with a cryopanel). The atoms from LVIS trap flow towards MOT at a speed of 9 m/s.

By optimizing the position of the LVIS cloud, we can upto $3*10^9$ atoms per second. This allows us to load about 10^9 atoms in a characteristic time of ~ 4 seconds.

Parameter	Value
Trap intensity	$5\,\mathrm{mW/cm^2}$
Magnetic field gradient	5-10 G/cm
Main chamber pressure	1-5.10^{-10} mbar
Cloud size	0.1-1 mm
Steady state loading	10^9 atoms

Table 5.2: **Main chamber parameters**: The laser trap parameters are similar to LVIS trap

5.4.1 Optical molasses

After the atoms are trapped in MOT, the temperature of the cloud is measured to be around the Doppler temperature of 150 μK. The atoms are further cooled down using the radiation pressure of MOT beams, this technique is known as optical molasses. Using this method, sub-Doppler temperatures can be achieved because of spatially varying radiation fields experienced by the atoms [86, 87]. A typical optical molasses sequence requires the magnetic traps to be turned off and the cooling lasers are reduced while they are moved away from the resonance. The final sequence is optimized for maximum trapping efficiency and lasts for 6 ms. During the first 3 ms the cooling laser's frequency is ramped from -18 MHz to -48 MHz from resonance and then kept constant for the remaining time. In the last 3 ms, its power is reduced by a factor of 10 linearly. The final temperature after the optical molasses can be anywhere between 30-50 μK depending on the loading parameters.

5.4.2 Imaging system

The trapped atoms are imaged by shining a near resonant beam on to the atoms. The fluorescence from the atoms depends on various parameters like Intensity, detuning etc of the incident beam . The scattering rate of one atom is calculated using

$$S_1 = \frac{I/I_{sat}}{1 + \Delta^2/\gamma_e^2 + I/I_{sat}}\gamma_e \tag{5.1}$$

Where the I_{sat} is 1.64 mW/cm^2, γ_e is $2\pi\,3$ MHz for the D2 transition of ^{87}Rb and Δ is the detuning of the imaging laser. Now we can compute the number of atoms N_a from the photons detected by the camera (N_{det}) from

$$N_a = \frac{1}{\eta_{coll}}\frac{g}{\eta_{CCD}}\frac{1}{\eta_{trans}}S_1\frac{1}{t_{exp}}N_{det} \tag{5.2}$$

Where η_{coll} is the collection efficiency , η_{trans} is the transmission efficiency and η_{CCD} is the detection efficiency of the camera, t_{exp} is the exposure time and g

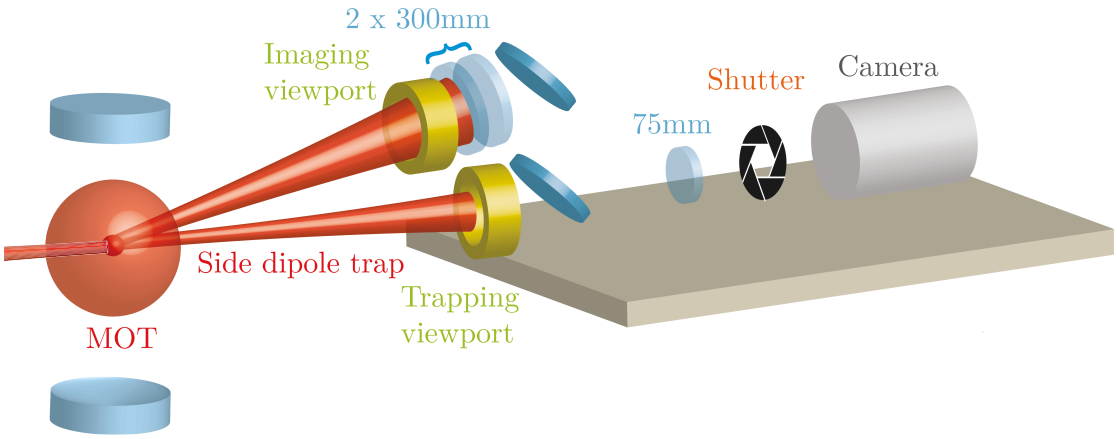

Figure 5.4: **Imaging setup**: A new imaging setup has been designed which would allow us to image clouds that are few tens of microns in diameter. The imaging system consists of two 300 mm doublets which replicate the cloud with 1:1 magnification. A 75 mm concave lens is used to magnify the image by 2.7.

is the adjustable gain on the camera. We use a princeton camera PIXIS 400BR for imaging. Even though it has a very high efficiency of 98 % when cooled to $-70°$ C, the pixel length is limited to 20 μm in size. The first imaging setup on the experiment was designed to image large clouds of 0.5 mm to 2 mm. So, the magnification ratio was limited to only 0.5 as the size of the CCD chip of the camera is only 1340x400 pixels i.e. about 27 mmx8 mm. For the Rydberg experiments we needed to prepare an atomic cloud of 30-50 μm. To characterize this small cloud we had to redesign the old imaging setup, which has a resolution limit of 80 μm. Given that the nearest viewport from the cloud is at 30 cm it limits the how close a lens can be placed from the cloud and the viewport is only 2 cm in radius hence the light collection efficiency is estimated to ≈ 0.1 %.

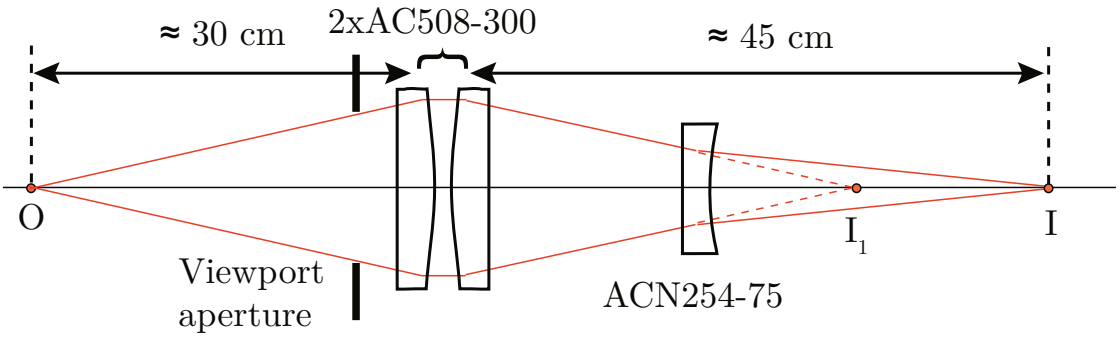

Figure 5.5: **The imaging scheme**: Two doublet lenses are choosen to reproduce the object 'O' with minimum aberrations at position I_1. A final doublet lens (ACN254-75) of -75 mm is used to magnify the image by 2.7 times at new position I. This image is reproduced from Erwan's thesis [78].

We use two doublet lenses of 300 mm placed at 30 cm away from the cloud to

image at 1:1 magnification. Then we use a negative doublet at -75 mm to further magnify the image. The final lens is positioned to achieve a magnification of $\approx$ 2.74$\pm$ 0.05 times while minimizing the aberrations. The new setup has a resolution limit of only 8 microns while still having the capability to image 1-2 mm clouds. The imaging setup has been designed with the help of Tikai while he was an internship student and is described in more detail in his report.

5.4.3 Temperature measurements

To estimate the temperature of the cloud, we use the standard time of flight measurements [87]. The radius of the cloud at any given time depends on the time of expansion and initial equilibrium temperature of the MOT. By considering the Boltzmann distribution for the velocity of atoms the cloud size can be estimated using the following equation [87]

$$\sigma(t) = \sqrt{\sigma_0^2 + \frac{k_B T}{M} t^2}$$

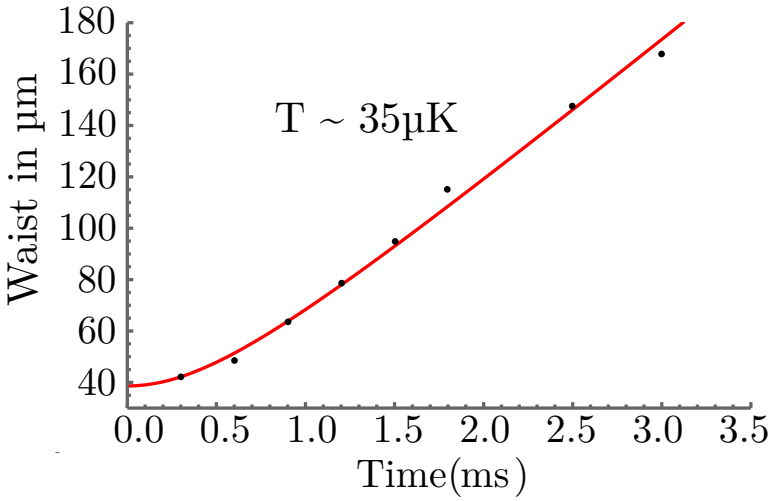

Figure 5.6: **The variation of cloud size with time**: By fitting the cloud expansion we can estimate the temperature of the cloud.

By measuring the size of the cloud at different times we estimate the temperature of the cloud. After performing the molasses, the cloud's temperature is about 35 μK which is much below the Doppler limit. The maximum density of the cloud can reach upto $\sim$ 0.05 atoms/ μm^3. One of the future goals is to implement 'dark' MOT cycles which would allow us to further increase the density by minimizing the repulsive forces between the atoms due to rescattering [88].

Chapter 6

Detection system

Contents

6.1 Second order correlation measurement 53
6.1.1 Photon statistics 54
6.1.2 Experiment 54
6.2 Homodyne Tomography 56
6.2.1 Phase locked experimental setup 58
6.2.2 Squeezing measurements in transmission 61
6.3 Conclusion 64

Rydberg-Rydberg interactions in a resonator can be used to convert coherent states into non-classical ones and hence require sophisticated detection systems to characterize them [89]. In this chapter we will describe how we measure the photon statistics, phase, and the squeezing spectrum of an optical beam.

6.1 Second order correlation measurement

To understand more details about the physics of the system it is necessary go beyond simple linear detection systems. A normal photo diode can only measure average intensity and cannot distinguish between different photon number components of a signal beam. To determine the quantum statistics of the light we measure the second order correlation function. If we assume that the incoming signal beam is invariant under time translation, then the normalized second order correlation function $g^{(2)}(\tau)$ is given by [51]

$$g^{(2)}(\tau) = \frac{\left\langle \hat{a}^\dagger(0)\hat{a}^\dagger(\tau)\hat{a}(\tau)a(0)\right\rangle}{\left\langle \hat{a}^\dagger(0)\hat{a}(0)\right\rangle^2} \tag{6.1}$$

where $\hat{a}(\tau)$ is the annhilation operator on the signal mode at time τ. By using a number operator $\hat{N} = \hat{a}^\dagger\hat{a}$ we can rewrite the $g^{(2)}(0)$ by

$$g^{(2)} = \frac{\langle\hat{N}^2\rangle - \langle\hat{N}\rangle}{\langle\hat{N}\rangle^2} = 1 + \frac{\Delta\hat{N}^2 - \langle\hat{N}\rangle}{\langle\hat{N}\rangle^2} \tag{6.2}$$

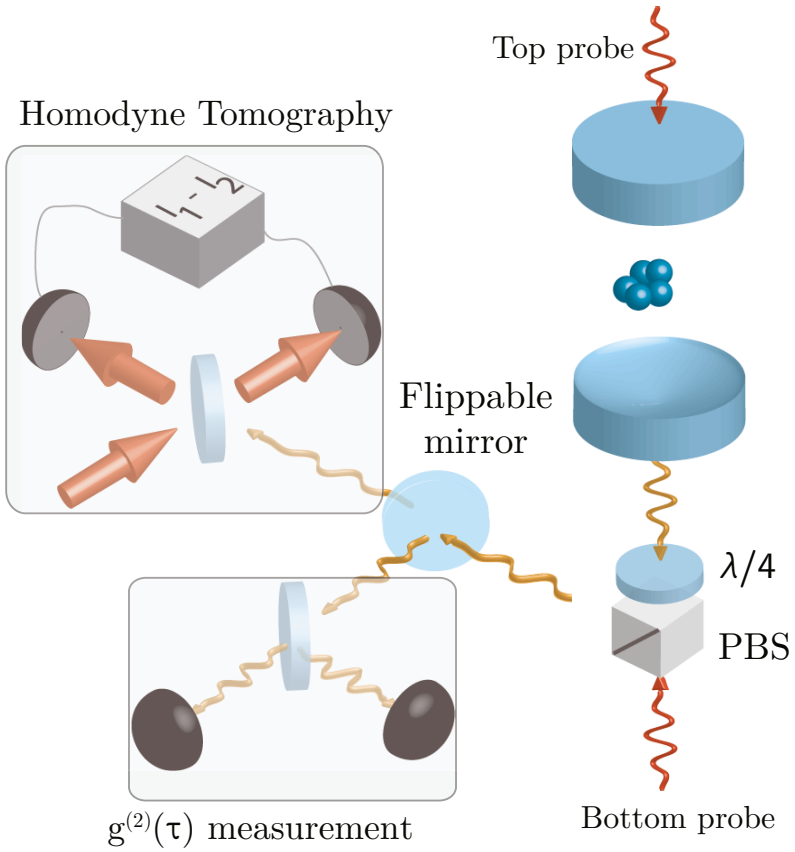

Figure 6.1: **Detection path for photons**: The detection path of the optical light from the cavity is designed to be able to freely switch between the $g^{(2)}$ measurement and the Homodyne tomography. The probe light can be sent to the cavity either from the top or the bottom. When sent in reflection, we use a polarization beam splitter (PBS) and a quarter wave plate to separate the input from the output.

6.1.1 Photon statistics

Cross correlation $g^{(2)}$ measurements are performed to determine the photon statistics of the light. Any classical laser beam is usually referred to as coherent light with $g^{(2)}(\tau) = 1$, while thermal light has super-Poissonian statistics with $g^{(2)}(\tau) > 1$ at short time scales. The classical description of light sets minimum limit of 1 for any kind of optical light. It can be shown that with quantum description one can go below the classical limit and have $g^{(2)}(\tau) < 1$ and the first experimental observation of anti-bunching statistics was carried out in Kimble's group [90]. Hence, this function provides information about photon number distribution in any optical beam, which can be used to quantify the bunching ($g^{(2)}(\tau) \geq 1$) or anti-bunching ($g^{(2)}(\tau) < 0$) nature of the light.

6.1.2 Experiment

We use a Hanbury-Brown Twiss type setup (refer Figure 6.2) to measure the correlation/anti-correlation effects in our signal beam [91]. The output field of

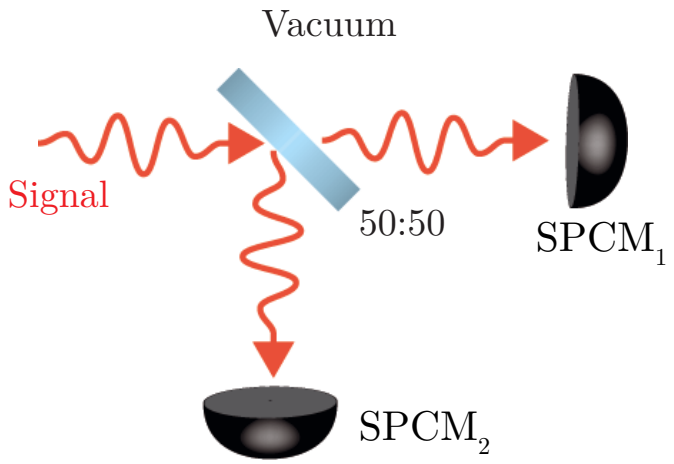

Figure 6.2: **Hanbury Brown Twiss type Interferometer to measure Intensity correlations**: The signal beam is incident on a 50/50 beam splitter and we measure the cross-correlation between the two output arms using two single photon counting modules (SPCMs).

the cavity is sent to a 50:50 beam splitter and two detectors are placed at the two output arms to measure the intensity correlations between them. It can be shown that measuring $g^{(2)}(\tau)$ is equivalent to $\frac{\langle a_1^\dagger(0)a_2^\dagger(\tau)a_2(\tau)a_1(0)\rangle}{\langle a_1^\dagger(0)a_1(0)\rangle\langle a_2^\dagger(0)a_2(0)\rangle}$ where 1 and 2 denote the two output modes. To evaluate the correlations between the detectors at the same time one can use the following expression $g^{(2)}(0) = \frac{\langle \hat{N}_1\hat{N}_2\rangle}{\langle \hat{N}_1\rangle\langle \hat{N}_2\rangle}$

The light from the cavity is collimated and filtered to reject any background photons from sources like the trapping beam, etc. It is then incident on a 50/50 beam splitter and intensity correlation between the two output paths are measured using single photon counting modules (SPCMs; Perkin-Elmer SPCM-AQR-12-FC). The counting modules creates a 20 ns pulse for every detected photon and a dark count rate of 50 counts/sec The specified quantum efficiency at 800 nm is 65 % and the dead time is 30 ns. It is important to note here that the quantum state measured using avalanche on/off photodiodes doesn't exactly give us the true $g^{(2)}$ value. It is only possible to distinguish between zero and 'one or more photons' event. It can be possible to design a photon-number resolving detectors using multiple on/off detectors [92]. But if the probability of having more than one photon in the same spatio-temporal mode is low then one can still use on/off detectors to accurately measure the $g^{(2)}$ function.

The total detection efficiency from the output of the cavity until the photons are detected is 37.5±2 %, it includes the transmission efficiency from cavity to counters of 57 % and detection efficiency of the counting modules (65 %).

While analyzing the data we ignore the first few seconds of the data as the MOT needs to attain quasi-steady state loading. The $g^{(2)}$ measurement gives an accurate value as long as the photon count is below 20 counts/μs. The typical sequence consists of probe detection for 120 μs with counts between 40-100, which is well below the threshold. The measurements are insensitive to the optical losses

between the cavity and the detector.

Parameter	$g^{(2)}$ measurement	Homodyne Tomography
Characterizes	photon statistics	full density matrix
Phase sensitivity	insensitive	precise phase change
Detection efficiency	not affected by losses	direct effects
Setup	relatively simple	complex

Table 6.1: **Comparision of the $g^{(2)}$ measurement and the Homodyne detection**

6.2 Homodyne Tomography

Unlike classical particles, quantum objects are not represented by a single point in phase space but with a probability distribution called Wigner function (for more information refer to the Appendix:D). It gives access to the precise quantum state of the measured particles. The Wigner function can be measured using a technique called homodyne tomography [15]. From photon-counting measurements one

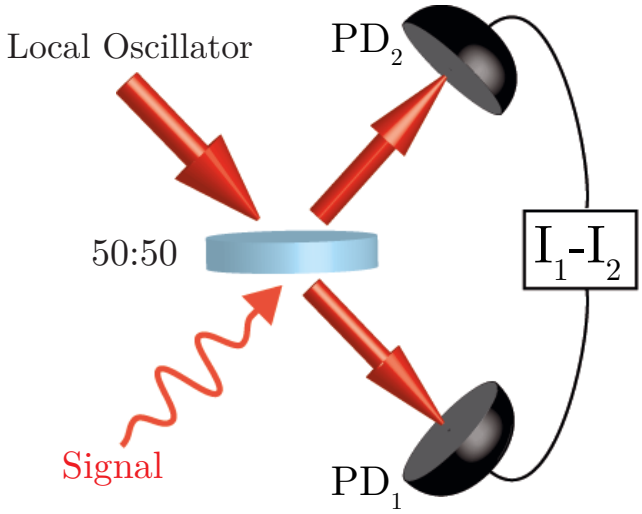

Figure 6.3: **Homodyne Tomography**: The optical signal is superposed with a Local Oscillator (LO) beam. Two low noise photo diodes are placed at the two output arms. The difference in the intensity is used to measured the tomography of the quantum state.

can retrieve information about the intensity correlations but it is inherently insensitive to phase fluctuations. By using homodyne measurements one can measure many properties like mode purity, phase, etc., of the photonic state however it is technically challenging to implement it. In this section, we will show how one can measure the phase shift of the retrieved photons. The optical signal we want to measure is mixed with a mode-matched strong coherent beam called local oscillator ($\alpha_{LO} \gg 1$) on a 50:50 beam splitter as illustrated in Figure 6.3. The two

outputs are measured using two high efficiency low noise photo diodes (PD). The difference between the detected signals is monitored and analyzed to extract the phase, the squeezing spectrum, and also to reconstruct the density matrix using maximum likelihood algorithms. In 2013, we demonstrated that our atomic cloud can be used as an on-demand single photon source with fully controlled quantum state by characterizing it with homodyne tomography [93].

By assuming that the amplitude fluctuations of the LO are negligible compared its amplitude α_{LO}, one can show that the difference of the photodiode currents is proportional to quadrature value of the signal field i.e.

$$\hat{I}_1 - \hat{I}_2 \propto |\alpha_{LO}|\hat{q}_\theta \tag{6.3}$$

where q_θ is the quadrature value along any axis at an angle θ in phase space ($\hat{q}_{\theta=0} = \hat{x}, \hat{q}_{\theta=\pi/2} = \hat{p}$ where the orthogonal quadratures $\hat{x} = \frac{1}{\sqrt{2}}(\hat{a}+\hat{a}^\dagger)$ and $\hat{p} = \frac{1}{\sqrt{2}}(\hat{a}-\hat{a}^\dagger)$). The quadrature variables with any phase θ can be measured by setting the optical phase difference between the LO and the signal to θ. By measuring the histogram of the quadrature variables for a fixed phase we obtain the projected Wigner function.

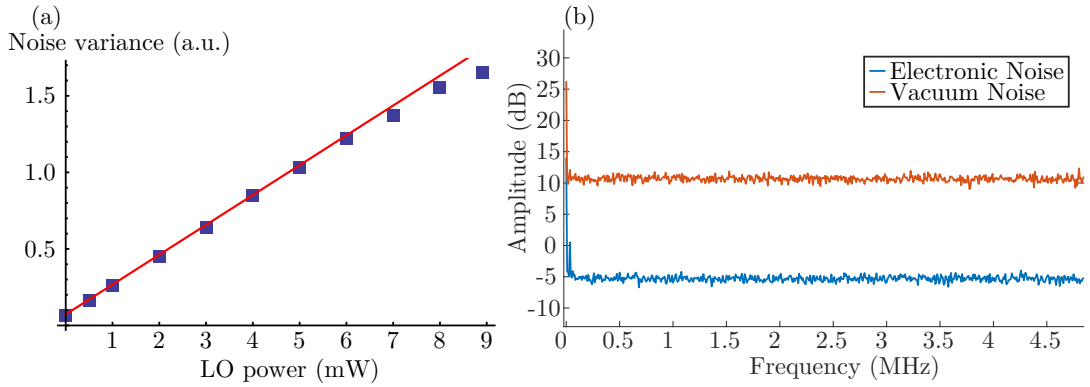

Figure 6.4: **Measurement of electronic noise level**: (a) The variance of the electronic noise is plotted against the local oscillator (LO) power. We can see that the variance increases linearly until it starts diverging above 7 mW of LO power. (b) The noise spectrum of both electronic and vacuum noise are plotted for 7 mW of LO power. The electronic noise level is 15 dB below the vacuum noise.

The larger the LO beam intensity the higher is the signal to electronic noise ratio however the detector efficiency is not linear for very large optical powers. So, we chose the maximum LO power where the detector is still linear, which corresponds to $\approx$ 7 mW. The bandwidth of the detectors is about 100 MHz, and the electronic noise is about 15 dB lower than the vacuum noise (refer Figure 6.4).

6.2.1 Phase locked experimental setup

In our experiment, we overlap a cavity mode-matched LO beam with the signal on a 50:50 beam splitter (Layertec 110895), which allows us to approximately separate the incoming beams into two output arms. The polarization dependent transmission of the glass on the photodiode, permits us to precisely tune the balancing of the light incident on the two photodiodes. By using a half wave plate we can vary the beam intensity by about $\sim 2\,\%$, which allows us to set the DC voltage of the difference signal to zero. In addition, the detectors are not orthogonal to the incoming beams to minimize back reflections on to our system. The two output arms of the beam splitter are then focussed to the homodyne detectors (low noise customized HCA-S S3883 photodiodes from Femto with an efficiency of 91 %) using two concave mirrors. In order to avoid any undesirable effects due to the dynamical response of the detector, we use a continuous local oscillator and filter the homodyne signal during data analysis.

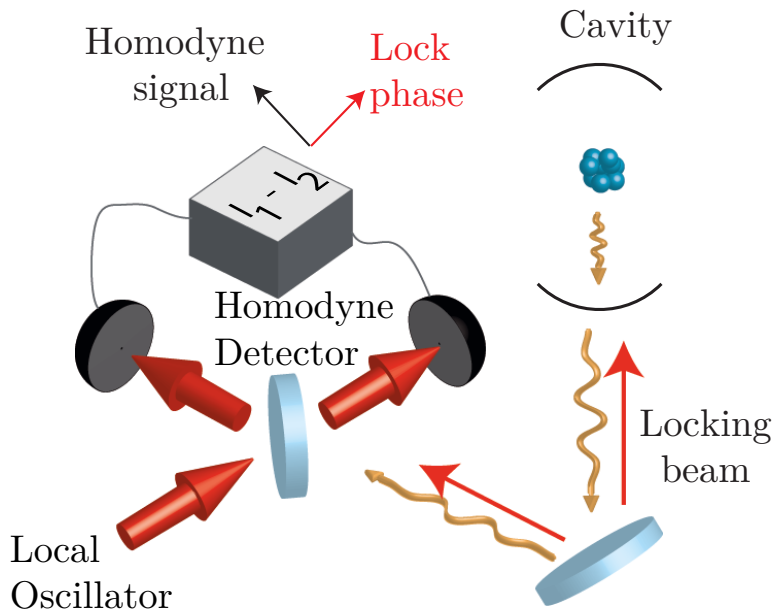

Figure 6.5: **Homodyne phase locking scheme in reflection**: A locking beam detuned from the probe by 88 MHz is used to lock the phase of the local oscillator relative to the probe. The locking beam is detuned far enough to not perturb the atoms and close enough such that it is within the bandwidth of the detector.

Locking the relative phase

In order to measure the vacuum or the Fock states, one doesn't have to actively stabilize the relative phase of the local oscillator as their Wigner functions are symmetric. But for any other type of non-classical states we must know the relative phase difference between the LO and the signal beam to measure the Wigner function.

From Andrey Grankin's calculation [47], we expect bunching/anti-bunching correlation in the probe beam reflected from the cavity depending on the parameters.

In order to lock the phase of this probe beam with respect to the LO beam, we use an auxiliary beam in the same path as the reflected probe sent to the cavity but detuned by 88 MHz. The locking beam and the probe beam pass through a single pass AOM, which is supplied by a signal $V_0(sin(\omega_1 t) + sin(\omega_2 t))$ where $\omega_1 = 212$ MHz and ω_2 =300 MHz. The auxiliary beam is rejected by the cavity and then interfered with the LO beam.

Assuming the frequency of the probe, auxiliary and LO beam is ω_0, as they originate from the same laser. After the AOM one can denote the respective fields as $E_p e^{(i(\omega_0+\omega_1)t)}$, $E_a e^{(i(\omega_0+\omega_2)t)}$ and $E_{LO} e^{(i(\omega_0+\omega_1)t+i\phi)}$. Both the probe and the auxiliary beam propagate in the same path for a distance L_1 and LO for a distance L_2. The field output at the two arms of the homodyne setup can be written as

$$E_{\pm} = E_{LO} e^{(i\omega_a(t-L_2/c)+\phi)} \pm (E_p e^{(i\omega_a(t-L_1/c))} + E_a e^{(i\omega_b(t-L_1/c))}) \tag{6.4}$$

where we replaced $\omega_0 + \omega_1$ by ω_a and $\omega_0 + \omega_2$ by ω_b. The output voltage of the homodyne signal is given by

$$\begin{aligned} V_{HD} = I_1 - I_2 &= 2E_{LO}E_p \cos\left(\omega_a \frac{L_2 - L_1}{c} + \phi\right) \\ &\quad E_{LO}E_a \cos\left(\omega_b \frac{L_2 - L_1}{c} + \delta\omega\left(t - \frac{L_1}{c}\right) + \phi\right) \\ &= 2E_{LO}E_p \cos\theta + E_{LO}E_a \cos\left(\theta - \delta\omega\left(t - \frac{L_2}{c}\right)\right) \end{aligned} \tag{6.5}$$

where $\delta\omega = \omega_a - \omega_b$ and $\theta = \left(\omega_a \frac{L_2 - L_1}{c} + \phi\right)$. This signal propagates through a cable of length L_3 and acquires an additional phase of $\delta\omega L_3/c$. It is then used by a FALC (Fast Analog Linewidth Control box from Toptica) to act on the input signal of the AOM to lock the relative phase (θ) between the LO and the probe beam. The homodyne signal is mixed with an RF signal at $\delta\omega$, which propagates through another cable of length L_4. The DC signal at the output of FALC is then given by

$$V_{mix} = V_{RF} E_{LO} E_a \cos\left(\theta + \delta\omega\left(\frac{L_2 + L_3 - L_4}{c}\right)\right).$$

By locking the above signal to zero, we can ensure that the relative phase between the LO and the locking beam doesn't vary with time. In order to change the relative phase difference between the probe and the LO by $\pi/2$ for a $L_2 + L_3 - L_4 \approx$ 20 m would require changing the frequency of the locking beam by 4 MHz. As the bandwidth of the phase lock is limited $\sim$ 100 kHz, the phase must be varied relatively slowly to measure the orthogonal quadrature.

Maximum phase lock power

Since the auxiliary beam is not very far from the atomic resonance, it entails specific constraints on the maximum allowable power one can use. There are many ways to estimate the effects of the locking beam on our system. If we start with the Bloch equations (refer to equation:2.28) and using perturbative expansion, we can

estimate the Rydberg atom population. In the lowest order of α we can assume $\sigma_{rr} = |\sigma_{gr}|^2$ [73]. The number of Rydberg atoms can be estimated from

$$N_{rr} = N\sigma_{rr} = N\frac{\tilde{g}a}{(\tilde{D}_e D_c - 2\gamma_e\gamma_c C)}, \tag{6.6}$$

where $\tilde{g} = \frac{\Omega_{cf}g}{2D_s}$, $a = \sqrt{\gamma_c}\alpha_{in}$ and for a given input power P_{in}, the photon rate $\alpha_{in} = \frac{P_{in}}{\hbar\omega_p}$.

For a typical experiment we have a C = 10, N = 10^4, $\Omega_{cf} = 5\gamma_e$ and $\Delta_e = \Delta_c = 30\gamma_e$. Hence, to create a single Rydberg excitation we require at least a power of $\sim$ 100 nW in locking beam. Since the lock of the relative phase is stable for a power of $\approx$ 50 pW, it limits the probability of Rydberg population to less than 10^{-3} in the cavity mode.

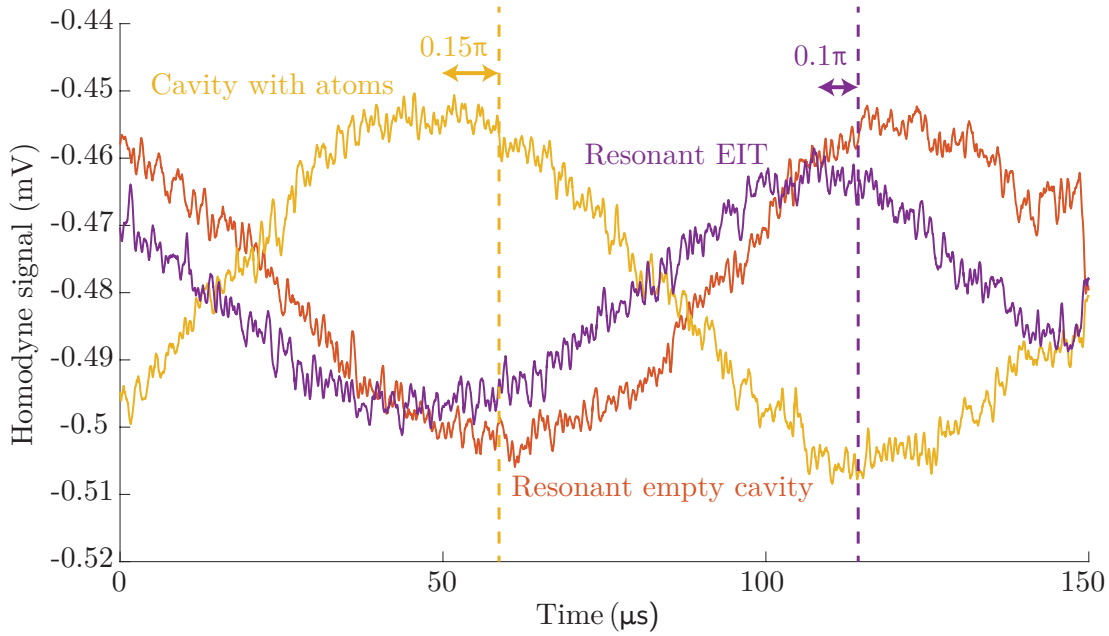

Figure 6.6: **Phase measurement using a resonant probe in reflection**. As relative phase between the LO and the locking beam is varied with time, we can observe that the phase is flipped by approximately 0.85 π when the atoms are switched on (green curve) compared to the empty cavity (red curve). When the coupling beam is switched on, the phase is flipped again by 0.9 π when the EIT peak appears (blue curve). The vertical lines are denoted to show the location of ideal phase flip of π. The dashed lines are denoted to visualize the deviation from ideal phase shifts.

Phase measurements with cavity EIT

We know that when the cavity is empty and locked on resonance with the probe, the reflected light has the same phase as the incoming light. In the presence of atoms, the resonant probe is scattered and the light reflected from the bottom mirror acquires a phase of π. As we can observe in Figure 6.6, the cavity with atoms has almost the same amplitude (95 % corresponding to the bottom mirror reflectivity)

but acquired a phase shift of 0.85π. In the presence of EIT in the linear regime, the resonant probe can enter the cavity again and the phase is flipped by π but the reflected intensity is weaker as the EIT transmission is not 100 %. We observe a phase shift of 0.9π compared to the situation with atoms. These measurements suggest that this setup is suitable to measure phase flips of the probe field and can be used to measure the fidelity of the Controlled phase gate.

6.2.2 Squeezing measurements in transmission

We setup a homodyne detection method which allows us to study the spectral components of the light retrieved from the cavity. We can extract the squeezing spectrum from the homodyne signal by spectral filtering. The noise power spectrum of the photo current is given by [51]

$$S(\omega,\theta) = \int_{-\infty}^{\infty} dt e^{-i\omega t} \left\langle : X_\theta^{OUT}(t), X_\theta^{OUT}(0) : \right\rangle, \tag{6.7}$$

where : indicates normal ordering and $X_\theta^{OUT}(t) = a_{OUT}(t)e^{-i\theta} + a_{OUT}(t)^\dagger e^{i\theta}$. According to convention, the orthogonal quadratures are represented by x = $X_{\theta=0}$ and p = $X_{\theta=\pi/2}$.

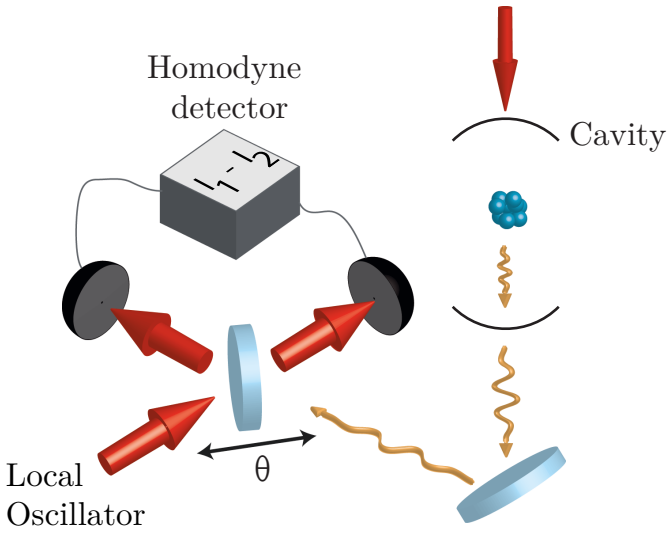

Figure 6.7: **Squeezing spectrum in transmission**: The probe phase is transmitted through the cavity and its relative phase is measured by changing its value by $\pi/2$. The measurements are repeated several times to acquire enough statistics for each value of the phase.

Experimentally one has to fix the phase or know the phase for measuring the squeezing spectrum using the homodyne measurements. In the previously described method the locking beam and the probe beam are in the same mode, which allows us to lock the relative phase between the LO and the signal beam. However, we cannot use the same system for measuring the squeezing spectrum of the light transmitted through the cavity. For this set of experiments, we implemented a simpler scheme to measure the noise squeezing without having to actively control the relative phase

between the LO and the signal beam. We assume that the arbitrary phase difference between the LO and the signal beam doesn't fluctuate during the relatively small measurement time of 120 μs (compared to the coherence time of the laser).

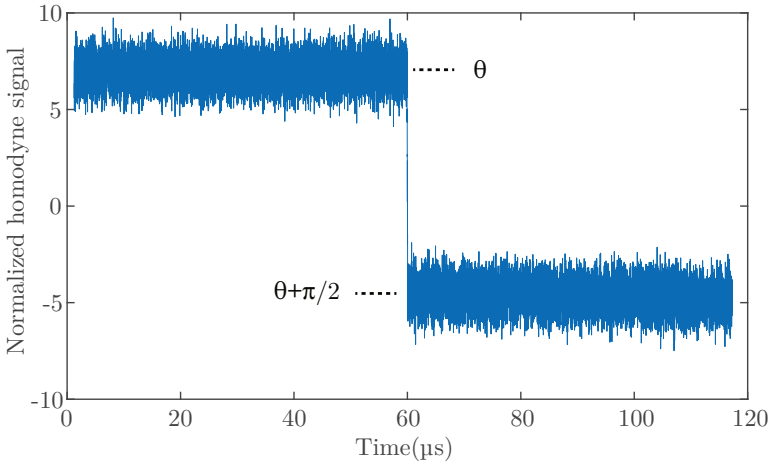

Figure 6.8: **Phase measurements:** Normalized homodyne signal within a cycle as a function of time. We flip the phase by $\pi/2$ at 60 μs. By using the value of homodyne signal from both halves we can determine the phase θ.

The active frequency generators (Synth300) can be used to change the phase of the radio frequency to any desired value. As the phase difference between the light and the LO is arbitrary we flip its phase by $\pi/2$ after half time. From the homodyne signal we can easily retrieve the initial phase θ (as shown in Figure 6.8). We repeat the experiment $\sim$1000 times to acquire enough statistics for each phase. By using a spectrum analyzer we acquire the squeezing in frequency space for each phase.

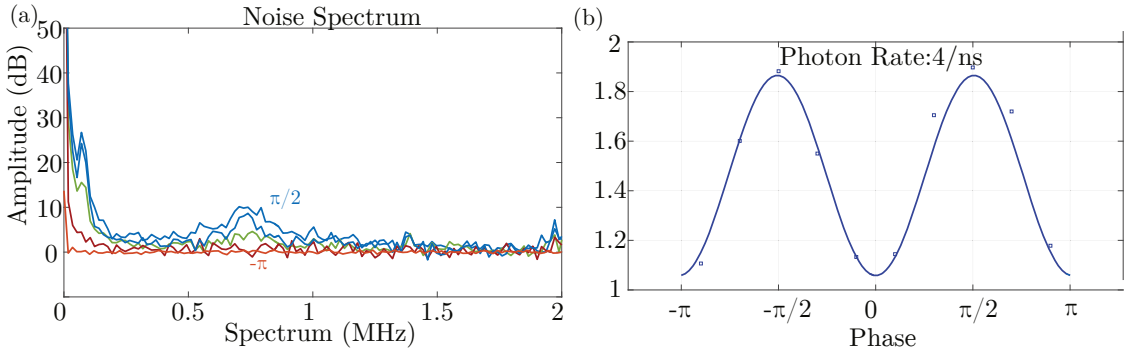

Figure 6.9: **Phase dependent noise from laser:** (a) The spectrum of homodyne signal for different phase differences between LO and the signal. At 700 kHz, we observe a strong phase dependent noise from the laser. (b) Average noise spectrum of the laser around 700 kHz plotted as a function of the phase.

Phase noise from the laser

To determine the phase noise of the laser, we measure directly the homodyne spectrum of the light coming from the laser without any dynamic elements like the cavity or atoms. As we can observe from the measurement signal in Figure 6.9, there is a strong phase dependent noise from the laser at 700 kHz. The phase noise

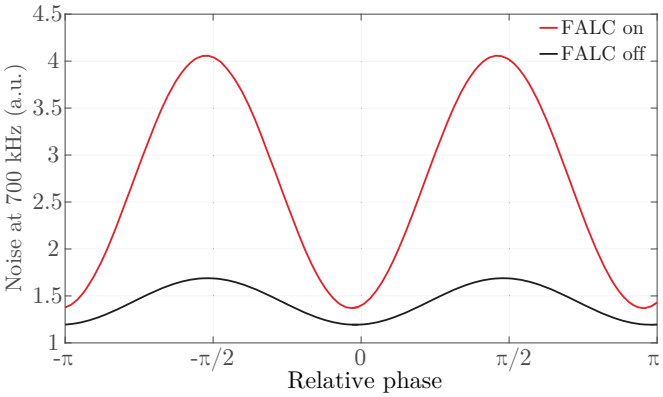

Figure 6.10: **Phase noise from the laser lock**: The phase noise at 700 kHz has been measured for the same probe intensity by switching on/off the laser lock. A FALC box is used to lock the laser on the transfer cavity, amplifies the phase noise.

is intensity dependent and can be described very well by assuming that the variance of one of the orthogonal quadrature varies linearly with intensity along with frequency dependence. We describe the variance of a coherent beam 'α' along the anti-squeezed quadrature by

$$\Delta Y(\omega) = 1 + k\alpha^2 e^{-\frac{(\omega-\omega_0)^2}{\sigma^2}} \tag{6.8}$$

where k, σ are constants, and depend on the laser lock parameters. We assume the variance along the orthogonal quadrature to be '1'. By using this model, the squeezing spectrum is estimated and plotted in Figure 6.11.

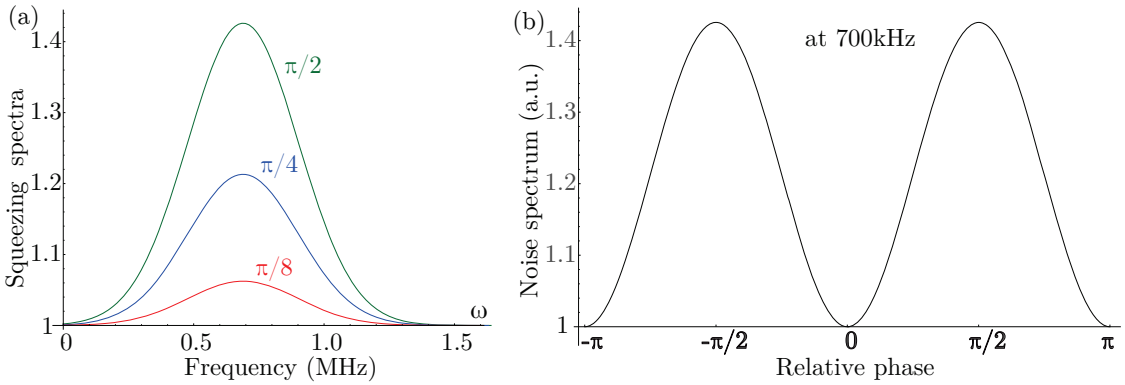

Figure 6.11: **Intensity dependent phase noise from model**: (a) The squeezing noise as a function of frequency for various phases. (b) The noise spectrum at 700 kHz as a function of phase.

The model allows us to predict how the noise varies with intensity so that we can proceed with the measurement of the transmission spectrum of the cavity.

Phase noise through the cavity

If we consider that the cavity is locked on resonance with the probe and the field is coupled to the cavity from the top mirror. We can look at the transmission spectrum of the cavity in the absence of atoms. In a resonant situation, the cavity transmitted intensity is about 1000 times smaller than what is incident at the top. If we compare the noise through the cavity to the direct noise from the laser, naively one might assume that the phase noise should be filtered by the cavity. But the noise is intensity dependent and, even though the cavity filters most of the phase noise, it is much higher than what we measured directly from the laser for the same intensity of the cavity transmission.

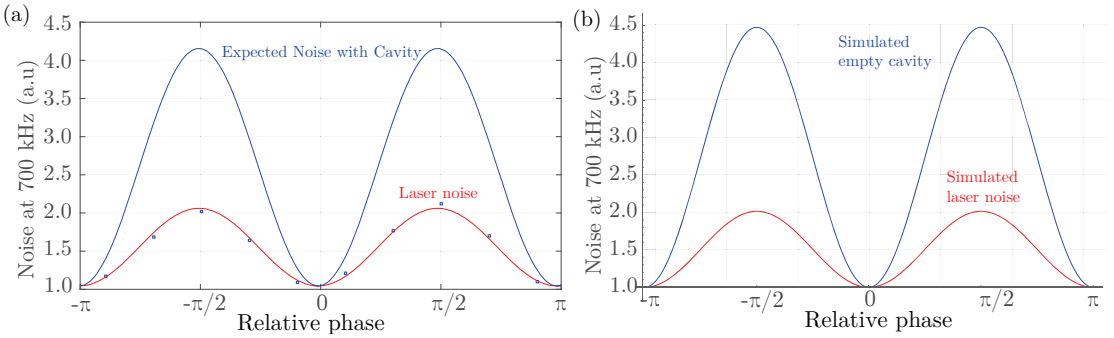

Figure 6.12: **Comparison of phase noise with and without cavity**: (a) **Experiment**: As the phase noise is intensity dependent we compare noise for the same intensity of light transmitted through the cavity and without the cavity. The red curve denotes the laser noise at 700 kHz and the blue curve denotes the noise we expect for the same light intensity through the cavity. (b) **Model**: We assume an intensity dependent noise in one of the quadratures and evaluate the spectrum in both the cases. The model reproduces the experimental observation accurately.

Unfortunately, the phase noise lies in the range of frequency (0-1 MHz) we are interested in. Nevertheless, the squeezing measurements allow us to probe the second order correlation effects of the transmitted light (refer to Chapter 8).

6.3 Conclusion

We demonstrated experimental methods to measure the $g^{(2)}$ function and squeezing spectra of the transmitted light. In addition, we also described the phase locked homodyne detection to detect phase flips on the experiment. We showed that the phase flips originating from the intracavity losses can be measured using this setup. We also characterized the noise originating from the probe laser using the squeezing spectrum and described the observations with an intensity dependent phase noise model. In conclusion, these methods in principle allow us to probe higher order non-linear effects originating from Rydberg-Rydberg interactions.

Part III

Absorptive Rydberg Non-linearities

Introduction

A decade ago, single photon non-linearities had never been observed experimentally in the optical domain. Since the proposal of using Rydberg-Rydberg interactions as a means of observing quantum optical non-linearities many groups have investigated various schemes where the photons are mapped onto atomic excitations using the EIT mechanism. The first experiment using resonant scheme in cold atoms was performed by Charles Adam's group [94]. In free space, many resonant EIT experiments have been designed to act as single photon filters [37], controlling optical photons using microwave Rydberg excitations [95].

In this part, we will discuss the experimental observation of the optical non-linear response of a cloud of cold atoms trapped inside a cavity. We will first describe the expected non-classical correlations and squeezing using perturbative approaches in weak feeding regime. In chapter 7 and 8 we will present our experimental results with a cavity of finesse 100. In chapter 9 we will describe our recent efforts to move towards the observation of quantum effects.

The important factor determining the non-linearity is the number of atoms which are influenced by a single Rydberg excitation. The sphere of influence is commonly referred to as the Rydberg bubble and the number of atoms blockaded are denoted by n_b. During the last few years, there were several new experiments which started employing Rydberg ensembles for strong optical non-linearities. The proposed idea is to slow down light using EIT conditions and then to further enhance the non-linearity using Rydberg-Rydberg interactions. This helps us to study many body interaction effects as well as the optical non-linearity at the few photon level.

To strongly increase the Rydberg effect, one needs to probe the system in a regime where even a single Rydberg excitation can change the cloud's optical response which can enable us to perform logical gate operations.

Dispersive non-linearities

As absorptive non-linearities in free space cause an irreversible loss of photons, one of the first experiments performed on this setup was to observe dispersive non-linearities. In free space, the effects are weaker which makes them harder to detect. Using an optical cavity one can amplify these effects into resonance shifts. In this section we will give a brief overview of dispersive non-linear measurements in classical regime carried out in our group during 2011-12. The experimental results and theoretical models were published in [48] and [96] respectively.

As we have seen in section 3, the Van der Waals interaction between Rydberg atoms shifts the resonance of nearby atoms and modifies its optical susceptibility. To avoid any resonance absorption the atoms are excited off-resonantly to a Rydberg state. The goal of the experiment is to observe nonlinear dispersion by Rydberg excitations using the scheme illustrated in Figure 6.13.

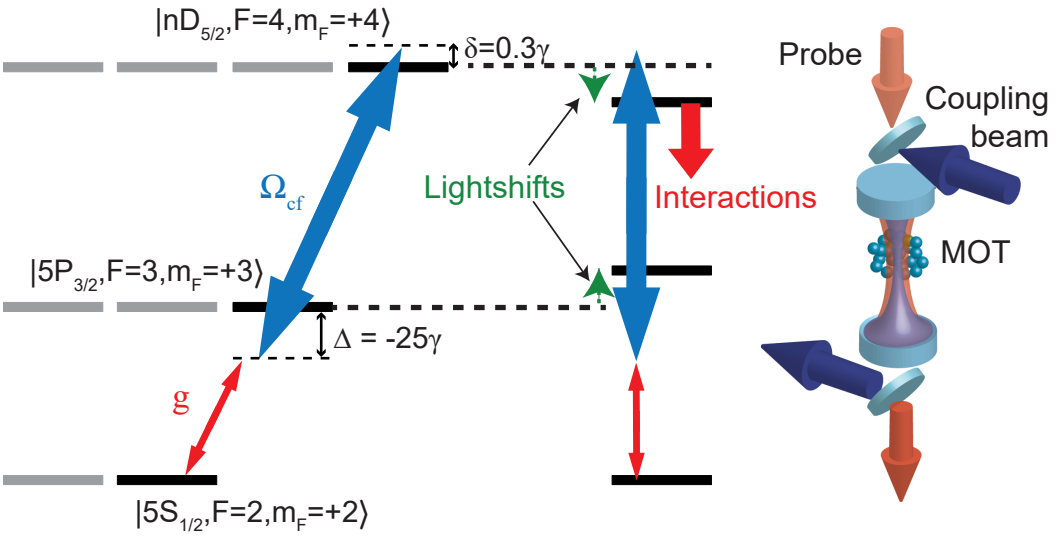

Figure 6.13: **Dispersive non-linearities using Rydberg excitations**: The atoms are excited using two photon excitation scheme where the probe light is red, and the coupling beam is blue detuned. This allows for the light shifts to move further from resonance and due to Rydberg-Rydberg interactions, the D states moves away from two photon resonance. The probe light and the coupling light are coupled to their fundamental modes from the top of the cavity using a dichroic mirror.

In order to measure the non-linear response, the cavity's length is scanned to probe the resonance position for various probe field intensities. Due to the Rydberg blockade effect, the optical susceptibility moves closer to the two level system for higher probe powers. The Rydberg induced shift of cavity resonance was measured as a function of the normalized probe intensity (Y), for different Rydberg levels.

A more precise criteria, to determine if the system can be used for phase gate like operation is to measure the non-linear resonance shift equivalent to the cavity linewidth. For n=62 $D_{5/2}$, the steady state photon number inside the cavity needed for shift of transmission peak by γ_c is 30. One cannot take only photonic excitations in the system as a benchmark, as there are many atoms ($\sim$5000) excited to the Rydberg state in the steady state. Nevertheless, the non-linearity is much stronger compared to the two level system where all the atoms(10^4) must be saturated to observe the expected behavior. The susceptibility was amplified in the presence of cavity of finesse $\sim$ 100. The expected $\chi^{(3)}$ value for the system is 4.10^{-9} $m^2.V^{-2}$. It is only two orders of magnitude lower than the resonant non-linearities observed in free space [35], and the largest observed dispersive susceptibility at the time of measurement.

A large non-linear dispersion should pave the way for optical bi-stability over a certain intensity, but the lack of such observation can be explained by the Rydberg

population dynamics. The absence of experimental bi-stability is attributed to the system evolution at the same scale as the typical measurement time [78]. In addition, there are inhomogeneous effects due to non-uniform control beam caused by a standing wave formed in the cavity.

Resonant Rydberg EIT

To increase the effect of a single Rydberg excitation, one possibility is to move closer to resonance. This will increase the spontaneous emission from the intermediate state due to Rydberg blockade mechanism leading to optical losses. The idea is to use different cavity mechanisms to minimize the losses while increasing the Rydberg interaction effects. Another possibility would be to increase the finesse of the cavity, which amplifies the weak interaction effects enough to significantly modify the optical response.

The main requirements for the realization of a controlled phase gate is to be able to modify the phase of a single photon using another. Our objective is to induce this phase shift by using a single Rydberg excitation. This led us to explore schemes closer to resonance, as a cavity can convert resonant Rydberg induced optical losses into phase shift. In order to find the relevant parameters of the system, which can help us achieve this quantum regime, we probe the system's resonant optical non-linearities.

Moreover resonant non-linearities are analytically intractable, hence many phenomenological models have been developed to describe the resonant interactions in free space [97] as well as in cavity [46, 47]. We described two such models in the chapter: 3 to describe the non-linear effects on our experiment.

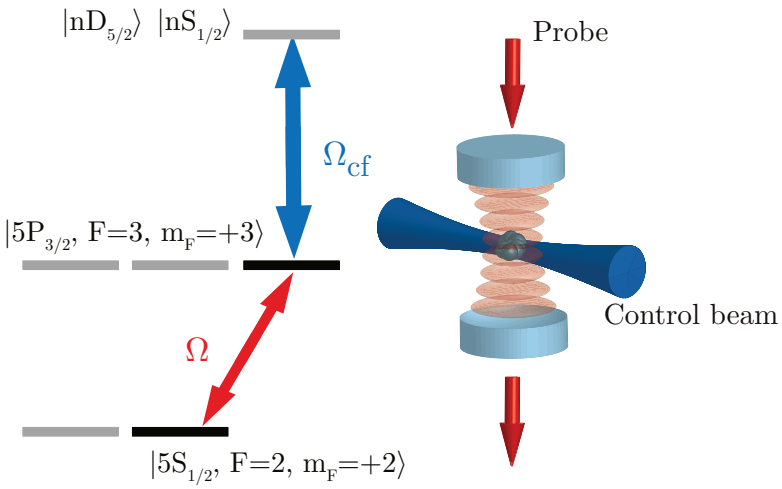

Figure 6.14: **Resonant excitation scheme with experiment**: The probe and the coupling beams are incident on resonance with atoms. The polarization of the control beam is fixed by the eigen modes of the blue cavity and it allows us to couple to all magnetic sublevels of D,S states.

In this part, we will describe the main cavity system which allows us to define the interacting mode between the probe and atoms. We will present a blue cavity

system which helps us to create large uniform Rabi-frequency to excite to high-lying Rydberg states. We will also report the resonant optical non-linearity created by Rydberg-Rydberg interactions and characterize the system. In addition, we will present some numerical models which enable us to evaluate higher order non-linear effects and determine the interesting range of parameters necessary to observe quantum non-linear effects. Finally, we conclude this part with the correlation and the squeezing measurements using Rydberg S states.

Chapter 7

Measurement of Absorptive Optical Non-linearities

Contents

7.1 Main cavity 72
7.2 Preparation of a small cloud 77
7.2.1 Dipole traps 77
7.2.2 Loading the traps 78
7.3 Cooperativity measurement 80
7.4 EIT in a cavity 82
7.4.1 Blue cavity 82
7.4.2 Linear regime 86
7.4.3 Rydberg linewidth 87
7.5 Non-linearity measurements 88
7.5.1 Resonant nonlinearity with Rydberg S state 88
7.5.2 Resonant non-linearity using Rydberg D states 90
7.5.3 Dephasing in Rydberg D-States 92
7.5.4 $\chi^{(3)}$ determination 95
7.6 Conclusion 95

The main experimental requirement to observe a strong non-linear effect is a small dense cloud whose size is comparable to the size of a typical Rydberg blockade radius. An advantage of having a small cloud is that it allows us to focus our blue coupling beam to waist size comparable to the cloud size, which in turn gives us the ability to access high lying Rydberg states. In this chapter we will describe how we prepare our atomic cloud and demonstrate classical non-linearity measurements with Rydberg S and D states.

In the current experimental setup, the atoms are excited resonantly, hence the Rydberg-Rydberg interactions leads to optical losses in transmission. The objective of this experiment is to measure the scaling of non-linearity for different Rydberg levels.

7.1 Main cavity

A cavity plays a crucial role in defining the optical mode, which interacts with the atoms. It enhances the coupling strength between the atoms and the light, which is defined by the mode volume and the cavity finesse. However it brings in more constraints such as restriction of frequencies which can be used to excite the atoms, and complexity. The cavity systems require precise positioning with respect to atoms and length stabilization. We will show how we resolve the technical issues by using a system which is designed with external control while still staying under vacuum.

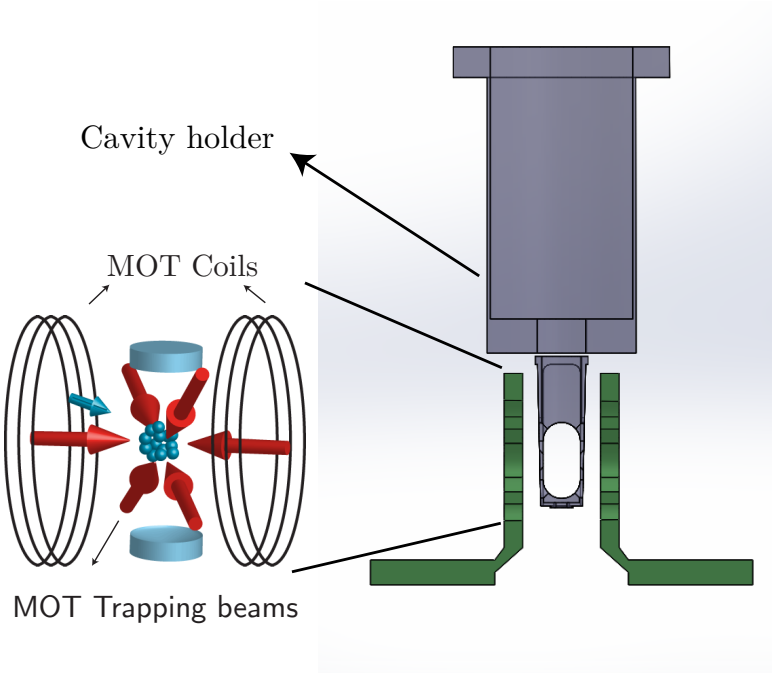

Figure 7.1: **Main cavity setup**: A schematic drawing of the MOT coils along with the position of the cavity holder in the system.

Parameter	Value
Length	6.6 cm
FSR	2.3 GHz
Linewidth	$\sim 2\pi$ 11 MHz
Mode waist	86 μm
Finesse	120
MOT distance from top mirror	2.2 cm

Table 7.1: **Main cavity parameters**

The cavity is positioned vertically parallel to both the MOT coils and its length is set to 6.6 cm which allows us to excite Rb^{87} atoms from both the hyperfine levels of the ground state $5\,S_{1/2}$ (which are separated by 6.8 GHz). To have maximum overlap

between two different standing wave patterns, the MOT is positioned 2.2 cm away from the top mirror. The top and the bottom mirrors have reflectivity coefficients of $R_1 > 0.999 \pm 0.1$ and $R_2 \approx 0.95$ at 780 nm. The cavity decay rate, i.e. Half Width at Half Maximum (HWHM) in the case of $T_2 \gg T_1$, can be obtained by $\gamma_c = \frac{c}{4L} T_2 = 2\pi\ 10 \pm 1\, MHz$. We can obtain the linewidth experimentally by measuring the transmission of the cavity by scanning the detuning of the probe light around the cavity resonance. The measured linewidth is $\approx 2\pi\ 11\, MHz$ which correspond to a $R_2 = 0.94$. From on-resonance transmission measurement we find the value of T_1 is $\approx 10^{-5}$.

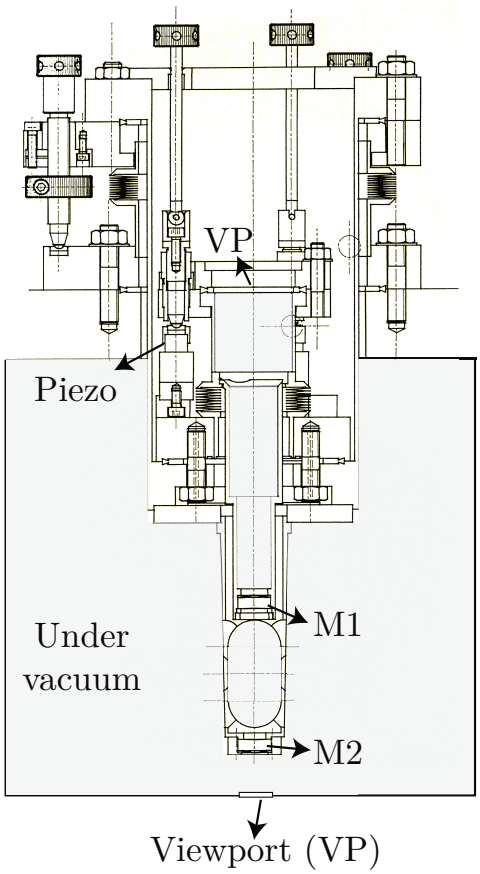

Figure 7.2: **Technical drawing of the cavity holder**: The location of the top (M1) and the bottom mirrors (M2) are illustrated. The greyed out part is under vacuum. The top mirror and the top viewport are made of a single piece, which is connected via a bellow to the main chamber. The viewport piece can be moved with the help of three screws resting on three different piezos. This allows us to change the cavity length and mirror alignment from the outside. The whole cavity can also be moved with the help of three more external screws.

Both the cavity mirrors have a curvature radius of 6 cm giving a cavity mode waist of 86 μm for a cavity length of 6.6 cm at 780 nm. The cavity is mounted on a specially designed system that allows us to change its length from outside the vacuum chamber. To achieve this one of the cavity mirrors and the top view port are attached to the vacuum chamber using a flexible bellow. The top mirror orientation and the distance from the bottom one can be adjusted by three inner

screws (BM17.04N with a range of 4 mm) resting on three different piezos. The piezos (PI P-170) have a travel range of 4 μm and are controlled by a E-501 voltage amplifier (from PI instruments) with a range 0-1000 V. The cavity's orientation can also be adjusted with three outer screws.

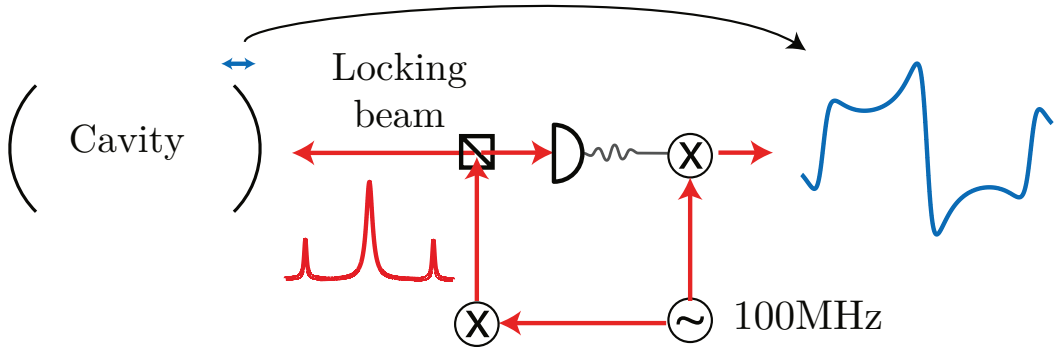

Figure 7.3: **Cavity locking loop using PDH technique**: We use an EOM to create two side bands on the locking beam at 100 MHz. The error signal is extracted by demodulating the reflected signal from the cavity. The length is stabilized by acting on the piezo using the slope of the error signal.

Stabilizing the cavity

Unlike most high finesse experiments, our mirrors are not glued to a low expansion surface. They must be actively stabilized against acoustic and thermal noise. In order to stabilize the distance between two mirrors, we use an auxiliary beam far from any atomic transitions at 810 nm. To minimize any light shift effects on the atoms, we only use about 100 μW of power while performing measurements.

We implement the Pound-Drever Hall (PDH) technique to lock the cavity's length [98]. The locking beam is phase modulated at 100 MHz using an Electro-Optic Modulator which creates two side bands. When incident on the cavity on resonance with the carrier frequency, the side bands acquire opposite phases on reflection. This allows us to extract an error signal like the one shown in Figure 7.3. We use a proportional-integral-derivative (PID) controller box to stay on resonance by acting on all the three piezos controlling the top mirror position. The frequency of the 810 nm laser is tuned to make the atomic transition ($5\,S_{1/2} \rightarrow 5\,P_{3/2}$) resonant with the cavity.

The cavity stability depends on the bandwidth of the whole locking loop. As the piezos are not acting just on the mirror, but also on the whole cavity holder setup, it cannot act on frequencies higher than 50 Hz. Any small noise at piezos' resonant frequency of 1 kHz can kick the cavity out of lock. After spending a significant amount of time, we managed to achieve a cavity stability $\sigma \approx 2$ MHz (refer to Figure 7.4).

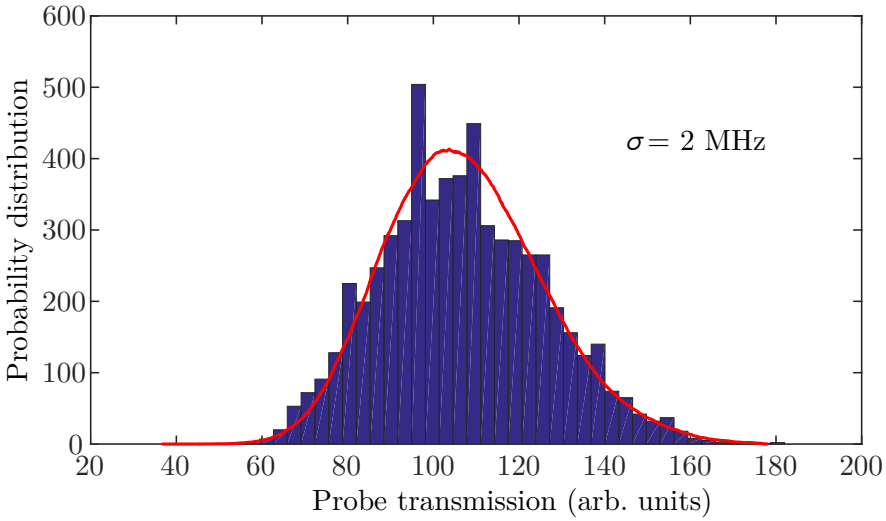

Figure 7.4: **Cavity lock stability**: We measure the transmission of the probe when it is detuned by the cavity linewidth from resonance (i.e $\Delta_e = \gamma_c$) to probe the stability of the cavity. The probability distribution of the normalized transmission was shown along with a model (red curve) where the cavity's resonance frequency has a standard deviation of 2 MHz.

Parameter	Value
Auxilary beam wavelength	810 nm
Locking beam power	≈100 μW
Modulation frequency	100 MHz
Cavity frequency stability	≈ 2 MHz

Table 7.2: **Main cavity lock parameters**

Calibration of photon flux

In this part we will describe how to evaluate the number of photons in the cavity when it is excited with a continuous optical field. The number of photons inside the resonator depends on many different parameters like the cavity resonance, the losses, etc. To convert the detected photon rate into number of photons present in the system, we use input/output relations of a two sided cavity.

In general, if we consider a cavity with decay rates $\gamma_1 = \frac{c}{2L}T_1$ and $\gamma_2 = \frac{c}{2L}T_2$ for the top and the bottom mirrors and the cavity is locked on resonance then in steady state

$$\begin{aligned} a_{out} + a_{in} &= \sqrt{\gamma_1}a \\ b_{out} + b_{in} &= \sqrt{\gamma_2}a \end{aligned} \tag{7.1}$$

where a and b refer to the fields on the top and bottom side of the cavity respectively as illustrated in Figure 7.5. The above equations are valid even in the presence of losses inside the cavity.

If we assume that the resonant light is coupled only from one side of the cavity (top mirror), then one can calculate the reflected, intracavity and transmitted fields

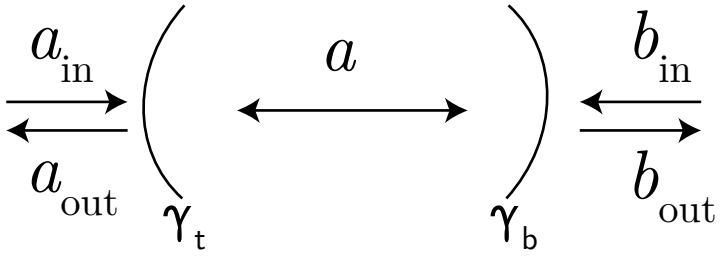

Figure 7.5: **Cavity with incident and reflected fields**: A cavity which is excited using fields a_{in} and b_{in}. The intra-cavity field is denoted by a. The decay rates of the top and the bottom mirrors are indicated by γ_t and γ_b respectively.

from the following equations:

$$\begin{aligned} a_{out} &= \frac{\gamma_1 - \gamma_2}{\gamma_1 + \gamma_2} a_{in} \\ a &= 2\frac{\sqrt{\gamma_1}}{\gamma_2 + \gamma_2} a_{in} \\ b_{out} &= \sqrt{\gamma_1} a = 2\frac{\sqrt{\gamma_1 \gamma_2}}{\gamma_1 + \gamma_2} a_{in} \end{aligned} \tag{7.2}$$

As the decay rate of the bottom side mirror is much higher than the top one then HWHM of cavity $\gamma_c = \frac{\gamma_1+\gamma_2}{2} \approx \frac{\gamma_2}{2}$. If we feed the cavity with a coherent state α then under steady state condition the intracavity field is given by $a = \frac{-i\alpha}{\gamma_c}$. Hence the average photon number inside the cavity is given by α^2/γ_c^2, and the output flux of the cavity is given by $2\alpha^2/\gamma_c$.

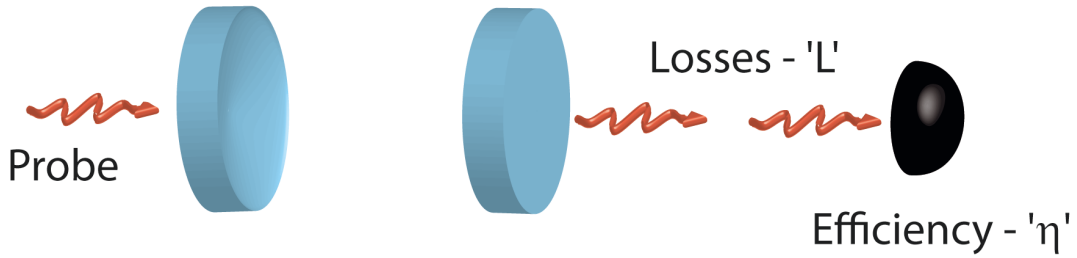

Figure 7.6: **Experimental Setup**: The probe light is coupled from the top side of the cavity and we measure the cavity transmission using two single photon counting modules. This setup was designed for the $g^{(2)}$ measurement but we also use if for photon counting experiments. To avoid detection of any stray light especially from the auxilary cavity locking beam, we use different filters at 780 nm.

Experimental calibration

To calibrate the photon flux, we measure the output of the cavity in the absence of atoms and the probe is incident on resonance with the cavity. We measure the photon count on the SPCMs.

The efficiency of the detector is 67% at 780 nm. The optical losses from the output of the cavity until the detectors (including the coupling efficiency) is 50% for both the detectors. If we detect N photons in t μs, then the photon flux at the output of the cavity is given by

$$\text{Flux} = \frac{N}{t \times 0.335} = \frac{2\alpha^2}{\gamma_c} \tag{7.3}$$

In a typical experimental scenario we have n photons detected on each SPCM in 120 μs, then

$$\frac{2\alpha^2}{\gamma_c} = 2.5 \times 10^{-3} n\gamma_e$$
$$\alpha = 0.07\sqrt{n}\gamma_e$$

where we use the value of intermediate state linewidth $\gamma_e = 2\pi\, 3$ MHz and cavity's HWHM $\gamma_c = 2\pi\, 10$ MHz. The average number of photons inside the cavity for a typical detected photon rate of 40 per cycle corresponds to only 0.015 in steady state.

7.2 Preparation of a small cloud

In order to generate a cloud of few tens of microns in size, a very usual employed method is to load the atoms from the MOT into a crossed dipole trap. In the following section, we will describe the loading and preparation of a small dense atomic cloud.

7.2.1 Dipole traps

Atoms can be trapped by using radiative forces from an optical beam [99]. This can be achieved by using lasers far from any atomic resonance. In practice, it is easier to work with red-detuned gaussian beams, in which the atoms are pushed towards its center. But any dipole trap with large Rayleigh range can only confine the atoms in directions orthogonal to the beam propagation. Hence, To achieve a three dimensional confinement we use more than one dipole trap.

On our experiment, we use a red detuned beam from D1 and D2 transitions at 810 nm from Ti-Sa lasers to create dipole traps; one along the cavity axis and two orthogonal to it. The dipole trap along the cavity is created from the same beam that is used to lock the cavity's length. To avoid any inhomogeneous light shifts while exciting the atoms to EIT, we switch between two states: 'only cavity lock' and 'cavity lock + dipole trap'. In practice, we use a RF controller to switch the AOM to create a high optical output and simultaneously decreasing the modulation signal which creates side bands for cavity lock. This would allow us to switch while maintaining the same magnitude of the cavity lock's error signal. In 'only cavity lock' state we use only 100 μW to minimize any light shifts and in 'cavity lock+dipole trap' position we use about 10 mW. This creates a standing wave trap inside the cavity with $\approx 85\,\mu$m waist. The vertical trap forms a standing wave

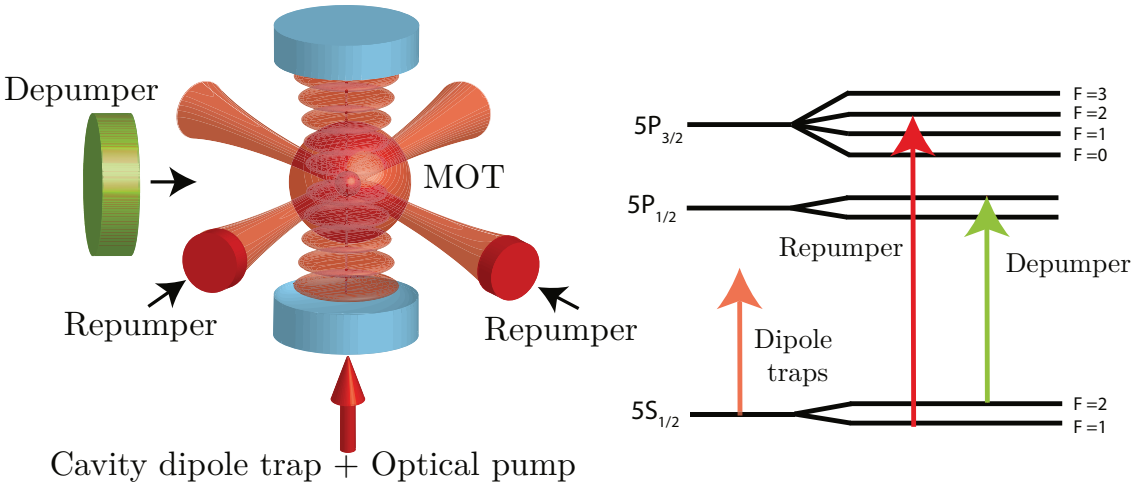

Figure 7.7: **Configuration for small cloud preparation**: **On left**: The atoms are loaded from the MOT to the crossed dipole trap during molasses. All the atoms in the system are depumped to a dark state ($5\,S_{1/2}$ F = 1) and only the atoms in the dipole traps are selectively repumped to the desired state ($5\,S_{1/2}$ F = 2 m_F = 2). **On right**: The energy levels of Rb^{87} along with the position of various excitation beams are represented (frequencies are not to scale)

inside the cavity with two nodes separated by 405 nm allowing us to trap the atoms along vertically at the same time.

We create two more traps (referred to as horizontal dipole traps) overlapped with the cavity dipole trap for better trapping efficiency. Unlike the cavity dipole traps, these are created by single pass beams. The second trap is created by collecting the light from the first one using a fiber. The two horizontal traps are prepared by magnifying the beam to $\approx 8\,mm$ before being focused to a waist of 40 μm by using 500 mm lenses. The first trap power is about 450 mW while the second one about 300 mW.

The dipole potential can be estimated using $U_{dip} = \frac{\hbar\Gamma_e^2}{8\Delta}\frac{I}{I_{sat}}$ [99]. The trap depth of the vertical and the first horizontal trap is about 300 μK while the second one is about 200 μK. The overall setup is illustrated in Figure 7.7

7.2.2 Loading the traps

To load the atoms from the MOT, we simply overlap the dipole traps with the atomic cloud starting from the molasses stage and lasting upto 20 ms. To quantify the efficiency of loading the dipole traps we measure the number of atoms loaded in the traps. We observed that to accumulate high atomic densities without being affected by multiple scattering of light we have to reduce the repumper power during the loading sequence. Loading the atoms while repumping causes radiative repulsive forces and photoassociative collisions and hence decreases its efficiency [100].

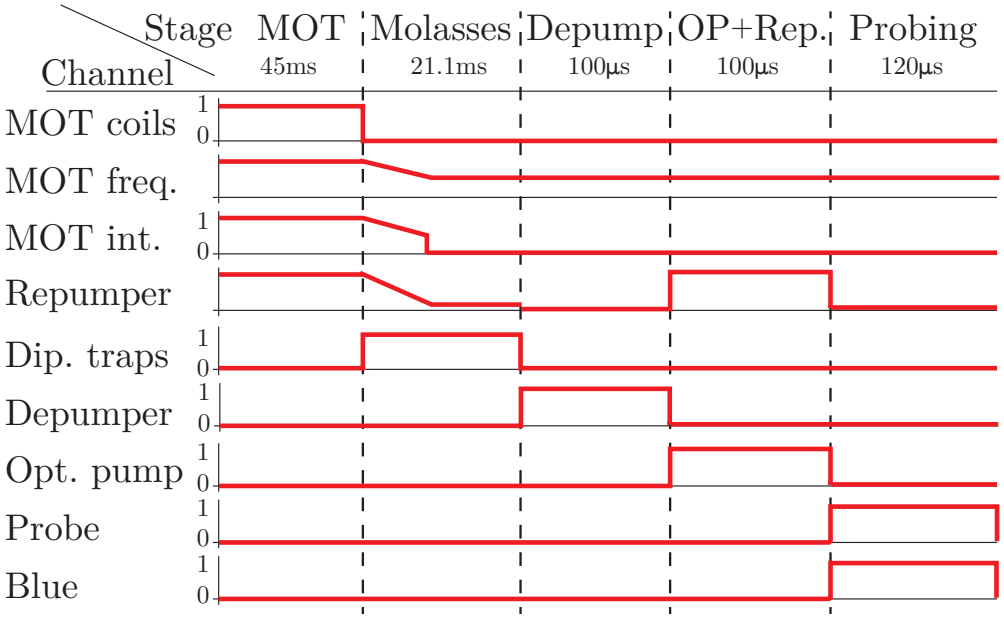

Figure 7.8: **Experimental Sequence**: After the cloud is trapped using the MOT for 45 ms, it is cooled down for 6.1 ms using polarization gradient cooling. During the molasses stage, the dipole traps are turned on and the atoms are allowed to load for about 21 ms. Then the whole cloud is depumped to $5\,S_{1/2}\,F = 1$ and only the atoms in the crossed dipole trap are repumped (and optically pumped) to $5\,S_{1/2}\,F = 2m_F = 2$. The atoms are probed during 120 μs during which the EIT transmission curves are measured.

Cloud preparation from dipole traps

As the cavity dipole trap has a Rayleigh range larger than 1 mm, the atoms a trapped in a cigar trap. In addition, the atoms outside the horizontal dipole traps require upto few 100 ms to escape but if one waits too long it will result in lower atomic densities. In order to only use the atoms which are in the crossed dipole traps we use a selective depump-repump scheme which allows us to achieve small clouds in reasonably short time.

We load the atoms from the MOT into crossed dipole traps by overlapping both the traps during 20 ms (upto 80 ms) of molasses stage. As the repumping power is set to low value, most of the atoms are already depumped to a dark state ($5\,S_{1/2}\,F = 1$) where the atoms are invisible to the probe transition ($5\,S_{1/2}\,F = 2 \rightarrow 5\,P_{1/2}\,F = 3$). We use an additional depumper pulse on the D1 transition to depump any left over atoms to the dark state. Then for 100 μs we shine a repumper pulse ($5\,S_{1/2}\,F = 1 \rightarrow 5\,S_{1/2}\,F = 3$) along the horizontal traps and a circularly polarized optical pumping pulse ($5\,S_{1/2}\,F = 1 \rightarrow 5\,P_{1/2}\,F = 1$) along the cavity dipole trap. This allows us to spatially isolate the atoms that are of interest and prepare a small dense cloud in the state $5\,S_{1/2}\,F = 2\,m_F = 2$. In addition, it improves the duty cycle of the experiment as we don't have to wait until all the atoms are lost.

The final loading sequence is shown in Figure 7.8. After loading the trap, we image the trapped atoms for 1 ms. From Figure 7.9, we can see that the atomic waist trapped in the cavity dipole trap is about 40 μm and in the side dipole trap

Stage	Settings	Time
MOT	trap -18 MHz	40 ms
Molasses+Dipole traps	-18 MHz to -48 MHz	6 ms
Dipole traps	810 nm	14 ms
Depumping	$F = 2 \rightarrow F' = 1$	100 μs
Optical pumping + Repumper	$F' = 1 \rightarrow F = 2$	100 μs
Probe+Blue	$F = 2 \rightarrow F = 3$	120 μs

Table 7.3: **Final sequence timings**

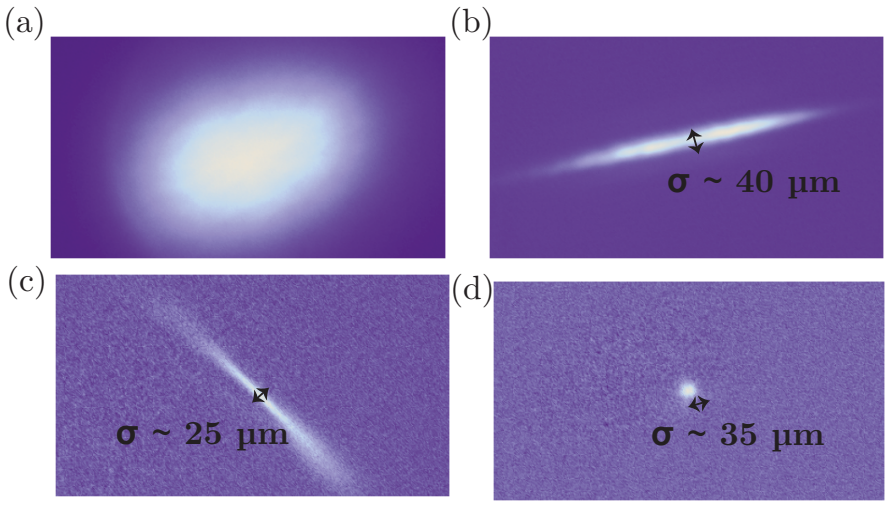

Figure 7.9: **Images of atomic clouds during different stages** (a)Image of complete MOT without dipole traps (b) Image of atoms trapped in cavity dipole trap (c) Image of atoms trapped in side dipole trap (d) Image of the final small cloud at the end of the preparation stage.

is 25 μm. The orientation of the cavity trap is not vertical as the imaging axis is not orthogonal to any of the traps. Finally, the size of the small cloud is 35 μm.

7.3 Cooperativity measurement

The trapped small cloud is characterized by its cooperativity. The cooperativity of the system can be probed by measuring the dispersive shift or resonant absorption. As the cooperativities obtained with our small cloud are less than 50, we cannot obtain a precise value using dispersive shift measurements.

We use a 780 nm optical beam close to the atomic transition ($5\,S_{1/2}$ F = 2 $\rightarrow$ $5\,P_{3/2}$ F' = 3) to probe the atoms. The cavity is locked on resonance with atoms while the probe frequency is scanned around the resonance of the atoms from -50 MHz to +50 MHz. The dipole traps are switched off during the measurement to avoid any light shifts. The cavity transmission for different probe intensities is monitored either with an Avalanche Photo Diode (APD) or SPCMs. The measurement are performed over 120 μs. When the cavity is empty we obtain the linewidth

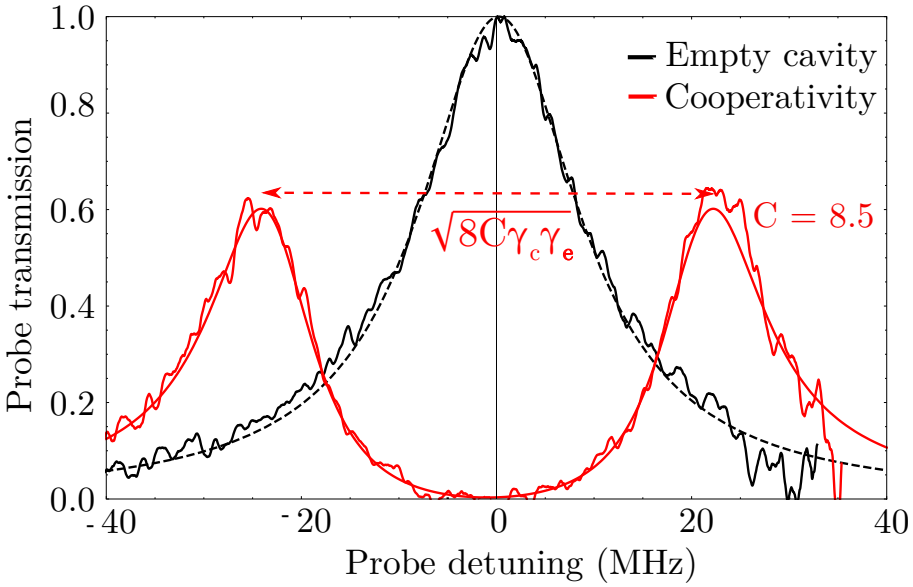

Figure 7.10: **Cooperativity measurement**: The black line denotes the empty cavity transmission and the red line is the cavity transmission in the presence of atoms. The cavity locked on resonance with atomic transition and the probe frequency is scanned across the resonance frequency. The atoms split the cavity mode into two normal modes separated by $\sqrt{8C\gamma_c\gamma_e}$. For this measurement, the cooperativity of the system is 8.5 and the HWHM (half width at half maximum) of the cavity is measured to be 11 MHz.

of the cavity and in the presence of atoms the normal modes are split into two. The splitting between the eigen energy states of the coupled system allows us to calculate the cooperativity. The frequency splitting of the eigen modes is calculated using $\sqrt{8C\gamma_c\gamma_e}$. The typical measured cooperativities are 8 - 10 which correspond to 10^4 atoms loaded in the trap.

Atomic inhomogeneities

It is important to account for various inhomogeneous effects which contribute to the deviation of experimental observations from the ideal behavior. Due to the selective preparation of the small atomic cloud it creates many atoms trapped in dark state (F = 1) in the cavity mode. In small numbers these atoms wouldn't affect the probe transmission but once we reach cooperativities of few hundreds for atoms in F = 1 we see a shift in the cavity's resonance. This shift leads to the observation of asymmetric normal modes even when the cavity is locked on resonance with the atoms. We measure the cavity transmission in the presence of depumped atoms and no atoms and the shift corresponds to a cooperativity of ≈250 for atoms in F=1.

Finally, the probe creates a standing wave inside the cavity which makes it impossible to have uniform coupling strength for all the atoms. The probability distribution of the intensity seen by the atoms is shown in Figure 7.11. We assume an average coupling parameter for all the atoms and the approximation is valid for short time scales when the atoms don't move.

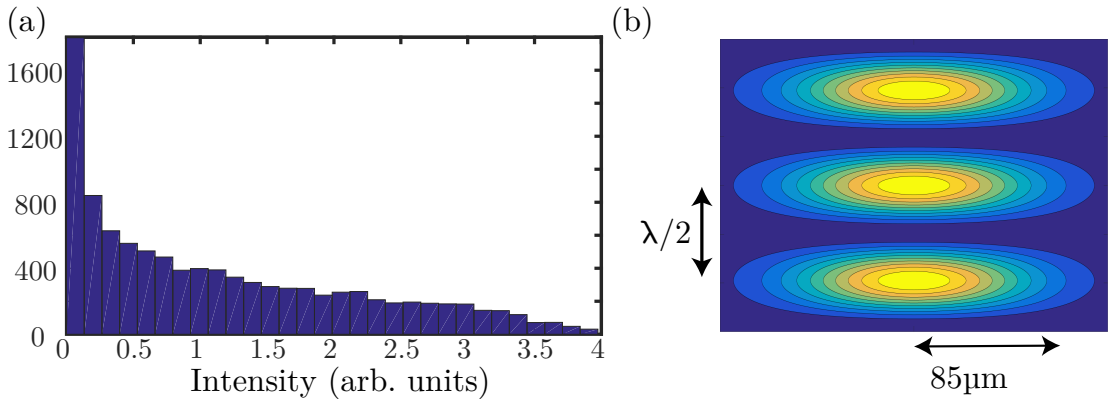

Figure 7.11: **Probe intensity as seen by atoms**: The atoms don't see a uniform probe light because of the standing wave formed in the cavity. (a) Probability distribution of the intensities seen by the atoms. A significant number of atoms see zero intensity. (b) Contour plot of standing wave formed by the probe light.

7.4 EIT in a cavity

The small cloud allows to have a strong uniform blue beam to couple to the Rydberg states. But the power we have is still not sufficient to reach high lying Rydberg states. Therefore, a blue cavity was designed to have a large optical powers while minimizing the effects of standing wave.

7.4.1 Blue cavity

The weak dipole moment of the coupling transition requires a large amount of coupling power on the Rydberg transition. In order to enhance the Rabi frequency of the blue laser we use a cavity to increase the effective power of the coupling beam on the atoms. The easiest way to design a cavity that wouldn't require breaking the vacuum is to build a cavity outside the chamber. In order to minimize the standing wave effect on atoms, a confocal cavity is chosen with minimum overlap of incident and reflected beams. We use viewports which are anti-reflection coated for blue frequencies to construct the blue cavity with a length of 1 m and curved mirrors of f = 500±5 mm radius. To match the losses of the viewport the input coupler of the cavity was chosen with a reflectivity of 2.9% and the other mirror has a reflectivity (≫99.9%) from Layertec.

Parameter	Value
Length	1 m
FSR	150 MHz
Mode waist	90 μm
Finesse	50
Power enhancement factor	14

Table 7.4: **Blue cavity paramters**

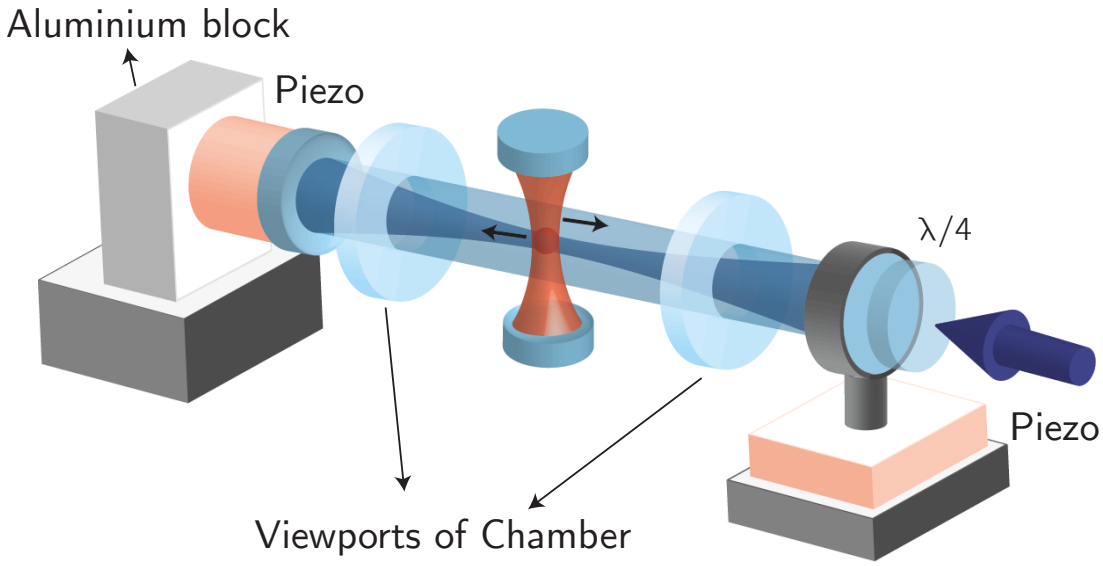

Figure 7.12: **A bird's eye view of the blue cavity along with the viewports of the vacuum chamber**: The cavity's position with respect to the main cavity and atoms is illustrated. Both cavity mirrors are mounted on two different piezos for stabilization.

By scanning the length of the cavity we measure the finesse of the cavity to be 90. The enhancement factor between the intra-cavity power and the incident beam is 14. This was measured from the scattering on one of the viewports. The waist of the blue beam can be set using the optics which couple the light to the cavity.

Stabilization of cavity length

Since the cavity is 1 m long and the mirrors rest on two independent breadboards situated 25 cm above the optical table, it has numerous sources of noise, making it a challenging task to stabilize its length.

We mount each mirror on two different kinds of piezos to cancel oscillations in different frequency range. One of the mirrors is mounted on a standard lens holder which is fixed to a translating piezo (P-611.10) with travel range of 120 μm. The other one is glued onto a cylindrical piezo (PICA P-025.10H, 15 μm range).

An auxiliary beam at 810 nm was used to stabilize the cavity length. The locking scheme was designed by taking advantage of the inherent birefringence created by the viewports present inside the cavity. We used a Hansch-Couillaud method to obtain an error signal to lock the cavity [101]. After optimization we couldn't attain a stable lock which was attributed to the stability of the breadboards.

The mirrors are placed on a 1.3 cm thick plain aluminum breadboards (Thorlabs MB4545) at a height of 25 cm, mounted on 4 legs of 1" diameter. We replaced them with 450 x 600 mm honeycomb breadboards (Thorlabs B4560A) with 6 cm thickness and mounted on legs of 1.5" diameter. However, this did not resolve the issue but helped to eliminate the mechanical noise. We observed that even though the optical path was stabilized for 810 nm, it wasn't for 480 nm. The reason was due to large

wavelength difference between the two beams which propagate in free space with no temperature and pressure control. The differential refractive index fluctuations led to slow drifts in the resonance at blue wavelengths. This explained why the cavity was stable for short time scales but inevitably went out of resonance with time. Finally, we chose an auxiliary beam closer to blue frequencies to lock the cavity's length.

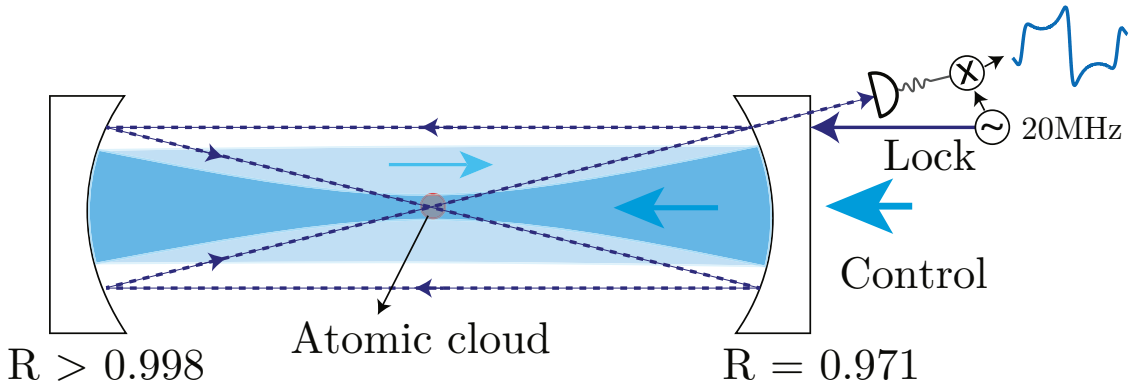

Figure 7.13: **Cross-section view of blue cavity along with optical beams**: Both the control and locking beams are incident into the cavity on the same side. The control beam is focussed and is collimated when reflected back from the highly reflective mirror. The locking beam is incident on the side and travels 4 times the length of the cavity. It is modulated at 20 MHz before incident onto the cavity and the reflected signal is demodulated to extract the error signal.

Currently, we use a 480 nm locking beam but far from resonance to lock the cavity's length. The beam is phase modulated and sent in a bow type configuration to minimize the overlap with control beam. The reflected signal is not in the same mode as the incident and hence, is easily extracted to generate a locking signal. Further instabilities led us to redesign the pieces which hold the mirrors for the blue. Finally, the mirror with cylindrical piezo is glued onto an aluminum block which is placed on a manual translation stage to adjust the length of the cavity but fixed firmly after the cavity is aligned to avoid mechanical vibrations. This helped us to minimize the noise at the resonant frequencies of the piezos.

Estimating the maximum locking beam power

As the locking beam is not very far detuned from the Rydberg transition, there is a finite probability of exciting to Rydberg states. If we start with the Bloch equations

(Equation 2.28) corresponding to terms $\sigma_{er}, \sigma_{ee}, \sigma_{rr}$

$$\frac{d\sigma_{er}}{dt} = i(D_r - D_e - \frac{\Omega_{cf}^2}{4D_r})\sigma_{er} + i\frac{\Omega_{cf}}{2}(\sigma_{rr} - \sigma_{ee}) + iga^\dagger\sigma_{gr}$$
$$\frac{d\sigma_{ee}}{dt} = -2\gamma_e\sigma_{ee} + 2\gamma_{rr}\sigma_{rr} - i\frac{\Omega_{cf}}{2}(\sigma_{er} - \sigma_{re}) + ig(a^\dagger\sigma_{ge} - a\sigma_{eg})$$
$$\frac{d\sigma_{rr}}{dt} = -2\gamma_{rr}\sigma_{rr} + i\frac{\Omega_{cf}f}{2}(\sigma_{er} - \sigma_{re})$$

where γ_{rr} is the population decay rate of the Rydberg state. The number of Rydberg excitation in the cavity can be evaluated from

$$N_{rr} = N\sigma_{rr} = N\frac{\tilde{g}\alpha}{(\tilde{D}_e D_c - 2\gamma_e\gamma_c C)} \tag{7.4}$$

where $\tilde{g} = \frac{\Omega_{cf}g}{2D_r}$ and $\alpha = \frac{2\gamma_c P_i}{\hbar\omega_p}$.

For our typical experimental conditions, i.e. C = 10, $\Delta_e = 0$, $\Delta_c = 50\gamma_e$ the locking beam Rabi frequency of $\Omega_{cf} = 0.1\gamma_e$ limits the probability of Rydberg population to less than 10^{-4} in the atomic cloud. By measuring the scattered power, we estimate that the intra-cavity power is stable within 10% of the maximum value.

Parameter	Value
FSR	75 MHz
Auxilary beam detuning	150 MHz
Locking beam power	$\approx 100\,\mu$W
Modulation frequency	20 MHz
Blue power stability	$\approx$ 10%

Table 7.5: **Blue locking specifications**

Blue cavity alignment and inhomogeneities

The cavity length was adjusted to confocal by using the separation between the transverse modes in the reflected light when the cavity's length is scanned. By carefully merging we can obtain a confocal cavity but a clean symmetric signal is obtained only when its length is exactly equal to 1 m.

In order to align the beam with the atoms, we shine on-resonant probe and look for the EIT signal in transmission by using only 3% of the transmitted light. Once the beam's position over the atoms is optimized, while having the reflection overlap with the incoming beam, its position is fixed and we only adjust the rear mirror to align the cavity with the incoming beam. This allows us to optimize the cavity mode on the atoms.

When coupling the blue beam to the atoms, its waist plays a crucial role in determining the quality of the EIT signal. A non-uniform blue results in asymmetric absorption across the cloud. At the same time we cannot use a very large blue beam waist compared to the atomic waist, as it will reduce the blue beam intensity. In addition due to interference between the counter propagating fields is not completely

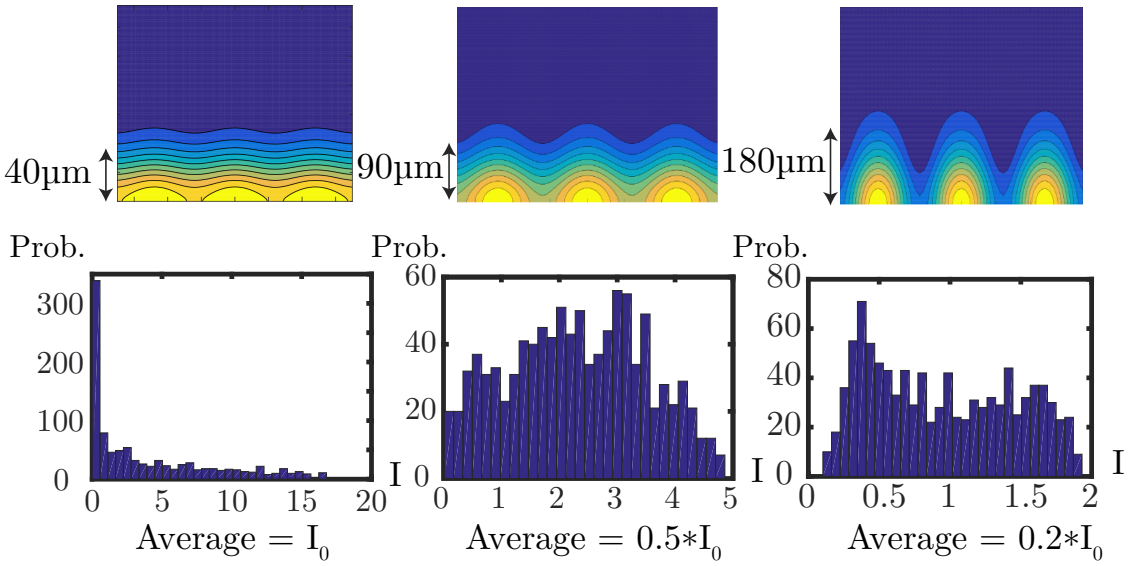

Figure 7.14: **Blue inhomogeneous effects**: **Top**: Contour plot of the blue intensity distribution at the waist of the cavity as a function of longitudinal and radial components for different values of waist. In the left most contour plot the standing wave effects are minimal but waist is comparable to atomic cloud size. In the right most contourplot the standing wave is prominent even though it is much bigger than the cloud size. **Bottom**: The probability distribution of the blue intensity as seen by the atoms. The units on the x- axis correspond to arbitrary units of blue intensity.

negligible. For a small waist ($\sim$ 40 μm), we can obtain more homogeneous high intense beam but most of the atoms see zero intensity, while for large beam waists ($\sim$ 180 μm) most atoms see non-zero blue intensities but the average intensity is low. To reach a compromise between the two extreme situations we choose 90 μm (refer Figure 7.14). Experimentally, in order to determine the suitable waist we optimize the EIT transmission by adjusting the waist size. We observe that the maximum EIT signal was observed for waist size twice the cloud size, i.e. 90 μm, where the average intensity observed by the atoms is still higher with not many atoms seeing zero intensity.

7.4.2 Linear regime

The probe is coupled to the fundamental mode of the cavity and the coupling light is sent orthogonal to the cavity mode as shown in Figure 7.12. As discussed in Section: 2.4, when we couple a coupling laser between the excited level to a long lived state, the medium can be rendered transparent. In this section we will describe the EIT measurements performed using our cavity.

To avoid, at first, any nonlinear effects arising from a Rydberg blockade, we couple the atoms to a level with a low principal quantum number using a control field resonant with the $5\,P_{3/2}$ F $= 3 \rightarrow 37\,D_{5/2}$ F $= 4$ transition. Since the Rydberg blockade effect is negligible, the response is identical for S and D states. In Figure

7.15, we show the cavity transmission as a function of the probe detuning. In the presence of the control field which couples the atoms to the 37 D Rydberg level, a transparency window is created at the two-photon resonance frequency. We note that such intracavity linear EIT was observed in many setups [102, 103] and more recently in a similar setup [104].

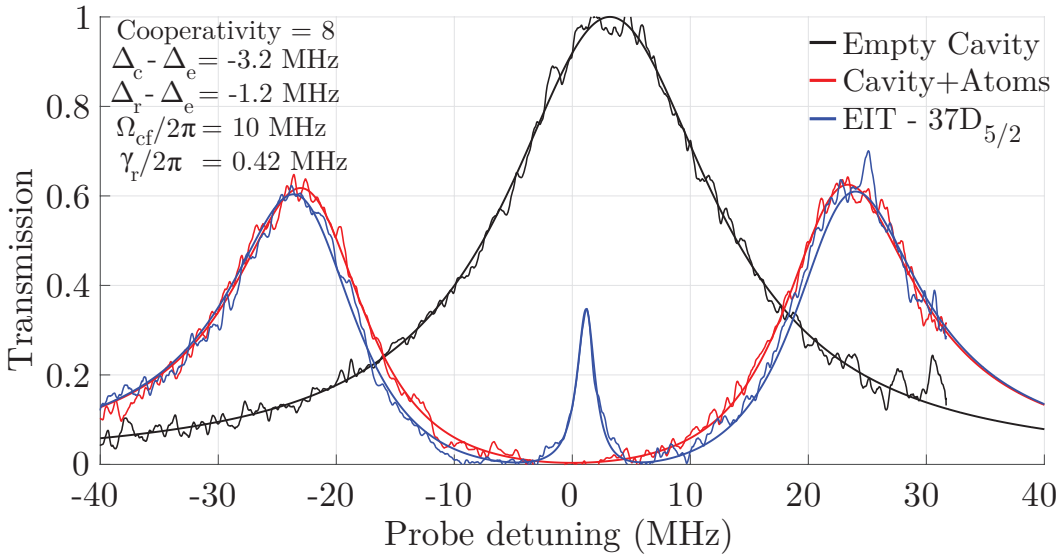

Figure 7.15: **EIT measurements in linear regime**: Cavity transmission as a function of the probe laser detuning for an empty cavity (black curve), with an intracavity atomic cloud (red curve) and with the presence of a control field resonant with the $5\,P_{3/2}\,F = 3 \rightarrow 37\,D_{5/2}\,F = 4$ transition (blue curve). A fit to the experimental observations allows us to extract various parameters of the system. We note that the centre of the two normal modes doesn't coincide exactly with the empty cavity resonance. This effect, taken into account in the fitting curves, is due to the presence of background atoms in a dark state ($5\,S_{1/2}\,F = 1$) which shifts the cavity line.

7.4.3 Rydberg linewidth

Due to weak dipole moments the natural Rydberg linewidths are extremely narrow but due to experimental noise the linewidth can be broadened. Several sources for these noise are oscillating weak electric fields, blackbody radiation, laser linewidth etc. Due to the presence of a weak static electric field in an unknown direction (created by stray charges) our quantization axis is not fixed. This allows us to couple to all the m_F sub-levels in D states. To quantify the Rabi frequency and linewidth we measure how the cloud transmission varies for different blue powers. By using the fact that the Rabi frequency of the control field is proportional to $\sqrt{I_c}$, where I_c we can scale it accordingly.

We fit the cavity transmission for one linewidth and then extract the Rabi frequency from it. Then we compare how well the parameters agree when we scale the Rabi frequency with the measured intensity. As we can see in Figure 7.16 the fit for $n = 37\,D_{5/2}$ agrees well when the linewidth $= 0.14\,\gamma_e$ which gives ≈ 450 kHz.

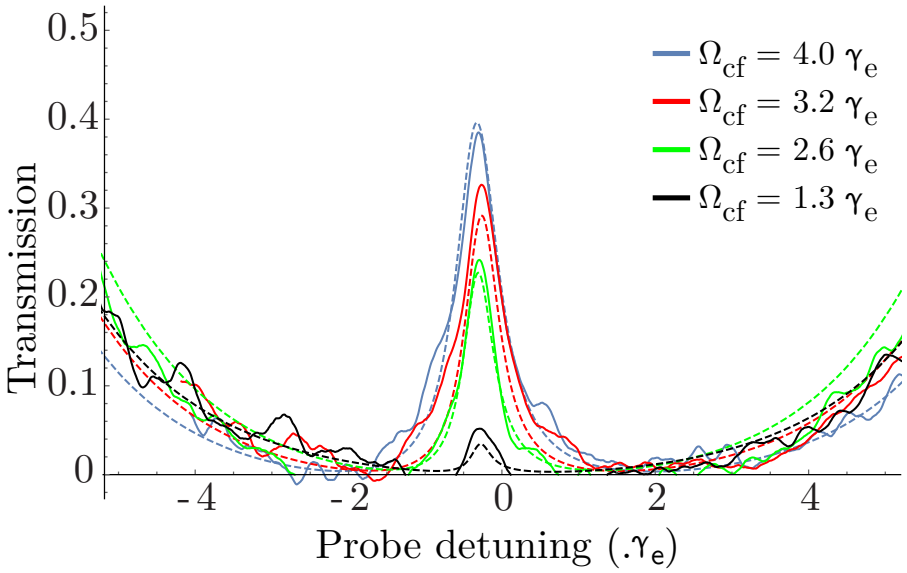

Figure 7.16: **EIT transmission for n =37 $D_{5/2}$ as a function of probe detuning**: Cavity transmission as a function of the probe laser detuning for various control field powers. A fit for linewidth $0.14\,\gamma_e$ agrees well with different Rabi frequencies scaled according to the incident power.

The natural radiative lifetimes are much lower and vary with the principal quantum number. The absence of this variation suggests that the linewidth is limited by different experimental noise sources. The laser linewidth even after optimization couldn't be lower than 50 kHz due to experimental constraints. The Doppler effect is the main source for the broadening, it has been estimated that in the worst case that it could lead to halfwidth at half maximum of ~ 250 kHz for Rb atoms at 40 μK. In addition, AC fields can also broaden the linewidth, as we will show in Section 7.5.3 there is a static electric field of ~ 100 mV/cm.

7.5 Non-linearity measurements

Once we increase the power of the probe beam it creates many Rydberg atoms in the cloud which lead to the creation of blockaded atoms. Thus Rydberg-Rydberg interaction scatter the probe light and the transmitted light starts to attenuate with increasing probe power.

7.5.1 Resonant nonlinearity with Rydberg S state

For S states, the nonlinear effect is induced by a long range and isotropic potential of the form $V(r) = -C_6/r^6$, where r is the interatomic distance and the C_6 coefficient for ^{87}Rb atoms is given by [105]:

$$C_6 \approx \left(63 - 267\left(\frac{n}{60}\right) + 64\left(\frac{n}{60}\right)^2\right)\left(\frac{n}{60}\right)^{11} \text{GHz} \cdot \mu\text{m}^6$$

where n is the principal quantum number. This Van der Waals type of interactions creates a blockade effect in EIT conditions [24], so that the transmission of the

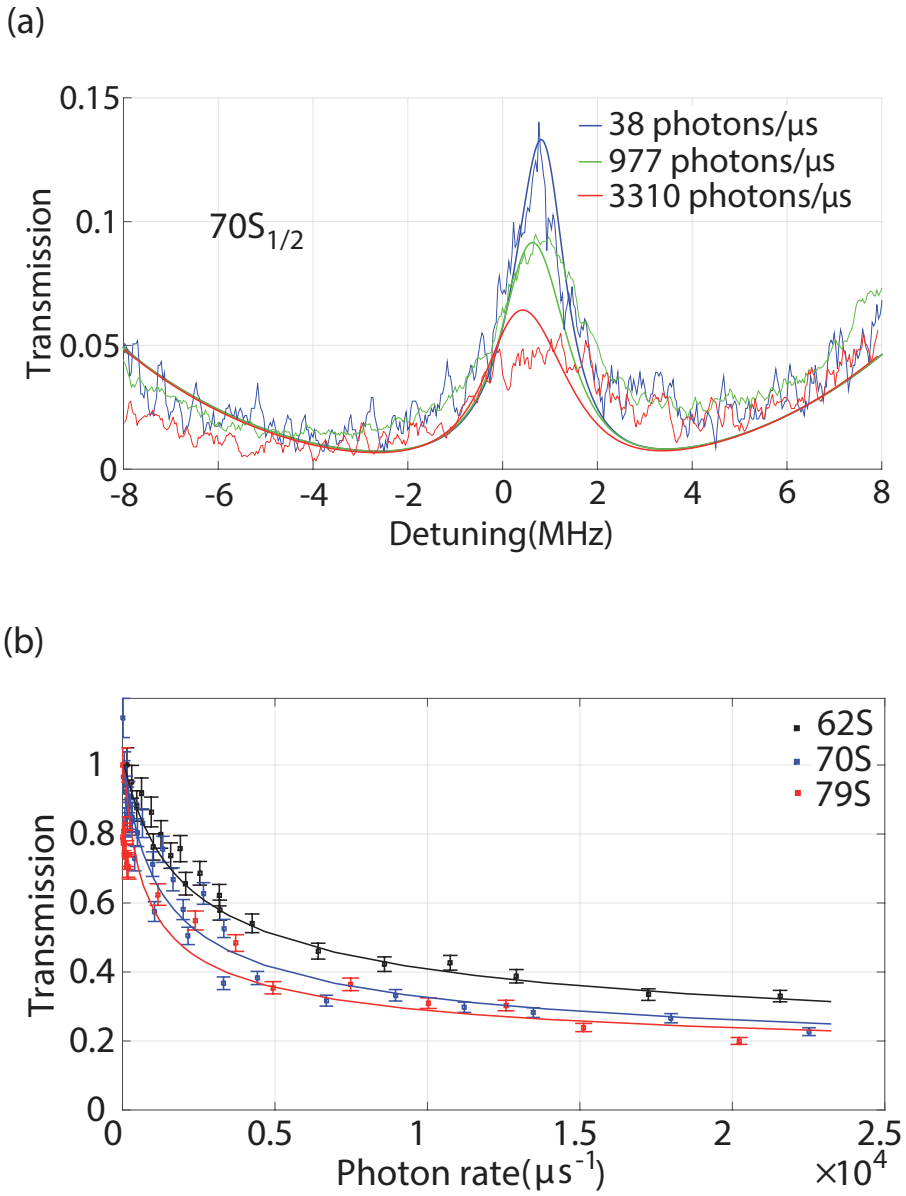

Figure 7.17: **Non-linearity using Rydberg S states**: (a) The cavity transmission spectrum is plotted for various probe photon rates for $70S_{1/2}$ Rydberg state. (b) Cavity transmission at the center of the transparency window as a function of the probe photon rate, for various Rydberg levels. Each curve has been normalized to help their comparison and the inset gives a closer look of the transmission at low photon rates. One can observe the reduction of the transparency with higher photon rate due to the Rydberg blockade effect. The theory is in quite good agreement with the data at any detuning or Rydberg state.

medium decreases with increasing probe field strength. This translates, in our case, to a cavity transmission that reduces with the number of photons. We measured this transmission by scanning the probe for various photon rates (Figure 7.17a). To bring out more clearly the nonlinear absorption, we take the transmission at zero detuning in Figure 7.17a and plot it as a function of the probe photon rate measured with the same probe power for an empty cavity (Figure 7.17b). This procedure has been repeated for various principal quantum numbers, since we expect a stronger nonlinearity for higher n.

We used a mean field approximation to calculate the expected transmission. More details can be found in Section 3.2. The experimental parameters such as the cooperativity, Rydberg state linewidth or the Rabi frequency of control field have been measured (section 7.4.2), leaving no free parameters in the model. The experimental data appears to be in a relatively good agreement with the theory for any probe detuning or Rydberg level (Figure 7.17), at least for small photon rate, i.e. as long as the fraction of blockaded atoms remains small. This is the first experimental test of the model provided in [47] and it seems reliable to predict the nonlinear transmission of the system. Unfortunately due to limited blue intensities we couldn't access higher Rydberg S states. The maximum cooperativity per blockade for the $79\,S_{1/2}$ state is only 0.1 which is not sufficient to observe strong quantum non-linear effects.

7.5.2 Resonant non-linearity using Rydberg D states

Rydberg D-states have higher coupling strength which would allow us to reach high lying states for same blue powers. The eigen modes of the blue cavity determine the polarization of the control field so it restricts our freedom to choose a specific magnetic sub-level. Nevertheless, we measure the Rydberg D state non-linearity by starting with a probe scan in linear regime. We observed that instead of observing a single Rydberg D transition we see multiple transmission lines in EIT spectrum. This can be caused by the stark effect of Rydberg D states.

Stark shift for Rydberg levels

Rydberg states are so sensitive to weak external fields that they are used as electric field probes for very weak fields of the order of tens of micro volts per centimeter [106, 107]. However it can be problematic if any stray electric fields around the atoms are not properly controlled.

In the presence of weak electric field the degeneracy of hyperfine sub-levels is lifted due to the stark effect. This effect can be quantified by considering the hamiltonian of the system where the field is along the z axis. We estimate the splitting for various field strengths using the model in Appendix C .

In our case, a small stray electric field was sufficient to lift the degeneracy as shown in a spectroscopic scan for a high Rydberg level (Figure 7.18a). The observed splittings are in good agreement with a simple Stark shift model [108], see Figure 7.18b.

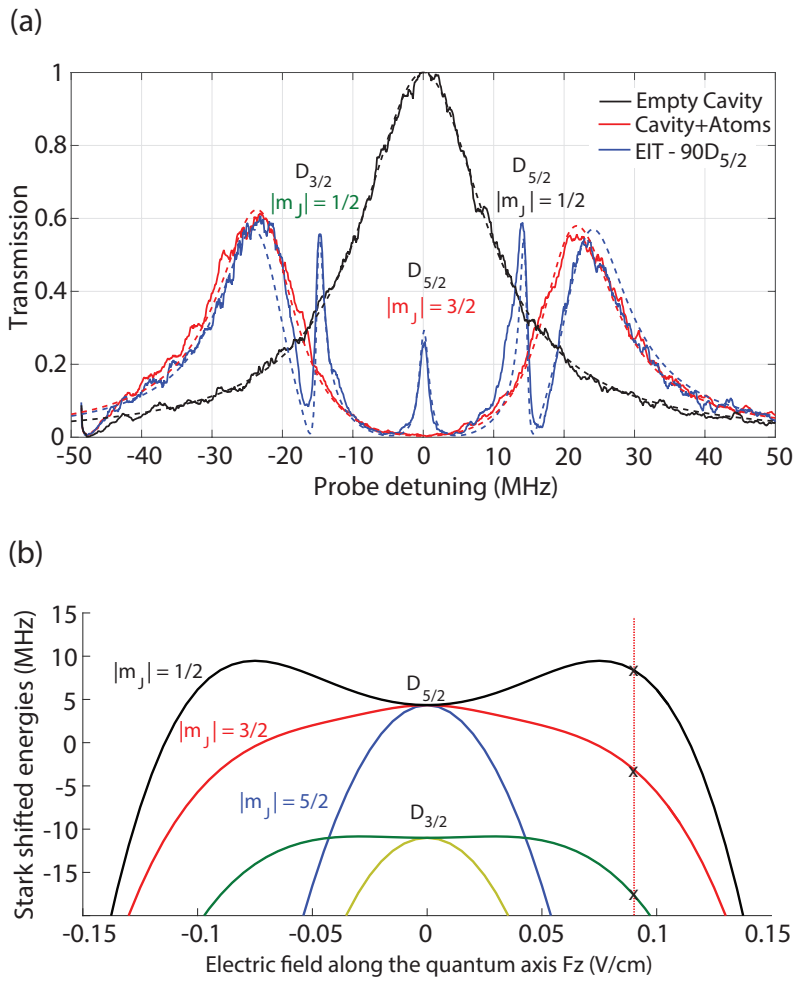

Figure 7.18: **Stark effect on Rydberg D states**: (a) A stray electric field lifts the degeneracy of the Zeeman sublevels of the 90 D states, which creates a transparency window for each transition. (b) Theoretical detuning of the degenerate levels with respect to the electric field in quantization axis. By comparing it to the measured splittings in (a), we can estimate the stray electric field in the quantization axis to be about 90 mV/cm. In order to be in linear regime, the probe photon rate is less than 10 photons/μs.

7.5.3 Dephasing in Rydberg D-States

Compared to S states, Rydberg D states have larger dipole couplings to the intermediate $5\,P_{3/2}$ state, which allows one to reach states with higher principal quantum numbers for the same coupling light intensity, and thus to get higher nonlinearities due to the associated increase of the blockade volume. However, no quantum effects such as anti-bunching have been observed for D states even though several experiments have been conducted to observe a nonlinearity in such systems [35, 76]. One must note two differences with S states which might complicate the blockade effect. Primarily, the Rydberg interactions for D states are anisotropic, they can even vanish for some orientations [109]. This angular dependance has been directly measured for two atoms in the $82\,D_{3/2}$ state [110]. In our model, we considered however an isotropic interaction [96]: $C_6 = 45 \cdot (n/56)^{11}\,\mathrm{GHz}{\cdot}\mu m^6$, averaging the potential in all directions. This simplification allows one to keep analytical calculations tractable, but it prevents one from correctly modeling beyond-mean-field effects related to the anisotropy of the interactions. By exciting atoms to D states

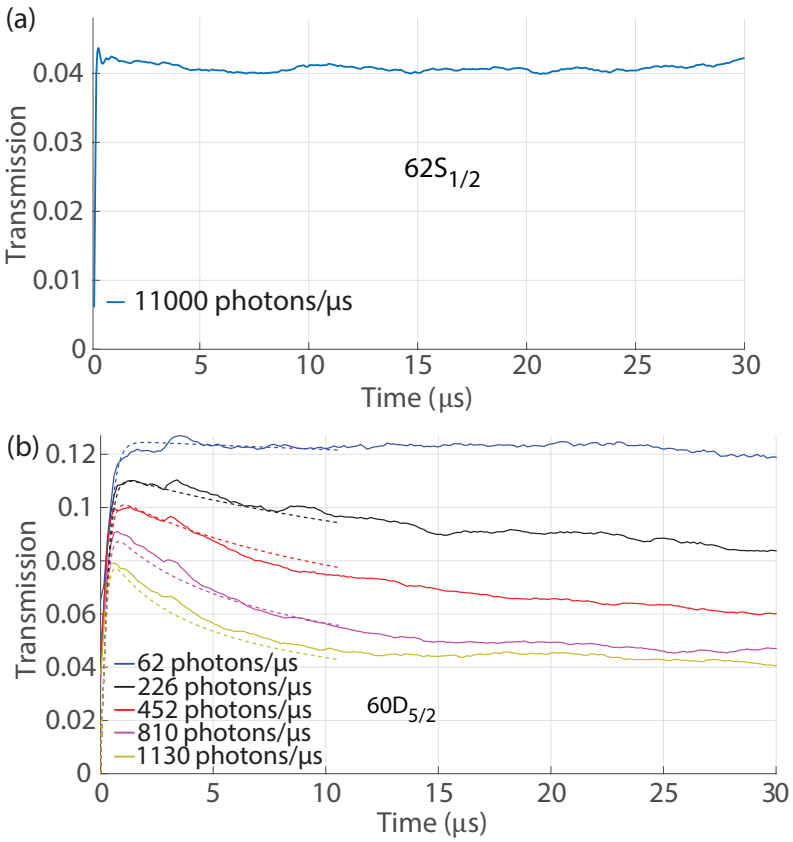

Figure 7.19: **Transient measurements**: Cavity transmission in EIT conditions (probe and control fields on resonance) for S(a) and D(b) states. In addition to a decrease in transmission with the probe photon rate due to the Rydberg blockade, we observe a transmission decay over time for D states. The dashed lines are a model which includes a possible decay of atoms into other Rydberg states that are uncoupled to the control field.

(keeping the probe and control field on resonance), we observe a transient decrease of the transmission during ≈10 μs (Figure 7.19(b)). This dynamical behaviour was also observed in [76] and is neither present for S states (Figure 7.19(a)), nor predicted by the steady-state model we used in section 7.5.1. In addition, we have also observed a decrease in transmission even after switching off the excitation lasers for 10 μs and probing it with a weak probe beam (as shown in figure 7.20). The decay time of 10 μs is far from any timescales present in our steady-state model.

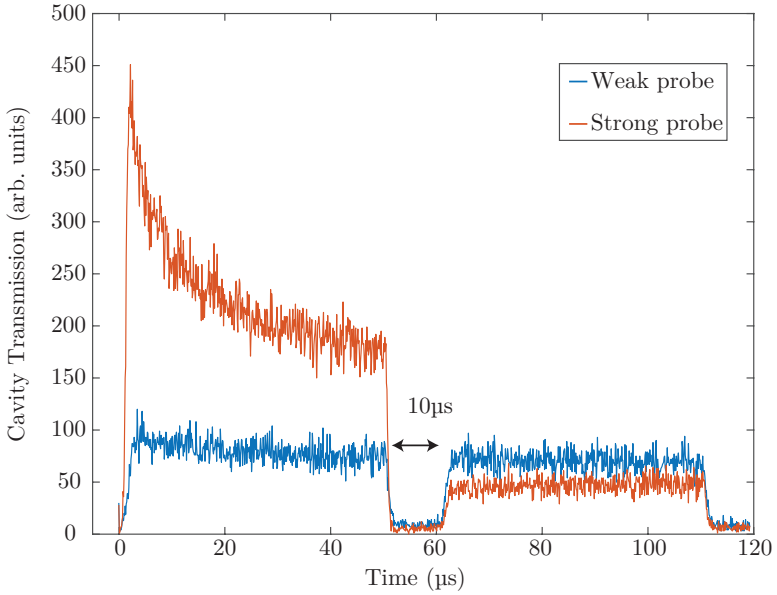

Figure 7.20: **Probing long lived Rydberg D states**: On-resonance cavity transmission in EIT conditions (probe and control fields on resonance) for D states. The first pulse (only red) consists of more than 50 photons/μs while the second pulse red pulse (and both blue) contain less than 10 photons/μs. We observe a transmission decay over time for D states for strong probe fields. This transmission decay also affects the transmission of the weak probe after switching off all the excitation lasers for 10 μs.

To explain the transient behavior, we consider that, because of the anisotropy of D states and their multilevel structure, a Rydberg atom can decay into another level that is uncoupled from the control field, a dark Rydberg level. This process creates long-lived blockading Rydberg atoms which decrease the total transmission. This transient decay, slower than all the timescales predicted by our simple blockade model, is thus the sign of the creation of long-lived blockading atoms. In [76], the experiments performed using Rydberg D states with degenerate Zeeman sublevels exhibited strong dephasing phenomenon. In their model, the decay was also explained by the evolution of Rydberg atoms into such levels. It is therefore interesting to notice that the dynamical behaviour is still present in our case, even when an electric field has lifted the degeneracy.

To account for this process, we included a decay term ξ in the bubble model (see 3.3), to account for the decay rate into "dark" Rydberg states. This gives us a free parameter to fit the curves in Figure 7.19(b). The good agreement with the data - for short times, i.e. when the medium is not saturated with blockade spheres

- indicates that it is a good phenomenological model.

Even while scanning the probe rapidly around the two-photon resonance, we observed a nonlinear transmission similar to S states. The nonlinearity appears to be stronger, although the C_6 coefficient for D states are of the same order. The reason is that the transmission is affected by the creation of long-lived blockading atoms during the scan. Including the decay to dark Rydberg levels into our model allows us to fit the data with good confidenc (Figure 7.21) for all detunings and various principal quantum numbers. We obtained a decay parameter for each principal quantum number: $\xi = \{1.8 \pm 1.7, 2.2 \pm 1.7, 2.3 \pm 1.7, 1.1 \pm 0.66\}$ MHz for $n = \{60, 66, 77, 85\}$, where the error bars contain a 95% confidence interval. It must be noted that once we fix the value of ξ, we observe that it fits very well for different cavity feeding rates. While this parameter allows to fit the data with good confidence, the large incertitude doesn't permit to conclude about its dependence on the principal quantum number.

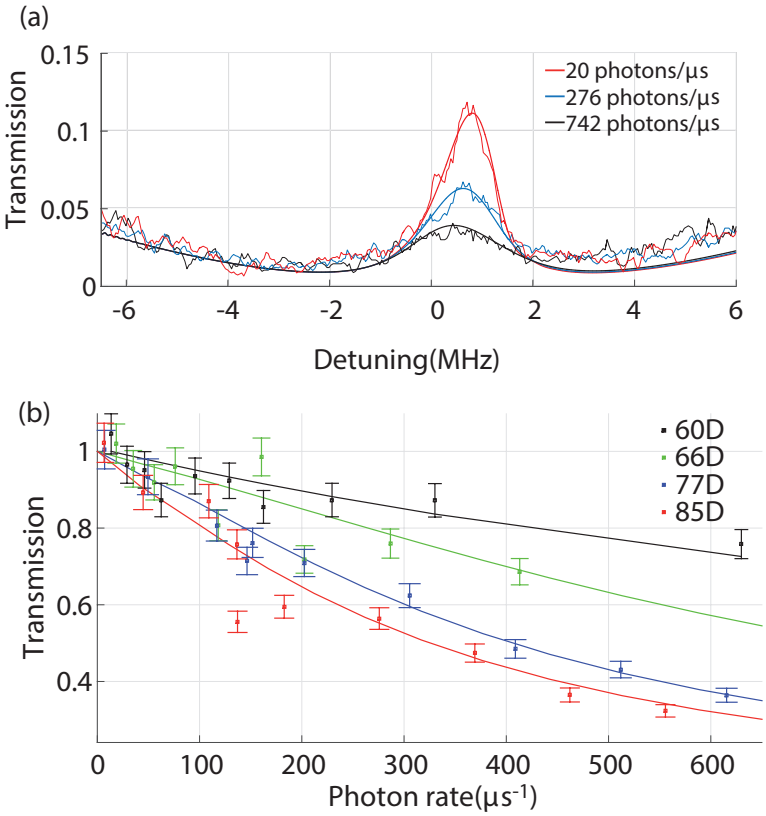

Figure 7.21: **Rydberg D-state nonlinearity**: (a) The cavity transmission spectrum is plotted for various photon rates for the $85\,D_{5/2}$ Rydberg state (b) Cavity transmission at the center of the transparency window as a function of the photon rate, for various Rydberg levels. The model including long-lived Rydberg atoms agrees well with the observed transmission data.

We believe that the creation of such long-lived Rydberg atoms is detrimental to the production of non-classical light states via the blockade-induced optical nonlinearity of the atomic cloud. Indeed, after the medium is saturated with long-lived blockading atoms, the medium has a low transmission, but it has a linear response to an incoming field. This may explain why effects such as photonic anti-bunching have

never been observed in experiments where atoms were driven to Rydberg D states. To use such transitions for quantum optics experiments, this decay mechanism must be circumvented. The above results can be found in the published article [111].

7.5.4 $\chi^{(3)}$ determination

One can quantify the non-linearity by evaluating how many photons one require to observe the bistability in resonator systems. But as the Rydberg atoms evolve in the same time scales as our excitation pulses it is hinders us from observing the bistable behavior. Instead we evaluate the $\chi^{(3)}$ value in the resonant regime using the following expression [97]

$$\chi_R = -\frac{4\sqrt{2}\pi^3\gamma_e\Omega_{cf}^4 C_6\sqrt{|C_6|}}{k^3\sqrt{\gamma_e}[\gamma_e\gamma_r + \Omega_{cf}^2]^{7/2}} \tag{7.5}$$

The susceptibility for our system at $90\,D_{5/2}$ is $7.5\times10^{-7}\,m^2.V^{-2}$„ which is of the same order of magnitude as measured in the free space regime [35]. The main limitations are the capability to reach high lying Rydberg states and the atomic density of our cloud. Even though the susceptibility is not much higher than the free space case, one must take into account the fact that the effects like phase shift induced by the media are amplified by the finesse of the cavity (~ 100).

7.6 Conclusion

In this chapter, we described the two cavities present on our experimental setup. We presented the preparation cycle for a small atomic cloud using a selective depump-repump sequence. Here, we measured the Rydberg resonant non-linearity for both S and D states. We also showed that a semi-classical model can be used to reproduce the Rydberg S state non-linearity and a dynamical dephasing model to describe the non-linear effects for Rydberg D states using long lived dark states. The reasonably good fit suggests that the models are valid for any system where the cooperativity per blockade is smaller than 1.

Chapter 8

Second order correlation effects

Contents

8.1 Second order correlation function 98

8.2 Photon statistics in continuous excitation limit 100

8.2.1 Experimental implementation 100

8.2.2 Photon counting measurements 101

8.3 Squeezing measurements using theoretical model . . . 101

8.4 Squeezing measurements on experiment 102

8.5 Conclusion 104

In order to observe strong resonant non-linear effects one would need the cooperativity per blockade sphere to be larger than one. In our experiment, however, the maximum value we could obtain was 0.1 and 0.2 for the 79 S and 92 D states respectively. For the observed non-linearity, weak correlation effects were predicted using theoretical models.

Rydberg-Rydberg interactions in an atomic cloud is a many body problems and cannot be solved analytically. It is possible to solve the system by perturbatively expanding the system's response in the lowest order of the feeding rate (α) of the system. The average probe field component ($\langle\hat{a}\rangle$) at the lowest order depends only on the first or the third order of the feeding rate. To evaluate the second order effects, we measure the field correlation functions.

After preparing an optically pumped cold atomic ensemble, we study the non-linear response of our system by characterizing the retrieved light using photon counting statistics and homodyne tomography. The calculation of the $g^{(2)}$ function is well described in the articles [46, 47] and in Andrey Grankin's thesis [73]. Here, we will numerically evaluate the function for the parameters of our system. We will also describe the squeezing spectrum measurements of the light transmitted through a cavity.

8.1 Second order correlation function

Rydberg induced optical non-linear effects modifies the statistical properties of light transmitted or reflected from the cavity. To characterize the systems non-linearity, we measure how the cavity can affect the single-photon and two-photon components by tuning the physical parameters such as the cavity detuning, the cooperativity, etc.

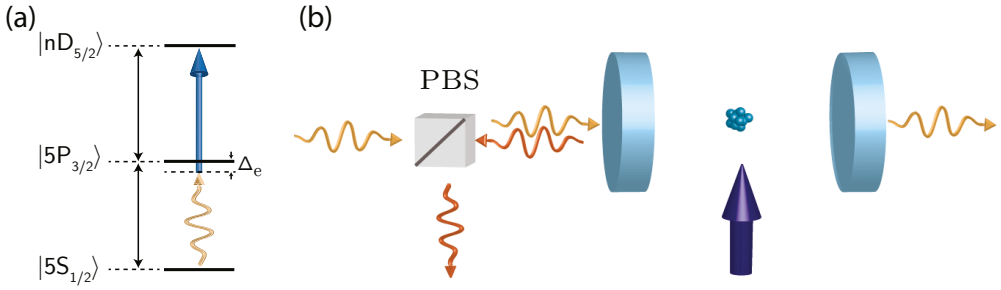

Figure 8.1: **Excitation scheme for photons**: (a) The atoms are excited using resonant beams to the Rydberg transition. (b) The probe beam is coupled to the cavity through 'lossy' mirror and the control beam is coupled from the side of the cavity. The reflected light and the transmitted light are characterized for bunching or anti-bunching nature.

The $g^{(2)}$ correlation function can be used to determine correlations ($g^{(2)}(0)>1$) and anti-correlations ($g^{(2)}(0)<1$) of photons. There are two extreme regimes in which one can probe the system; the dispersive regime where the intermediate state is excited far from resonance and the resonant case where the atoms are on resonance. In the dispersive regime, as the atoms are off-resonant the intermediate state remains mostly unpopulated and the system of equations can be solved by adiabatically eliminating the coherence terms. The system effectively behaves as two level atoms and can be solved numerically using the Rydberg bubble approximation [46].

Resonant case

The effective two level system is no longer applicable in the resonant case. In order to calculate the correlation function, we expand it using the factorization of the lowest perturbative order of the operator product averages.

In reflection

According to Andrey Grankin's analysis [73], the observed effects can be explained by the fact that the impedance matching condition is different for single and double photon component. The $g^{(2)}$ function of the reflected or the transmitted light is an indicator of the photon number distribution.

We consider the volume of the cloud to be around $(\sqrt{2\pi}\times 35)^3\ \mu\text{m}^3$. For the Rydberg $79\,S_{1/2}$ state the C_6 coefficient is $\approx -3.6\times 10^3\,\text{GHz}\cdot\mu\text{m}^6$. For $\Omega_{cf}=2$, the impedance matching condition is satisfied for the single photon pairs when $\Omega_{cf}=2\sqrt{\gamma_e\gamma_r(2C-1)}\approx 2\gamma_e$ which gives a cooperativity of 5. Hence, we observe a strong bunching correlations in this regime (refer Figure 8.2).

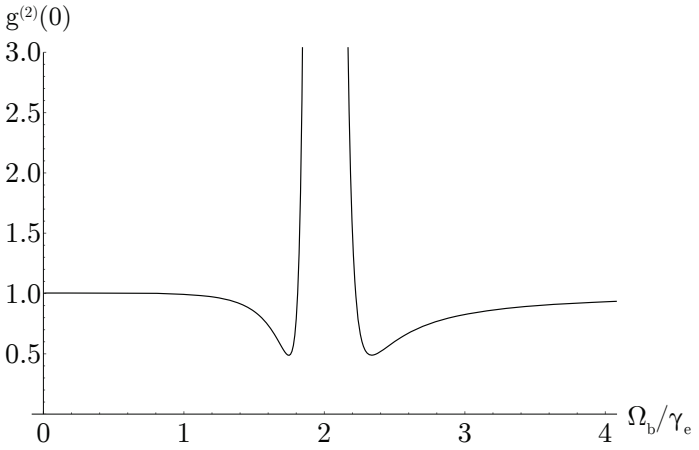

Figure 8.2: $\mathbf{g^{(2)}(0)}$ **on resonant in reflection**: The correlation function of the reflected light is plotted with normalized control field Rabi frequency Ω_{cf}/γ_e when $\Delta_e = \Delta_c = \Delta_r = 0$

In transmission

We evaluate the correlation function for the transmitted light around the same range of parameters i.e. for C = 5, $\Omega_{cf} = 3$ and the control field detuning (Δ_c) is set to zero. In Figure 8.3 we plot the $g^{(2)}(0)$ function against the detuning of the probe field. We observe that there is a strong anti-bunching correlation in transmission. It is important to note here that while the correlations are weak in the transmission field, the probe field is not completely absorbed by the cavity. Hence, in the transmission case it is more likely to detect the correlations.

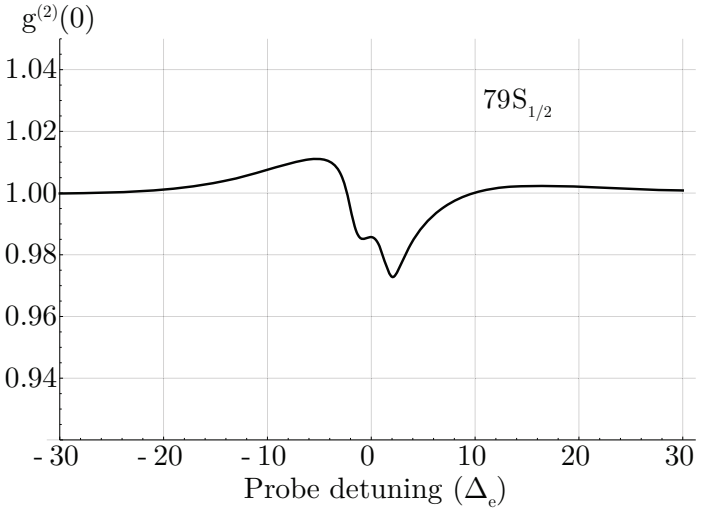

Figure 8.3: $\mathbf{g^{(2)}(0)}$ **in transmission**: The correlation function of the transmission as a function of intermediate state detuning Δ_e/γ_e when $\Delta_c = \Delta_r = 0$. The transmitted light exhibits weak anti-bunching close to the resonance for a control field Rabi frequency of $3\gamma_e$.

8.2 Photon statistics in continuous excitation limit

The steady state response of the system can be studied by using a weak continuous probe light. In free space, the transmitted light through a Rydberg cloud displayed anti-bunching correlations [37]. In cavity systems, correlation experiments have never been performed till date.

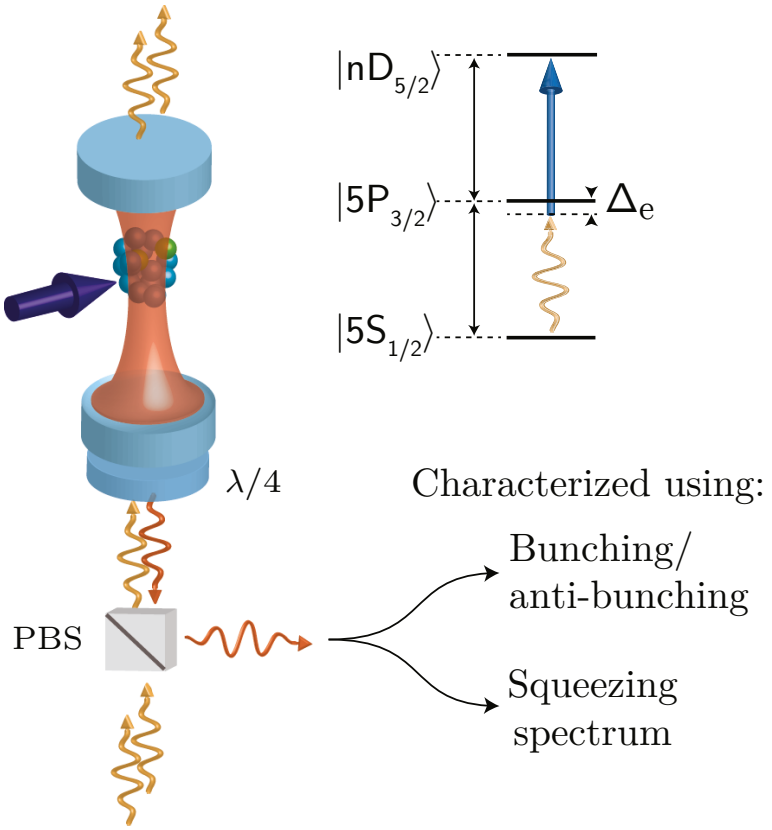

Figure 8.4: **Excitation scheme**: The probe light is coupled through the low reflectivity mirror in a weak feeding regime (few photons per intermediate liftime). The cavity detuning and various parameters can be tuned to achieve impedance matching conditions for single photon or two photon component. The reflected/ transmitted light is later on analyzed for bunching/anti-bunching effects or squeezing spectrum.

8.2.1 Experimental implementation

As it is easier to detect strong correlations, we studied the system in reflection first. By using a polarization beam splitter, we separate the incident and the reflected light. The measured signal is an interference between the light reflected from the bottom mirror and the leaked light from the intra-cavity field. By tuning the probe detuning, one can move the impedance matching condition from single photon state to two-photon states.

In the previous section, numerical calculations suggested that bunching/anti-bunching correlations can be observed depending on the experimental parameters.

We can therefore expect to see, $g^{(2)}(0) > 1$ for a resonant probe field when the impedance matching condition is set for single-photon component.

8.2.2 Photon counting measurements

The cavity is locked on resonance with atoms and the atomic cloud is prepared in the similar manner as the non-linearity measurements. According to numerical calculations, the correlation effects are observed both in transmission as well as in reflection. But the range of parameters necessary to observe non-linear effects in reflection correspond to the impedance matching condition where almost all the light is absorbed. Due to fluctuating cavity resonance and the oscillating control field Rabi frequency (Ω_{cf}) the system is pushed out of the impedance matching condition.

In transmission

Once the cloud is prepared, we shine a resonant probe on the cavity and look at the transmitted signal using two SPCMs. We look at the correlation effects between the two SPCM signal output under resonant EIT conditions (as shown in Figure 6.1). According to numerical simulations, we must observe a weak anti-bunching close to 0.98 at resonance. Even after averaging over several cycles, the instability of cavity resonance didn't allows us to observe the expected anti-bunching effects on the transmitted light. By going Rydberg D-states one could have higher cooperativity per blockade which in turn can lead to stronger correlations, but the dephasing effect inhibits us from the observation of any higher order correlation effects.

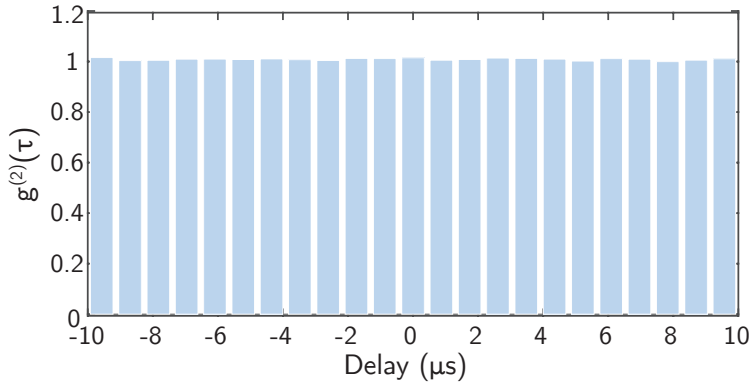

Figure 8.5: **Intensity correlation measurement**: The $g^{(2)}$ function of the transmitted light is measured for the Rydberg state $79\,S_{1/2}$. The stability of the cavity lock and small cooperativity per blockade prohibit us from observing strong non-classical effects like anti-bunching.

8.3 Squeezing measurements using theoretical model

Measuring the squeezing spectra of the cavity system gives us an insight into the rich physics of Rydberg EIT that is at play. In order to evaluate the correlation effects

beyond the lowest order effects, Andrey Grankin with Etienne Brion evaluated the squeezing spectrum using the Schwinger-Keldysh contour formalism [112]. Using this method it is possible to evaluate the transmission spectrum of the probe light at a priori given order. It is defined as normally ordered noise spectrum of the optical field in a steady state regime.

We use a typical resonant parameters i.e. $\gamma_r = 0.14\gamma_e$, $\Delta_c = \Delta_e = \Delta_r = 0$, n = 62 $S_{1/2}$, C = 5. We evaluated the squeezing spectrum for weak non-linear systems. Numerically, it was found that an observable phase-dependent squeezing could be observed even at small cooperativity per blockade. The phase noise of the transmitted light at zero frequency can be seen in Figure 8.6.

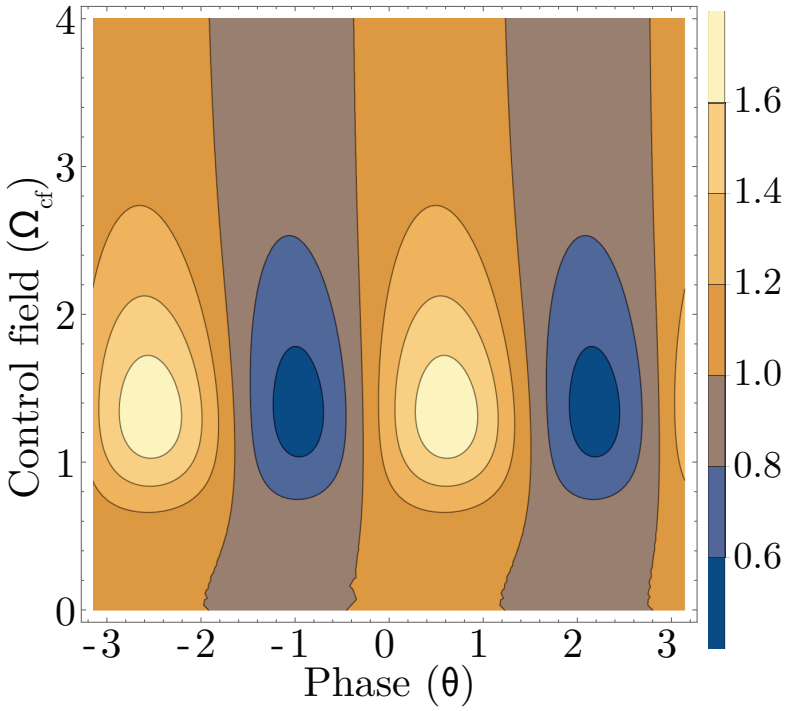

Figure 8.6: **Phase dependent quadrature noise induced by Rydberg-Rydberg interactions**: The contour plot of expected phase dependent quadrature noise at zero frequency of the transmitted light for n = 62 $_{1/2}$ and $\alpha = \sqrt{80}\gamma_e$ plotted against the relative phase between the LO and the probe. The quadrature noise is normalized to shot noise. On the vertical axis we can see its dependence on the control field Rabi frequency.

8.4 Squeezing measurements on experiment

We evaluate the squeezing spectra using the homodyne method described in Section 6. The phase dependent quadrature noise measurements is normalized to vacuum noise. We use n = 62S state to avoid any dephasing effects present in Rydberg D states. All the beams were excited on resonance, and we probe the transmission spectra of a resonant cavity. As we have shown in Chapter 6, the probe laser has an inherent phase dependent noise coming directly from the laser. Nevertheless,

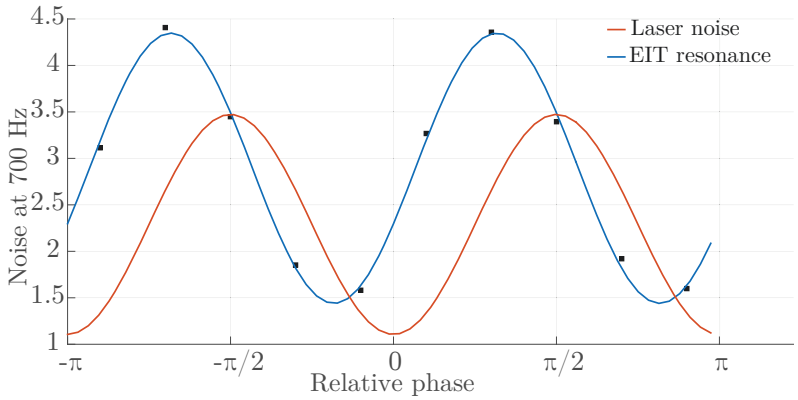

Figure 8.7: **The normalized phase dependent noise of transmitted light for n = 79 $S_{1/2}$**: The quadrature noise at 700 kHz as a function of relative phase between LO and probe is measured in the absence of atoms (red) and in the presence of resonant EIT conditions (blue).

we measured the squeezing spectra in transmission for various phase values and we observe a relatively small phase shift with a slightly larger amplitude.

The rotation of the noise squeezing can be explained by a linear cavity system with a control field slightly detuned by -0.5γ_e. We didn't assume any non-linear effects in the model and observations are very well reproduced by the model. while we used all the beams close to resonance the most likely explanation could be moving cavity resonance or the control field.

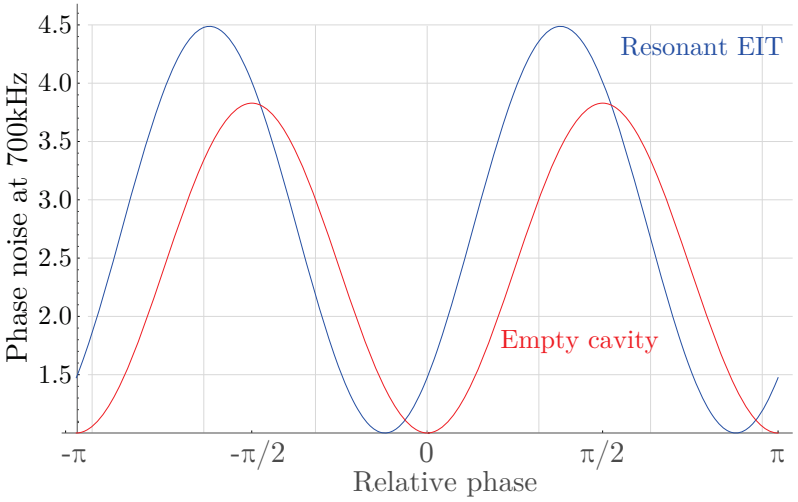

Figure 8.8: **The normalized phase dependent noise using a linear EIT model**: The observation of rotated noise spectra on the experiment can be explained by a slightly detuned control field ($\Delta_c = -0.5\gamma_e$). In addition, the noise on the cavity resonance frequency adds to the already existing phase noise.

It is not possible to filter this noise even by using a narrow band pass cavity as it is intensity dependent. The easier alternative is to increase the non-linearity of system by increasing the cooperativity per blockade. As the goal of our experi-

ment is not to observe squeezing which can be observed even simpler systems, we concentrated our efforts on moving towards quantum non-linearity.

8.5 Conclusion

In this chapter, we show that the second order effects can be used to study the non-linearity of the system. We used numerical models developed by Andrey Grankin and studied how our system behaves under various resonant excitation schemes.

We measured the second order correlation function of the transmitted light but the fluctuations in the cavity resonance and the control field stamped out the correlation effects. In reflection, the bunching/anti-bunching correlations are observed only near the impedance matching condition where almost all the light is scattered. In transmission, the $g^{(2)}(\tau)$ measurement was found to be the same as a coherent beam. This led us to conclude that the weak non-linear effects coupled with the experimental noise can damp out the correlation effects.

We showed that even with a laser with inherent phase noise, we can still study the physics of the Rydberg-EIT system. The observed rotation of the squeezing spectra was reproduced using a linear EIT model.

Conclusion

In this chapter we demonstrated how a small atomic cloud of few tens of microns size is loaded into three crossed dipole traps. The selective spatial preparation enables us to load atoms with very short duty cycles and large number of atoms. A build up cavity was installed to increase the power of the coupling beam such that it allows us to excite atoms to n = 95 for D states.

Experimentally, we couple to Rydberg states using resonant EIT transition. Absorptive non-linearities were measured for both Rydberg S and D states. We developed theoretical models which explains the observed non-linearity with very good precision. The stark splitting created by weak electric field has been characterized and agrees reasonably well for different Rydberg D states. The cooperativity per blockade of the current system even when excited to highest possible Rydberg states is limited to 0.2 for n = 90 $D_{5/2}$ states and 0.1 for n = 79 $S_{1/2}$ states.

In addition, we also worked on observation of second order effects which helps us in giving a better understanding of the physics of our system. The correlation function of the transmitted or reflected light was evaluated perturbatively using second order expansion of feeding light. Unfortunately, the fluctuations of cavity moves the system out of resonance and averages the correlation effects.

The squeezing spectra gives more information about the higher order effects in the system. We measured and characterized the phase noise of the laser. In addition, we also explained the increased anti-squeezing observed through our cavity system using a linear model. We showed that these detection methods can help us understand more in details the physics of Rydberg-Rydberg interactions.

Part IV

Towards Quantum Optical Non-linearities

Chapter 9

Towards quantum optical non-linearities

Contents

9.1 Introduction 109
9.2 Quantum regime 110
9.3 A new cavity system 111
9.3.1 Design 112
9.3.2 Installation and alignment of the cavity 114
9.3.3 Characterization of the cavity 115
9.4 Cooperativity and EIT measurements 118
9.4.1 Cooperativity measurement 118
9.4.2 EIT measurement 118
9.5 Possible schemes to exploit 119
9.5.1 Off-resonant excitation 120
9.5.2 On-resonance excitation 121
9.5.3 Cavity phase shift 121
9.6 Photonic controlled-phase gate proposal 123
9.7 Conclusion 125

9.1 Introduction

The observation of large classical non-linearities have encouraged us to find ways to improve the experimental setup even further. In free space, large non-linearities require a large single Rydberg sphere of the same order of magnitude of the atomic cloud [41]. In our system by using the cavity new schemes can be imagined where the Rydberg blockade sphere doesn't have to be very large. We will show that we can engineer a photonic gate using atomic systems without moving towards the cavity QED regime. This chapter will give an overview of our current efforts to

increase the optical non-linearity of our system. In addition, we will also present multiple proposals through which we can probe the quantum optical non-linearities using correlation measurements and homodyne tomography.

An important parameter for observation of strong non-linear effects is the cooperativity per blockade. As we have observed in the previous experiment, the highest cooperativity per blockade we could achieve was about 0.2. To increase this value one must either have very large atomic densities ($> 10^{11}$ atoms/ cm^3) [113] or higher finesse cavities.

Naively, one might assume that we can simply increase the repumper power in the preparation cycle which would efficiently repump all the atoms in the crossed dipole trap. Unfortunately, as we increase the repumper power, the size of the atomic cloud also increases as the atoms are repumped by its gaussian tail. Since, it leads to the same or even smaller atomic density, we didn't resort to this method. Without increasing the finesse or decreasing the cloud size the optical non-linearity we can achieve is limited.

9.2 Quantum regime

If we use a small interacting mode-volume then it is easier to saturate the optical response by even a single Rydberg bubble. Hence, one must resort to higher finesse cavity with smaller mode waist to move to quantum regime. We therefore decided to change the cavity mirrors while still having the same length such that we could have a mode waist close to 15 μm with a finesse of 1000 as proposed in [46].

Rydberg bubble estimation

The cloud's non-linearity depends on the cooperativity of the single Rydberg sphere. In order to have an estimate of the cooperativity per blockade sphere in the new cavity setup we consider the expression of the blockade volume on resonance [96]:

$$V_b = \frac{\sqrt{2}\pi^2}{3}\sqrt{\frac{iC_6}{\gamma_r - \frac{\Omega_{cf}^2/4}{\gamma_r+\gamma_e-\Omega_{cf}^2/4\gamma_e}}} \tag{9.1}$$

where C_6 is the van der Waal's interaction coefficient. The value of C_6 was measured using dispersive/absorptive non-linear measurements and its value is given by C_6/γ_e = 35700 μm^6 for n = 61. For any Rydberg state n it scales as $C_6(n) \approx 35700 \times (\frac{n-1}{60})^{11}$

Figure 9.1 shows the real part of V_b as a function of Ω_{cf}, for several different possible values of γ_r for n = 95. It might seem that the blockade size is large for smaller control field Rabi frequency, but it manifests from the fact that the Rydberg excitation linewidth is not broadened by the coupling powers lower than 1.

Starting with the parameters from the previous system, where the cloud is 30 μm and the cooperativities are between 8-10, Since we need enough blue Rabi frequency to observe EIT at low power, we are somewhere on this curve where the value of V_b does not depend on γ_r, and is of the order of 10000 μm^3. Typically, the cloud has a measured cooperativity of ≈ 8, and an estimated density profile is proportional to

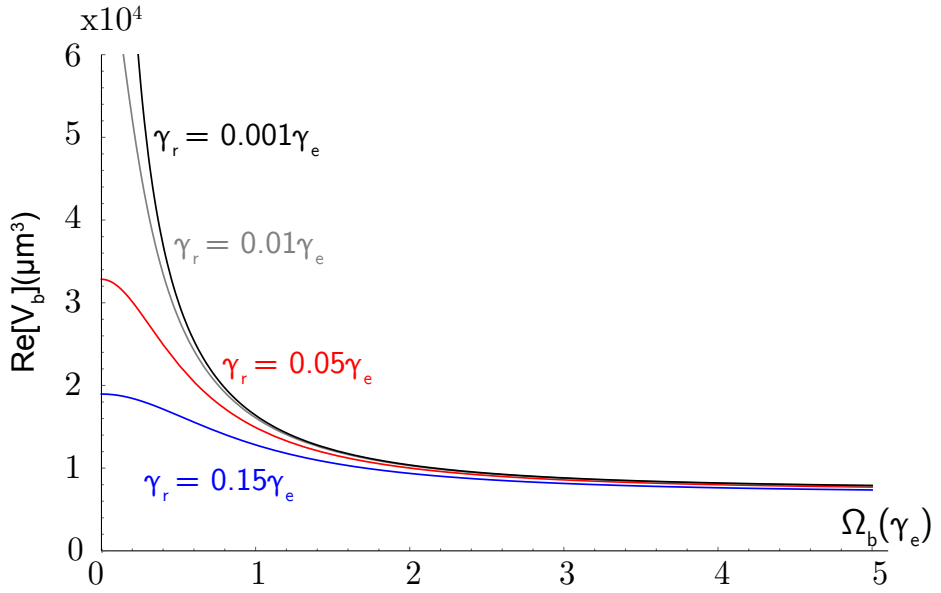

Figure 9.1: **Rydberg blockade volume dependence on the control field Rabi frequencies**: The blockade volume depends strongly on the Rydberg linewidth. The blue curve corresponds to the measured EIT linewidth of ≈ 450 kHz

$e^{-r^2/2R^2}$ with R of the order of 30 μm, which corresponds to a total effective volume V = $(\sqrt{2\pi}\mathrm{R})^3 \approx 400000\,\mu m^3$

Based on these estimations and considering Re$[V_b]$ as the interesting quantity, one sees that the cloud can contain typically 40 blockade spheres, and the "cooperativity per blockade sphere" should be $8/40 = 0.2$ which agrees well with our measurements.

If we have a cavity with a finesse 10 times higher and waist 5.67 times lower than the current cavity then each atom's cooperativity ($\propto \mathcal{F}/\omega_0^2$) will increase by 320, for the same number of blockaded atoms, we can have a $C_b \sim 64$. But by going to very high C_b, the cooperativity also increases and we lose the EIT transparency window since the control field power is limited. To circumvent this problem, we can lower the atomic density to decrease the cooperativity of the new system upto 100. If we assume that only the atoms which are in the cavity mode of 15 μm waist take part then we can have an effective volume V = $(\sqrt{2\pi}15)^2(\sqrt{2\pi}30) \approx 100000\,\mu m^3$. By using approximately the same blockaded volume, as we have now, the cloud can contain upto 10 blockaded spheres and the "cooperativity per blockade sphere" is still reasonably high. Even with a $C_b \sim 10$, we are in a good range of parameters where quantum non-linearities should be observed. Another alternative would be to explore the dispersive regime where we can work with very high cooperativities [48].

9.3 A new cavity system

The design of a one-sided cavity with a very narrow mode-waist is challenging because of the already existing constraints. As mentioned in the previous part, the distance between the mirrors must be set close to 6.6 cm to be able to address

atoms present in both hyperfine levels $5S_{1/2}$ F = 1 and F = 2. In addition, the MOT must be situated about 22 mm from the top mirror to have the maximum overlap between the two different standing waves.

9.3.1 Design

In order to obtain the smallest gaussian waist size one must move closer to the concentric configuration [114]. Given the restrictions with the MOT position, the inner radius of curvature of the top mirror and the bottom mirrors are fixed to $r_t = 2.2$ cm and $r_b = 4.4$ cm respectively. To achieve a finesse of 1200 at 780 nm, the bottom and top mirrors have a special coating to have a reflectivity of $R_1 = 99.5 \pm 0.15\%$ and $R_2 > 99.9\%$ at 780 nm. In addition, to be able to couple blue light to the atoms along the cavity axis, the mirrors are specially coated to have $R_1, R_2 < 2\%$ at 480 nm.

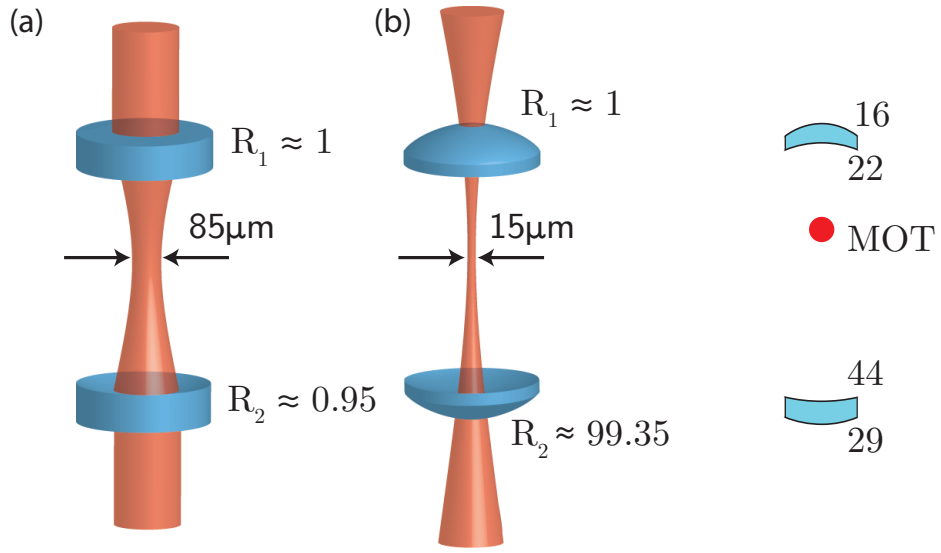

Figure 9.2: (a) Old cavity setup with a finesse of 120 and waist of 85 μm. (b) New cavity setup with a finesse of 1200 and waist of 15 μm

Mode waist calculation

The stability of a cavity depends on the distance between the mirrors (l) and their inner radius of curvature. By convention, we define $g_i = 1 - \frac{l}{r_i}$ and the stability criterion is given as $0 < g_t g_b < 1$. The mode waist can be written as

$$w_0 = \sqrt{l\lambda/\pi}\left[\frac{g_t g_b(1 - g_t g_b)}{(g_t + g_b - 2g_t g_b)^2}\right]^{0.25} \tag{9.2}$$

To obtain a mode waist of 15 μm, the cavity length has to be set to 57 μm shorter than concentric case. This gives us the beam waist at the top mirror using $\omega_t = \sqrt{\frac{L\lambda}{\pi}}\left(\frac{g_b}{g_t(1-g_t g_b)}\right)^{0.25} = 364\,\mu m$, and the bottom mirror $\omega_b = 728\,\mu m$. As the nearest

viewports to the mirrors are atleast 30 cm away from them, it is better to curve the external surfaces of the mirrors to minimize the size of the beam outside the chamber.

Spherical aberration

In order to avoid the spherical aberration due to the edges of the curved surfaces, we fix the outer radius of curvature where the incident beams are orthogonal to the concave side of the mirror. If we assume the mirror has a thickness t and refractive index n then the $r_{out} = \frac{n}{n+1}(t + r_{in})$. This means the outer radius of curvature has to be set to ≈16 mm and ≈29 mm to minimize spherical aberrations. With this configuration the main contribution for the aberration arises from the external optics.

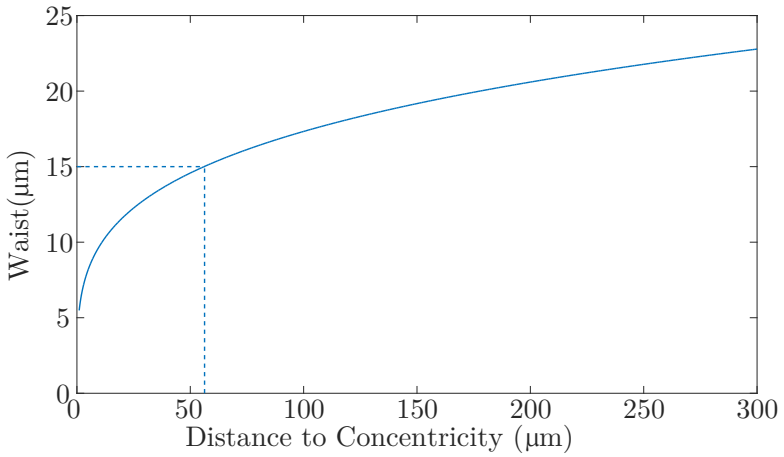

Figure 9.3: **Minimum waist attainable vs. distance to concentricity**: The minimum waist attainable for mirrors with fixed radius of curvature depends on the distance between them. The minimum waist occurs when the separation between the mirrors is equal to the sum of radius of curvatures $(R_1 + R_2)$. For a waist of 15 μm the cavity length should be 57 μm shorter than 66 mm.

In addition, we also took into account that the beam size at the viewports of the vacuum chamber are not bigger than them and any optical element cannot be placed at least 30 cm away from the mirrors.

Length Stabilization

As the top three piezos have to move the whole cavity holder setup from outside the vacuum, the length fluctuations at high frequencies (>50 Hz) couldn't be compensated. In order to circumvent this problem, a new piezo was installed to stabilize the cavity length. The only possibility was to install it under vacuum on the bottom mirror, which brought certain constraints on its shape and access. We use a ring type piezo with an inner diameter of 9 mm and outer diameter 15 mm, from Noliac, to allow light to be freely coupled in and out of the cavity. With a travel range of 3 μm it gives us enough room to scan over 3 FSR. The piezo can be placed under

UHV conditions and is glued to Kapton wires (with a SMA connector). We use a DN40 CF flange with a SMA feed through to supply voltage to the piezo.

In addition, the stabilization system we established for the previous cavity doesn't work because of the Ti-Sa broad linewidth even after locking its frequency. The 810 nm Ti-Sa laser has a modulation at 100 kHz on its output which inhibits us from using it to stabilize the cavity. The only solution is to use a new diode at 810 nm to lock the cavity. In the previous resonator, we needed a locking beam of 10 mW to create a 300 μK trap but in the new cavity we only need about 1 mW because of the finesse improvement.

Bottom mirror holder

Initially, the bottom mirror is attached to the cavity holder using a hollow cylinder and a cap with a spring. In order to eliminate all sources of instability, a new single piece is designed to hold the bottom mirror to minimize cavity length fluctuations.

Figure 9.4: **Configuration of the bottom mirror**: (a) To minimize any fluctuations, the mirror and the piezo are glued using a triangular ring adapter to maximize the surface contact. A non-conducting glue is used to minimize any potential contacts between the electrodes of piezo and other surfaces. (b) **Bottom mirror holder**: A single piece was designed without any springs.

9.3.2 Installation and alignment of the cavity

Opening a vacuum chamber requires extreme care as it brings the inner parts in contact with external gases and possibly oils. To avoid that, we used two turbo pumps one connected to the main chamber and the other to the LVIS chamber to pump the system rapidly. Both of them are pumped down to 10^{-7} mbar before opening the valve, which connects them to the vacuum chambers. Once we reach an equilibrium, dry nitrogen gas is slowly pumped into the system without letting any moisture in. After the vacuum chambers reach room pressure, we unscrew the cavity mount from the system while still pumping in dry N_2 gas. The cavity mirrors were replaced and the bottom mirror was glued to the holder to minimize vibrations. The pieces were baked at 120°C to remove any trapped gases from the surface.

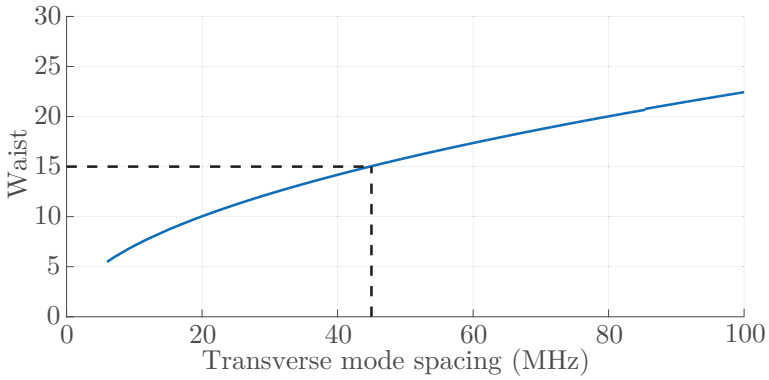

Figure 9.5: **Waist size of the TEM00 mode as a function of the frequency spacing between the higher order TEM modes:** To precisely adjust the cavity length to achieve a cavity mode waist of 15 μm we use the screws and piezos to attain a frequency spacing of 45 MHz.

Alignment

As the cavity is very close to concentricity, it is a challenging task to align it without any access once it is set under vacuum. As the cavity's length determines the fundamental mode waist, we need to set the cavity length exactly to 55 μm away from concentricity. We measure the reflected light from the bottom mirror as it is easier to observe losses on a non-zero signal. The cavity reflection is monitored using a photo diode while its length is scanned. In order to have an easy starting point, we start with a cavity length close to 6.5 cm and align the optical beam to the cavity mode. Once we couple some light to the first few TEM modes, we measure the frequency spacing between the modes.

We assume that the incoming beam is gaussian and we evaluate the higher order modes of the cavity, which gives us the frequency spacing between the modes for various cavity lengths as shown in Figure 9.5. In order to have a waist of 15 μm, the frequency spacing between the TEM modes is 45 MHz. We coarsely adjust the cavity length using the screws and precisely by using a constant DC voltage on all the three piezos. Once the length is set such that the spacing is close to the estimated value, we optimize the cavity on the fundamental gaussian TEM00 mode. In Figure 9.6 we can observe the various TEM modes excited inside the cavity for different lengths.

9.3.3 Characterization of the cavity

In this section we will describe the set of measurements carried out to characterize the newly installed cavity by measuring the finesse and the intracavity losses. The factory measured reflectivity of the mirrors are 99.4 $\pm$0.1% and $>$ 99.99% at 780 nm. The transmission for both the mirrors at 480 nm is $>$ 98%.

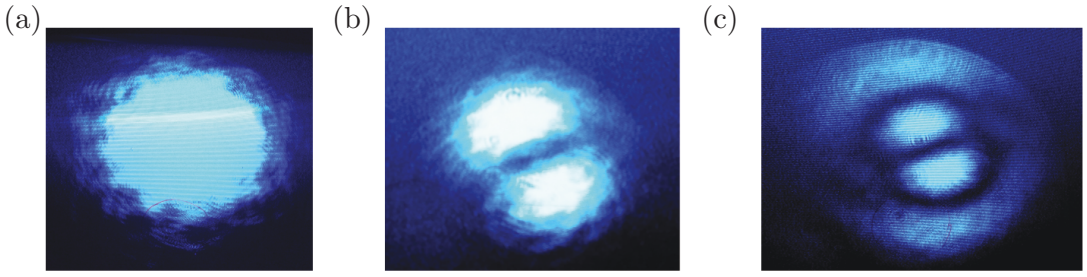

Figure 9.6: **Different cavity modes excited**: The cavity's length is adjusted to excite various TEM modes (a) TEM00 (b) TEM01 (c) TEM11

Cavity finesse measurement

We determine the resonator lifetime by scanning the cavity length linearly. We create two side bands on a beam at a known frequency to allow us to determine rate of the scan. By measuring the reflection from the cavity we determine that the HWHM is $\approx 2\,\mathrm{MHz}$, it corresponds to a finesse $\mathcal{F} \approx 500$ (as shown in Figure 9.7). It is considerably lower than what we initially expected and it can be attributed to 0.4% intracavity losses caused by some dust particle. The reflectivity of the bottom mirror was found to be $\approx 99.35\%$.

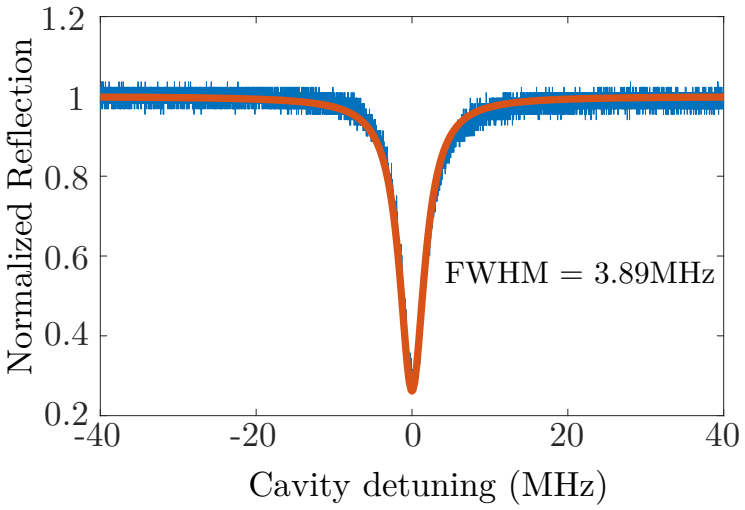

Figure 9.7: **Cavity linewidth measurement**: The reflection signal from the 'lossy side' of the cavity when the probe frequency is varied around the cavity resonance. By using the depth and the linewidth we estimate the intracavity losses and the reflectivity of the bottom mirror.

We spatially repositioned the beam to avoid any dust crept onto the surface while installing the system. Despite our best efforts, we couldn't achieve a higher finesse. As the estimated intra-cavity losses are lower than the reflectivity of the bottom mirror, hence it should allow us to observe the impedance matching condition in reflection.

Parameter	Value
Linewidth - FWHM	≈ 3.9 MHz
Mode waist	$15\,\mu$m
Finesse	555

Table 9.1: **Main cavity parameters**

Cavity stability

Even in the presence of dust, we could couple efficiently to the fundamental mode without scattering light into other modes. The locking scheme is similar to the previous cavity, we use a 810 nm auxiliary beam with side bands at 100 MHz. Instead of acting only on the top mirror, we act on the top one for slow large drifts and on the bottom one to compensate noise at high frequencies (above 50 Hz). We can use the same error signal for both the locking loops of top and the bottom mirrors, but any sharp movements disturbs the slow piezos enough to move it out of resonance.

To start with, we stabilize the length using only the fast piezo, but over a few hours the cavity drifts longer than the range over which we can act on. We use a low pass filter on the error signal to allow frequencies only below 50 Hz and use this to compensate for large drifts using the slow piezos.

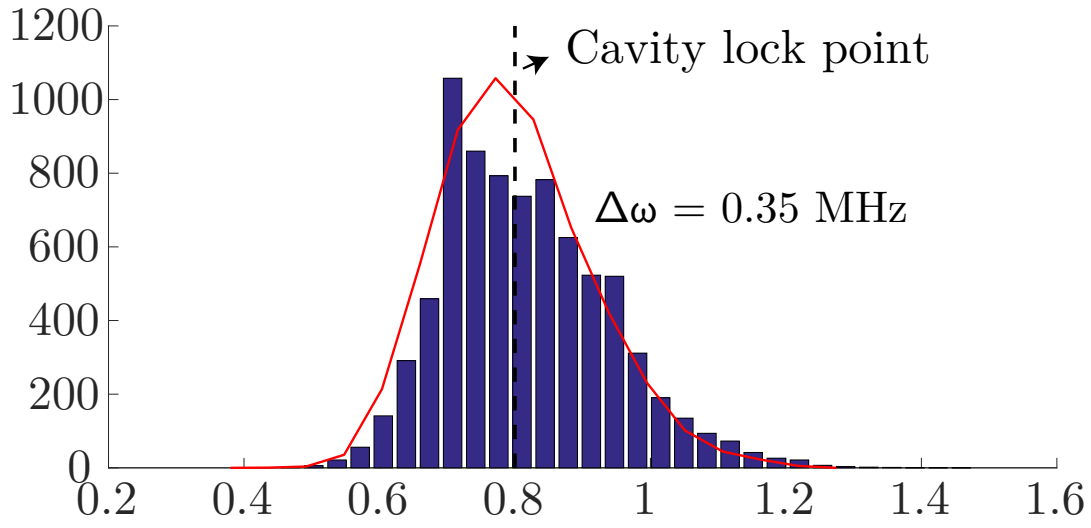

Figure 9.8: **Cavity drifts**: The stability of the cavity can be inferred by monitoring the transmission of a probe detuned by γ_c from cavity resonance. We measure the histogram of the transmitted powers which corresponds to a standard deviation of 0.35 MHz in cavity resonance frequency

In order to optimally stabilize the cavity, we look at the probe transmission when it is detuned by γ_c from resonance where it is most sensitive to fluctuations. We measured that the cavity lock frequency has a standard deviation of 0.35 MHz, less than 10 % of the full width at half maximum.

9.4 Cooperativity and EIT measurements

After the installation of the cavity, we were unable to trap the same number of atoms as we used to before opening the vacuum chamber. Given the specific configuration through which we load our atoms, it is not very straight forward to determine if the atoms are not loading in the LVIS trap or in the main trap. The only possible explanation after realigning all the MOT beams and adjusting the LVIS atomic flux was that we ran out of Rb atoms.

Installation of a new Rb dispenser

As Rubidium is highly reactive to water, we use a special technique to avoid any contact with atmospheric moisture. The Rb dispenser was developed in the SYRTE laboratory in Paris, and is available in glass cells in solid form with an approximate weight of 2 gms. The glass cell is placed inside a malleable tube and attached to the chamber via a flange. After the removal of the old Rb cell, the new dispenser is installed without breaking the glass cell. Once we pump the system down to $\sim 10^{-8}$ mbar, we squeeze the malleable tube using a special tool until we observe a spike in the pressure. After about a week of heating the dispenser at $50°C$, we managed to load the atoms in our MOT.

9.4.1 Cooperativity measurement

After the cavity mirrors were changed, the fundamental mode of the cavity no longer overlaps with the atomic cloud. In order to position the cavity mode onto the atomic cloud, we prepare a large cloud by increasing the atomic flow using a large B field gradient in the LVIS trap. We move the trap position by using the external magnetic field compensation coils. Once we see the normal mode splitting, we position the cloud more precisely using a smaller atomic cloud.

The cooperativity is measured using the same sequence as the previous chapter. We prepare the cloud using 40ms of MOT cycle but without any preparation cycle. The shape of the cloud in the current system is cigar shaped with a waist of 15 μm. The cavity transmission is measured with the probe detuning scanned around the resonance of the atoms. The cooperativity for the same number of atoms in the new cavity is enhanced by the increase in finesse i.e. 5.

9.4.2 EIT measurement

We avoid the Blue cavity to minimize the fluctuations in control field Rabi frequency. In order to couple to Rydberg states, we can either incident the blue beam along the cavity mode or we can also couple it perpendicular to the cavity axis. The main advantage of the former setup is to have the freedom to select the polarization of the blue beam which will allow us to select the magnetic sub-level to excite to in Rydberg D-states.

Since the Blue is coupled in the same path as the probe, we can no longer have the enhancement cavity. In its absence, the control field power near the atoms is lowered by a factor ≈ 15 if we use the same waist for the same incoming control field power. But its waist can be reduced by 3 times (from 90 μm to 30 μm) as the

cavity mode is only 15 μm. Effectively, the Rabi frequency will be at least 0.6 times the one with the cavity and can be easily higher since we can channel all the power to excite to only one specific sub-level.

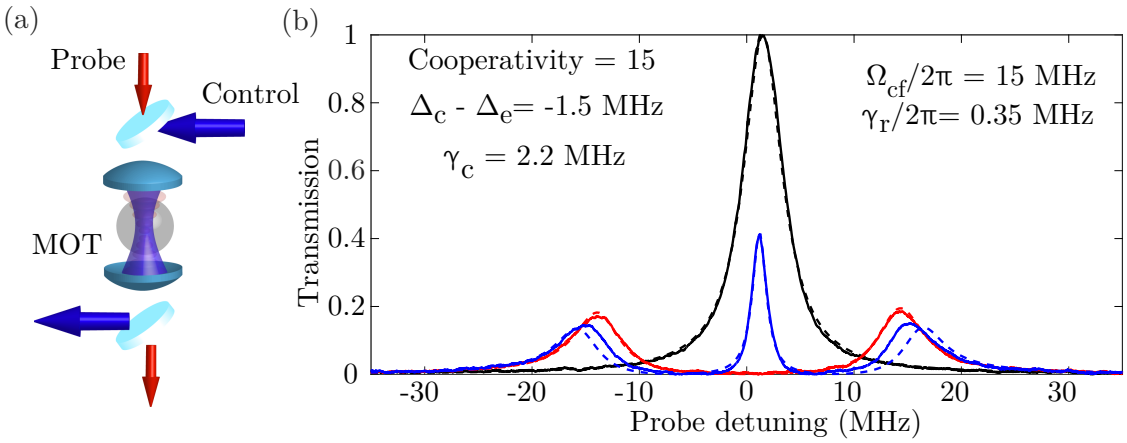

Figure 9.9: **Schematic representation of the setup** (a) The probe field is coupled into the cavity but the blue beam is transmitted by the mirrors since they are transparent at 480 nm. (b) **EIT measurement**: The black curve corresponds to empty cavity transmission line with a linewidth of 2.2 MHz. The red curve is the cavity transmission in the presence of atoms. The blue curve is the EIT with blue coupled along the probe mode.

We measure a control field Rabi frequency of $5\,\gamma_e$ for a power of 50 mW as shown in Figure 9.9. We should be able to achieve at least twice the current Rabi frequency by replacing the amplifier of the blue laser. From the above measurements we observed that indeed with the new setup, the control field is stronger than what we have estimated.

Increasing the MOT density

With the new narrow dipole trap, we are not able to efficiently load the atoms into a 15 μm trap. The most likely explanation is that we are limited by radiative losses due to the presence of repumper during the molasses which limits the loading efficiency. Currently, we are exploiting various schemes to make even larger atomic densities by using dark MOT cycle which enables us to achieve small samples with high density.

9.5 Possible schemes to exploit

After characterizing the non-linearity of the new atom-cavity system, there are many schemes that we can explore. One of our current goal is to be able to generate deterministically non-classical fields for quantum information processing tasks.

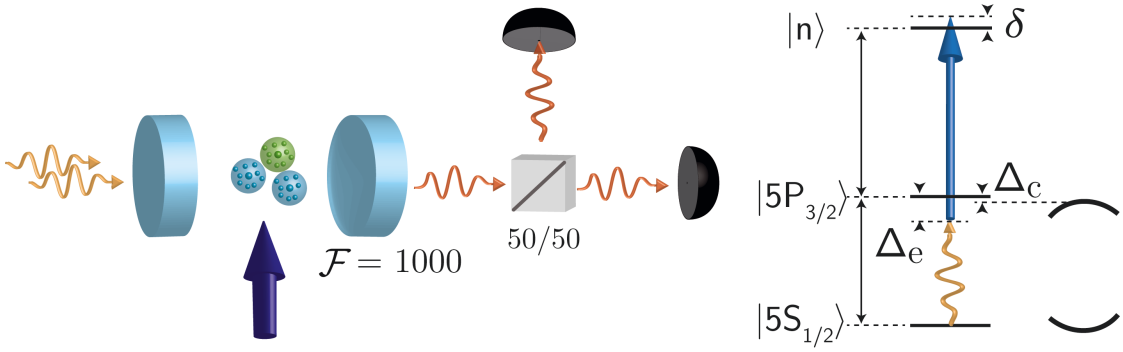

Figure 9.10: **Proposed excitation scheme in dispersive regime**: Atoms are excited to Rydberg states off-resonantly. In this scheme, the interactions divide the atomic cloud into "bubbles" which can at most have only one excitation. The green bubbles have a single excitation and the blue ones have none. These spheres act like two-level superatoms. The statistical properties of the transmitted probe light is measured using correlation measurement.

9.5.1 Off-resonant excitation

An interesting experiment that can be carried out with the new setup would be the theoretical scheme proposed in [46]. In this configuration the statistics of the transmitted light is measured when excited off-resonantly to an intermediate state but close to the resonance of the two photon transition. This approximation is only valid when the number of Rydberg excitations is much smaller than the number of atoms.

As the intermediate state is far-detuned, one can adiabatically eliminate the population and coherence term as it mostly stays unpopulated [115]. Effectively, the system behaves as two-level superatoms and using a slight two-photon detuning will allows us to observe dispersive effects. The strong Rydberg-Rydberg interactions divide the cloud into N_b spheres (with n_b atoms) where each one cannot have more than one Rydberg excitation [116, 117]. The number of atoms per bubble is given by Equation 3.6. Each bubble 'α' can either have no excitations ($|-_\alpha\rangle$), or one collective Rydberg excitation ($|+_\alpha\rangle$) (as shown in Figure 9.10). The interaction term is simplified to the following form

$$\hat{\mathcal{H}}_{int} = g_{eff} N_b (\hat{a}\hat{J}_+ + \hat{a}^\dagger \hat{J}_-), \tag{9.3}$$

where $g_{eff} = \frac{g\Omega_{cf}}{2\delta}$ and a collective spin lowering operator $\hat{J} = \sum_{\alpha=1}^{N_b} |-_\alpha\rangle\langle+_\alpha|$ corresponding to the spin 1/2 Rydberg bubbles introduced in [46]. The effective spin $\hat{J}$ interacts with the cavity mode $\hat{a}$ and evolves the system with an enhanced coupling factor $\sqrt{n_b}$. This is similar to the well known Tavis-Cummings model [118].

The correlation function of the transmitted light can be shown to be equal to that of the intracavity field [51]. The $g^{(2)}$ function is evaluated from the coupled spin-field evolution equations by assuming that, at maximum, only the N_b Rydberg excitation can survive in the medium.

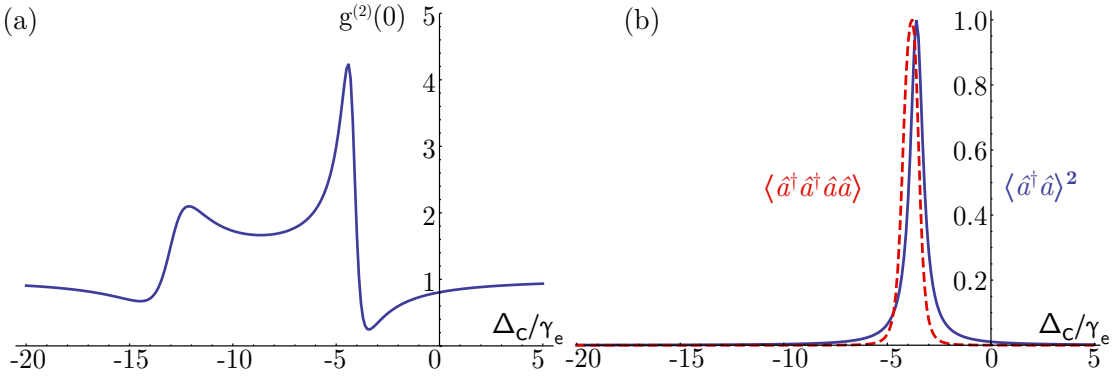

Figure 9.11: **The statistics of the transmitted light in off-resonant excitation scheme using a continuous probe**: (a) The auto correlation function of the transmitted light as a function of normalized cavity detuning. It exhibits strong bunching/anti-bunching features depending on the cavity detuning which favors either photon emission in pairs or one by one. (b) The average number of photons $\langle a^\dagger a\rangle^2$ (solid) and the average number of photon pairs $\langle a^\dagger a^\dagger aa\rangle^2$ in the transmitted light exhibit a different resonant frequency. The experimental parameters chosen are $\gamma_c = 0.3\,\gamma_e$, Rydberg level n = 95, C = 300, $\rho = 0.1$ atoms/μm^3, $\delta = 0.5\,\gamma_e$ and $\Delta_c = -16\,\gamma_e$.

Physical interpretation

The non-linearity arises from the coupling of the nonlinear spin operator to the cavity. The presence of a finite number of atoms in each blockade sphere breaks the harmonicity of the excitation space. The excitation to doubly-excited subspace is detuned by a parameter $\bar{\kappa}$ compared to the single excitation subspace. Hence one can tune the parameters to go on resonance with either one or the other, and therefore one can observe bunching or anti-bunching correlations in the transmitted light. The numerical simulations for the new cavity using perturbative approach does agree with this physical picture (see Figure 9.11). All these parameters are within the current experimental reach.

9.5.2 On-resonance excitation

Going to an all-resonant case will increase the non-linearity, but at the cost of large optical losses. The current 'low' finesse cavity will help us to circumvent this problem without resorting to the cavity QED regime.

9.5.3 Cavity phase shift

Using an optical resonator one can convert losses into phase shifts. To achieve that, an unbalanced cavity with one mirror reflection much higher than the other is required. By using a single ended cavity in reflection one can move between two extreme regimes by tuning the intracavity losses only by the transmission of the 'lossy mirror'. A possible implementation scheme is illustrated in in Figure

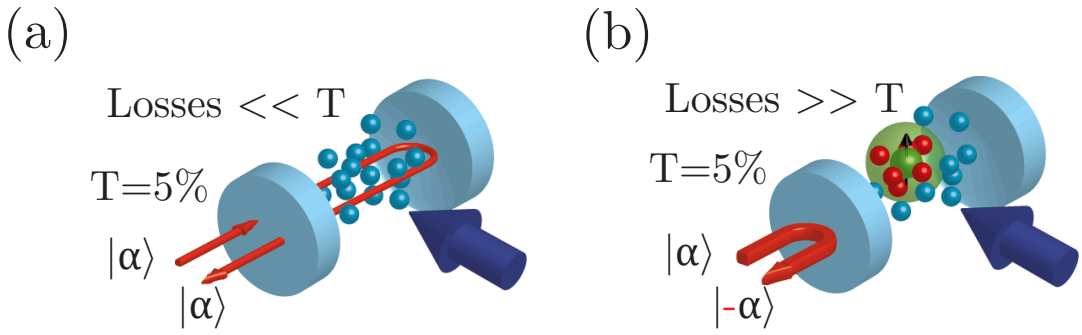

Figure 9.12: **Phase gate**: A possible scheme to implement a phase gate with a single Rydberg excitation. (a) The Reflected field acquires no phase shift when incident under EIT conditions (b) If a single Rydberg atom creates losses much higher than 0.5% then the reflected field acquires a phase shift with reasonable losses.

9.12. In the absence of intra-cavity losses the incident field on the 'lossy mirror' enters into the cavity and is reflected with the same phase. If the losses are much higher compared to the transmission of the mirror then 'almost' all the incident field acquires a phase π in reflection. We showed in Section 6.2.1 that our detection can be used to detect these phase shifts. The goal is to create strong enough losses by using a single Rydberg excitation in the atomic cloud.

Quantum scissors experiment

In the blockade model, we assume that in every Rydberg sphere there is only one excitation. In reality, there is a finite probability of exciting two Rydberg excitations which evolve with the interaction potential. If we consider an initial ground state of the N-atom system $|\phi_i\rangle = \sum_{n=1}^{N} |g_1, g_2 ....g_N\rangle$ evolving with

$$\hat{U} = \exp\left(-i \sum_{j<k}^{N} \frac{C_6}{R_{i,j}^6} \hat{\sigma}_{rr}^{(j)} \hat{\sigma}_{rr}^{(k)}\right) \tag{9.4}$$

each single excitation term evolves conservatively and only the terms with n>1 gets dephased due the interaction potential. In retrieval process, one can extract only the excitations phase matched with the initial state and hence the photonic component retrieved will be of the form [89, 119]

$$|a_{out}\rangle = \frac{|0\rangle + \alpha|1\rangle}{\sqrt{1+\alpha^2}} \tag{9.5}$$

where α is the amplitude of the input coherent state. In addition to the creation of non-gaussian states, it allows us to study Rydberg-Rydberg collisional physics. In free space systems, the photon packets get distorted by propagating via highly non-linear medium which renders them unusable for quantum operations but using the cavity systems can avoid this distortion.

9.6 Photonic controlled-phase gate proposal

In order to estimate the above effect more precisely, we use a pulsed scheme to implement the controlled phase gate. It is one of the universal gates and is a building blocks of quantum computation. One of the input qubits act as a control and imprints a phase of π on the other one depending on its incoming state.

As we have seen earlier, in free space locality and causality prevent us from achieving a perfect phase shift without destroying the purity of photons. We can overcome this by using a cavity scheme where one of the photon is stored in the cloud as a Rydberg excitation. The proposal and the calculations are performed in collaboration with Anders Sørensen's group [120].

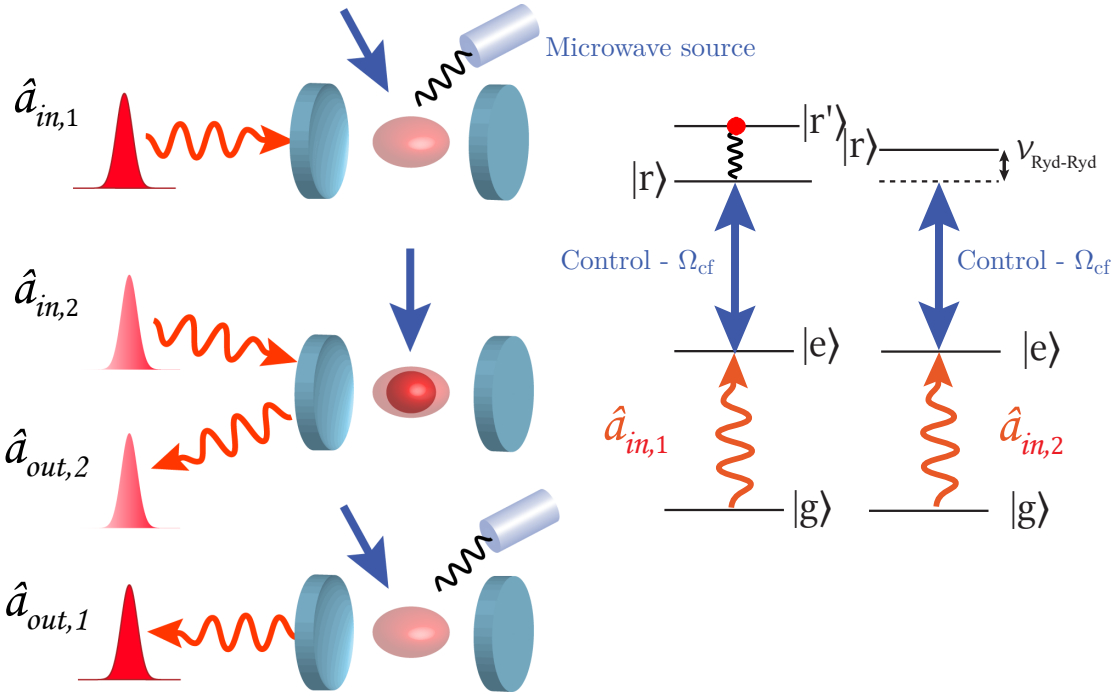

Figure 9.13: **Scheme for photonic phase gate**: A single photon stored as a Rydberg excitation acts a blockade for the second photon pulse and induces a phase shift of π on it. **On the right** The excitation scheme for the first photon and the second photon is illustrated. The first photon is stored in a different Rydberg state using microwave transition. The second photon can no longer be excited to Rydberg state $|r\rangle$ due to interaction potential $\mathcal{V}_{Ryd-Ryd}$.

Gate implementation

In a single-rail system, the information is encoded in the presence or absence of a photon. We denote a qubit with no photons in the pulse as $|0\rangle$, and with a single photon as $|1\rangle$. The first photon pulse ('control') is stored in the atomic cloud via EIT to a state $|r\rangle$ using a control field Ω_{cf}. This excitation is then transfered to another Rydberg state $|r'\rangle$. A second pulse ('target') is then incident onto the

cavity. If the cloud doesn't contain a Rydberg excitation ($|r'\rangle$), then the second pulse will be reflected with the same phase. Conversely, if there is a Rydberg atom then it will detune the state $|r\rangle$ out of resonance for the remaining atoms. In this case, the photon field entering the cavity is lost and the field reflected acquires a phase shift of π as shown in Figure 9.13.

In dual-rail systems, the information is encoded in the state of the photon rather than its presence. For eg: the logical states $|0\rangle$ and $|1\rangle$ can be encoded as two orthogonal polarizations of a single photon. As opposed to single rail implementation, the dual rail systems are conditioned by the detection of both photons.

Choi-Jamilowski Fidelity

To evaluate the performance of the gate operation, the Choi-Jamiolkowski fidelity has been calculated [121, 122]. The imperfections of storage/ retrieval process can be ignored as the fidelity is mainly affected by the target photon scattering. In free space, the Rydberg non-linearity is characterized by the optical depth per blockade d_b while in the cavity systems with a finesse ($\mathcal{F}$) the parameter characterizing the system is cooperativity per blockade $\mathcal{C}_b \sim \mathcal{F} d_b$.

The fidelity is estimated by evaluating how the real gate operation deviates from the ideal gate operation. The operation has no effect when the control pulse is in state $|0\rangle$. Hence the fidelity is affected in the presence of a single photon in the control pulse and it is estimated to be [73, 120] :

$$F_{cj} = |\langle \phi_{ideal} | \phi_{real} \rangle| = \frac{1}{16} \left| 3 - \frac{1 - 2\mathcal{C}_b}{1 + 2\mathcal{C}_b} \right|^2 \tag{9.6}$$

where $\mathcal{C}_b$ is the cooperativity per blockade. As we can see from the above equation, the fidelity approaches one for large C_b.

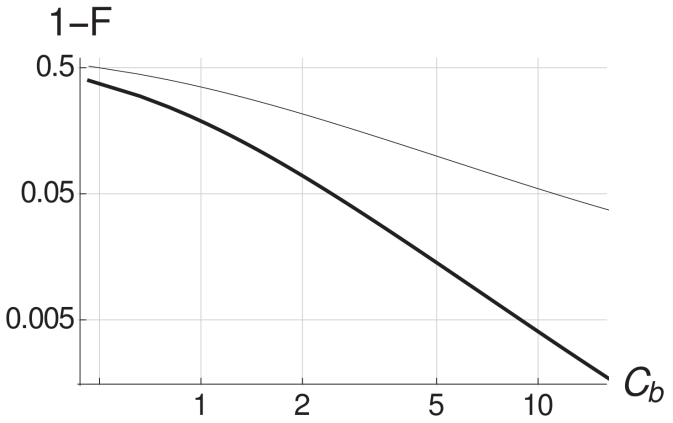

Figure 9.14: **Fidelity as a function of cooperativity per blockade**:

As the main source of error in single rail systems is photon scattering, the dual-rail implementation is less likely to fail. In Figure 9.14, we compare the fidelities of single rail and dual rail systems and we can observe that for a reasonable $\mathcal{C}_b$ of 10 one can achieve very high fidelities (post selected) greater than 0.99. In addition, for practical application the proposed gate has shown to improve the communication rate of quantum repeaters [120].

9.7 Conclusion

In this chapter we described our efforts to move to the quantum regime with the help of a new cavity. We showed how the designed resonator fulfills the necessary conditions to create strong optical non-linear effects. We also described its installation and the EIT measurements performed with this setup. Currently, we are in the process of characterizing the non-linearity of the system. Finally, we concluded the chapter with possible schemes we can exploit and a proposal for photonic phase gate.

General conclusion and outlook

In this manuscript, we studied classical optical non-linearities using dipole-dipole interactions between Rydberg atoms in a cavity. This work was motivated by the fact that Rydberg interactions in an atomic cloud have been theoretically proposed to be viable candidates for efficient manipulation of photons. We combined the advantages of EIT along with the interaction of Rydberg states, to enhance the optical non-linearity induced by a cold atomic system.

We demonstrated how one can prepare a small cold atomic ensemble, trapped from a relatively large cloud of 1 mm in diameter, using selective depumping and repumping cycles. By exciting the atoms resonantly to Rydberg states using EIT, we measured the effects of Rydberg-Rydberg interactions using both S and D states for n = 37-90. The resonant non-linear effects appeared as intensity dependent losses that increase as we move to high-lying Rydberg states. A semi-classical model was developed to explain the observed non-linear behavior arising from Rydberg-Rydberg interactions for S states. We also showed that we must move beyond the three level model to explain the non-linearity observed in Rydberg D states, where the collisional effects lead to the creation of long-lived excitations in the cloud.

The cooperativity per blockade sphere was enhanced by increasing the cavity finesse. This should, in principle, allow us to probe quantum optical non-linearities. Based on the EIT signal observed at n = 37, we are confident that the available coupling power will allow us to excite to atleast n= 90-100 Rydberg states.

As we move away from the coherent classical picture like the Rydberg bubble model, dephasing mechanisms give way to non-linear losses. A cavity can help us take advantage of these irreversibly lossy photonic channels. Following this idea, we described a theoretical proposal for a very high fidelity controlled photonic phase gate. This proposal allowed us to circumvent the Shapiro's limitation, where large Kerr non-linearities cannot be used for quantum optical communication [43]. Finally, we showed that cavities can be used in novel ways to modify the light at the quantum level, such as the creation of higher order correlations.

In addition, with the help of Andrey Grankin, we observed that we can use the Schwinger-Keldish formalism to evaluate the correlation effects beyond the lowest order. This allowed us to calculate the elastic and inelastic components of the squeezing spectrum up to any given order in feeding rate.

It has been shown that dissipative propagation through Rydberg EIT ensembles, like single photon filters or subtractors irreversibly distort the shape of optical photons [123]. Since such distortions will limit the fidelity of the operation, one

needs to characterize the purity of the manipulated photons. To achieve that, we use a powerful technique called optical homodyne tomography to measure more intricate details of the optical photons. We developed a setup which allows us to measure the Wigner function, phase dependent squeezing, etc., of light. We showed that our setup can be used to detect phase changes, by measuring the phase flips induced by a linear system. We also studied the squeezing spectrum of light along with the effects caused by the cavity and the EIT.

The experimental results and the theoretical ideas described in this thesis brings us one step closer to the quantum optical manipulation using cavity enhanced Rydberg-EIT systems. Moreover, the detection methods developed will help us study the manipulated photons more elaborately.

Outlook

Simple models, such as the perturbative approach and the bubble model, can be used to estimate the resonant classical non-linearity of Rydberg-EIT. Using the Schwinger-Keldish formalism, we observed that by evaluating the cavity transmission in third order, it reproduces the semi-classical non-linearity. Hence, we can use this formalism to calculate the non-linear effects observed beyond the semi-classical model by moving to higher orders.

The goal for the next few months is to investigate the resonant non-linearity of the current experimental setup, and study the non-linear evolution of few-photon excitations in the Rydberg-EIT cloud. In the long term, the objective is to create more exotic states such as "quantum fluids of light" [124]. This could be achieved by using the Rydberg-induced coupling between different but nearly-degenerate transverse modes of the cavity [125].

Part V

Appendices

Appendix A

Fundamental constants and Energy levels of ^{87}Rb

We list some fundamental constants and various properties of ^{87}Rb that complement this thesis. Most of this information can be found in the NIST website.

A.1 Fundamental constants

Vacuum permitivity	ε_0	$8.854{\cdot}10^{-12}$ As/Vm
Vacuum permeability	μ_0	$4\pi{\cdot}10^{-7}$ H/m
Speed of light	c	299 792 458 m/s
Planck's constant	$\hbar$	$1.054\ 571\ 8{\cdot}10^{-34}$ Js
Boltzmann's constant	k_B	$1.380\ 650\ 4{\cdot}10^{-23}$ J/K
Electron charge	e	$1.602\ 189{\cdot}10^{-19}$ C

Table A.1: **Selected fundamental constants**.

A.2 ^{87}Rubidium reference

We recall some constants we use in our calculations. A more detailed review of these constants can be found in [126]. We use only the D_2 for trapping and cooling of ^{87}Rb atoms. In Figure A.1 we show the full hyperfine levels with cross-over resonances. The MOT trapping light is locked using the crossover transition between $5P_{3/2}$ F = 1 and F = 3. It is then moved closer to resonance using a double pass AOM. The repumper beam is locked on the crossover transition between the $5P_{3/2}$ F = 1 and F = 3 and then shifted to on-resonance to repump atoms in $5\,S_{1/2}$ F = 2 by a single pass AOM.

Atomic number	Z	37
Mass	m	$1.443{\cdot}10^{-24}$ kg
Melting point	T_m	39.30 ° C
D_2 line	$5S_{1/2} \rightarrow 5P_{3/2}$	780.033 330(23) nm
Natural lifetime	τ	26.24 ns
Natural Linewidth	$\gamma_e = \Gamma_e/2$	$2\pi \cdot 3.033$ MHz
Saturation Intensity	$I_{sat} = \pi hc\Gamma/3\lambda_0^3$	1.67 mW/cm^2
Doppler Temperature	T_d	145.57 μK

Table A.2: **Properties of ^{87}Rb atoms**.

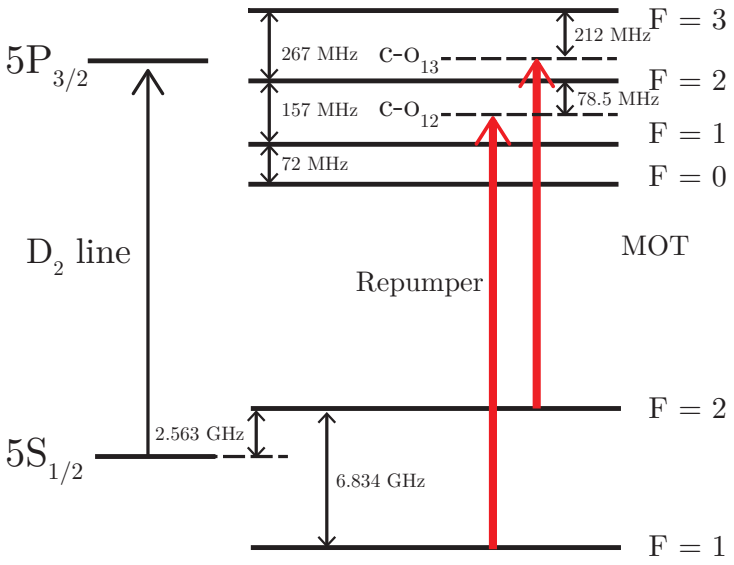

Figure A.1: **Hyperfine structure of D_2 transition**: The locking points of saturated absorption of MOT and Repumper lasers along with the crossover resonances are shown.

Appendix B

Rydberg atoms

In this appendix we will briefly recall the properties of Rydberg atoms and their interaction strengths. Rydberg electrons are so far from the nucleus they are extremely sensitive to weak fields. We are going to look at the properties of Rydberg states in alkali atoms, where only one valence electron is excited to high principle quantum numbers.

Due to the shielding effect of the non-valence electrons in an alkali atom, it acts like a Hydrogen atom and hence referred to as Hydrogenoid atom. Unlike the Hydrogen atom, where there are no other electrons in inner orbitals, Rydberg states are affected by the presence of non-valence electrons. This effect is very prominent in low orbital angular momentum states (l), where the electron orbits very close to the nucleus. These Hydrogenoid atoms can be accurately described by the quantum defect theory [70], especially for the low angular momentum levels ($l \leq 3$). The physical properties of Rydberg atoms can be described by a formula similar to the one of the Hydrogen atom, with an effective principal quantum number $n^* = n - \delta_{n,l,j}$ where $\delta_{n,l,j}$ is referred to as quantum defect.

The energy of any Rydberg level can then be evaluated using

$$E_{n,l,j} = -\frac{R_y(1+\frac{m_e}{m_c})}{(n^*)^2} \tag{B.1}$$

where $R_y = 13.6\text{eV}$ is the Rydberg constant.

Atomic property	n^* scaling	For n = 80
Binding energy	$1/n^{*2}$	$E_{n,l,j} = -0.5\,\text{THz}$
Energy separation neighbouring levels	$1/n^{*3}$	$\Delta E_n = 13\,\text{THz}$
Radius/Dipole moment	n^{*2}	r = 0.3 $\mu\text{m}/\mu_0 \approx 10^4 e a_0$
Radiative lifetime	n^{*3}	$\tau \approx 500\,\mu s$
Polarizability	n^{*7}	$\alpha \approx 10^4\,GHz/(V/cm)^2$

Table B.1: **Properties of Rydberg atoms**: Scaling of various properties of Rydberg atoms and their typical values for n=80 in ^{87}Rb atoms.

Appendix C

Calculation of Stark shifts for D states

In this appendix, we will describe how to calculate the Stark structure of alkali atoms. As the principal quantum number increases, the electron moves away from the nucleus and the coupling to external electric field increases. The excitation to D states involves a large number of Zeeman sublevels, which are highly sensitive to the electric field especially at high principal quantum numbers. Therefore, the atomic level structure is perturbed by the presence of even weak electric fields [127].

We assume that the electric field is in the direction of the quantization axis $\vec{z}$. The electron experiences an additional force due to the external field $\vec{F}$ along with the Coulomb potential of the extra proton in the nucleus. The additional Hamiltonian term can be expressed as

$$\hat{\mathcal{H}}_{stark} = eF\hat{z} \tag{C.1}$$

The electric field creates an additional off diagonal coupling between different states of same m_j, and new energy levels are calculated by diagonalizing the total Hamiltonian. The matrix of the Stark interaction can be calculated from the following expression in the atomic basis $|n, l, j, m_j\rangle$ [94]

$$\begin{aligned}\langle n, l, j, m_j|\hat{\mathcal{H}}_{stark}|n', l', j', m_j'\rangle \\ = \delta_{m_j, m_j'}\delta_{l,l'\pm1}F\langle n, l, j|\hat{r}|n', l', j'\rangle\langle l, j, m_j|\cos\theta|l', j', m_j'\rangle\end{aligned} \tag{C.2}$$

Here we consider the selection rules to select only the levels which are coupled by the electric field.

For weak fields, the Stark splitting for non-hydrogenic states ($l \leq 3$) can be calculated using a perturbative expansion and the shift can be calculated using

$$\Delta E = \frac{1}{2}\alpha F^2 \tag{C.3}$$

where α is the static polarizability of the energy level and is calculated using

$$\alpha = \sum_{n,l,j \neq n',l',j'} -2F \times \frac{|\langle n, l, j, m_j|\vec{z}|n', l', j', m_j\rangle|^2}{E_{n,l,j} - E_{n',l',j'}} \tag{C.4}$$

The radial term in the numerator scales as $(n^*)^2$ and the energy difference between the neighboring energy levels scales as $(n^*)^{-3}$. The polarizability term scales as $(n^*)^7$, hence the Rybderg states especially the high lying ones, are extremely sensitive to weak fields.

To estimate the shifts more precisely, its necessary to diagonlize the total Hamiltonian. We consider the atomic basis which includes all the neighboring states with a given $|m_j|$. For each manifold $|m_j|$ we truncate the atomic basis with $\Delta n = 5$.

$$\mathcal{H}_{tot} = \begin{bmatrix} E_1 & 0 & ... & 0 \\ 0 & E_2 & ... & 0 \\ & & \vdots & \\ 0 & 0 & .... & E_n \end{bmatrix} + F \begin{bmatrix} 0 & \langle 1|z|2\rangle & \langle 1|z|3\rangle & ... & \langle 1|z|n\rangle \\ \langle 2|z|1\rangle & 0 & \langle 2|z|3\rangle & ... & \langle 2|z|n\rangle \\ & & \vdots & & \\ \langle n|z|1\rangle & \langle n|z|2\rangle & \langle n|z|3\rangle & .... & 0 \end{bmatrix} \tag{C.5}$$

All the radial components are calculated using the Numerov algorithm [127]. We show the stark map of Rydberg 85 D state along with the neighboring levels in Figure C.1.

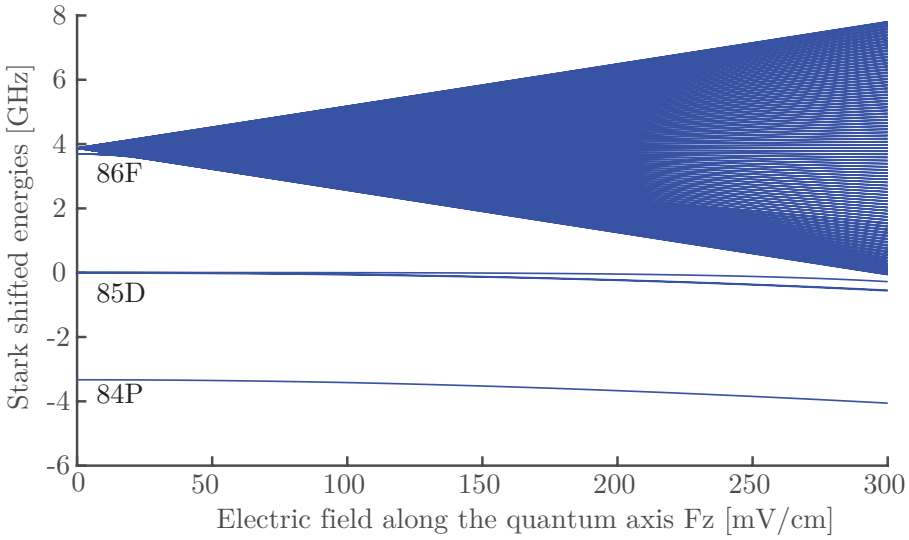

Figure C.1: **Stark map of 85D state**: The splitting of energy states of the 85 D, 86 F, 84 P is shown with electric field.

Appendix D

Wigner Function

The $g^{(2)}$ measurement is inherently insensitive to phase fluctuations inside a quantum state, hence it doesn't give full information about the state. The quantum state of light can be fully described by using a density matrix. Usually, this density matrix is written in a Fock state basis, where each state is an eigenstate of the number operator ($\hat{N} = \hat{a}^\dagger \hat{a}$). One can also describe it in the optical phase space using quadratures of quantized electric field ($\hat{q} = \sqrt{\frac{\hbar}{2\omega}}(\hat{a} + \hat{a}^\dagger)$ and $\hat{p} = i\sqrt{\frac{\hbar\omega}{2}}(\hat{a} - \hat{a}^\dagger)$).

Each point in the phase space corresponds to one set of quadratures. The quasi-probability density function in phase space is known as the Wigner function. It is quasi because quadrature variables don't commute and we cannot measure both of them precisely at the same time. The Wigner function is defined as

$$W(q,p) = \frac{1}{2\pi}\int_{-\infty}^{\infty} \langle q - x|\hat{\rho}|q + x\rangle e^{-ipx/\hbar} dx \tag{D.1}$$

By measuring the Wigner function one can reconstruct the full density matrix.

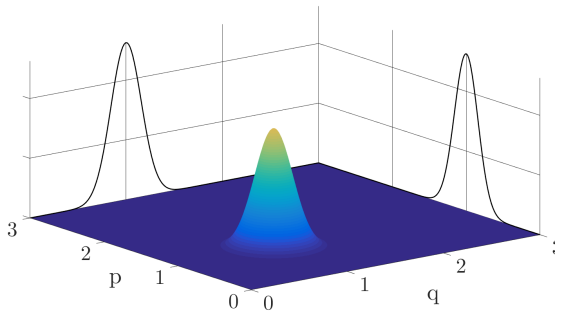

Figure D.1: **The Wigner function of a coherent state along with its projection on the orthogonal quadrature planes**.

Experimentally it is not possible to measure the function directly but it is possible to measure its projection along any particular direction. If we project the Wigner function onto one of the quadrature planes, then we obtain the probability distribution corresponding to that quadrature. The projected function can be represented as

$$\int W(q,p)dp = \Pr(q) \tag{D.2}$$

The coherent states have gaussian Wigner functions with positive values across the phase space whereas the non-classical or quantum states are those states whose Wigner function can go below zero for certain quadrature values, for example pure Fock states with n>0 as shown in Figure D.2.

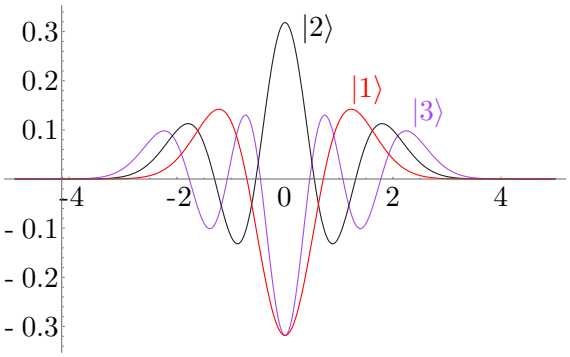

Figure D.2: **Cross section of a Wigner function of pure Fock states**: The Wigner function of Fock states - single photon $|1\rangle$, two photon $|2\rangle$ and three photon $|3\rangle$ states when one of the quadratures is zero.

The coherent and Fock states have circularly symmetric Wigner functions, i.e. they are phase invariant. Conversely, squeezed states can have lower noise than vacuum fluctuations for certain quadrature phase ($\hat{q}_\theta = \hat{q}\cos\theta + \hat{p}\sin\theta$) and at the same time, the noise in the orthogonal phase goes up without violating the Heisenberg uncertainity principle ($\Delta\hat{q}_\theta.\Delta\hat{q}_{\theta+\pi/2} \geq \hbar/2$). This makes the squeezed states extremely useful for precision measurements in quantum metrology.

Bibliography

[1] Moore G E *Cramming more components onto integrated circuits (Reprinted from Electronics, pg 114-117, April 19, 1965)* Tech. Rep. 1 IEEE (1965).

[2] Waldrop M M *The chips are down for Moore's law* Nature News **530** 144 (2016).

[3] Feynman R P *Simulating physics with computers* International Journal of Theoretical Physics **21** 467–488 (1982).

[4] Shor P W Algorithms for quantum computation: discrete logarithms and factoring Proceedings 35th Annual Symposium on Foundations of Computer Science pp 124–134 (1994).

[5] Bressoud D M and Wagon S A course in computational number theory (Wiley) (2008).

[6] Nielsen M A and Chuang I L Quantum Computation and Quantum Information (Cambridge University Press) (2011).

[7] Ourjoumtsev A, Jeong H, Tualle-Brouri R and Grangier P *Generation of optical 'Schrodinger cats' from photon number states* Nature **448** 784–786 (2007).

[8] Vlastakis B, Kirchmair G, Leghtas Z, Nigg S E, Frunzio L, Girvin S M, Mirrahimi M, Devoret M H and Schoelkopf R J *Deterministically Encoding Quantum Information Using 100-Photon Schrödinger Cat States* Science **342** 607–610 (2013).

[9] Raimond J M, Brune M and Haroche S *Manipulating quantum entanglement with atoms and photons in a cavity* Rev. Mod. Phys. **73**(3) 565–582 (2001).

[10] Haroche S and Raimond J M Exploring the Quantum: Atoms, Cavities, and Photons (Oxford University Press) (2006).

[11] Moehring D L, Madsen M J, Younge K C, R N Kohn J, Maunz P, Duan L M, Monroe C and Blinov B B *Quantum networking with photons and trapped atoms (Invited)* J. Opt. Soc. Am. B **24** 300–315 (2007).

[12] Monroe C, Raussendorf R, Ruthven A, Brown K R, Maunz P, Duan L M and Kim J *Large-scale modular quantum-computer architecture with atomic memory and photonic interconnects* Phys. Rev. A **89**(2) 022317 (2014).

[13] Monroe C R, Schoelkopf R J and Lukin M D *Quantum Connections* Scientific American **314** 50–57 (2016).

[14] Caulfi H J and Dolev S *Why future supercomputing requires optics* Nature **4** 261–263 (2010).

[15] Lvovsky A I and Raymer M G *Continuous-variable optical quantum-state tomography* Reviews of Modern Physics **81** 299–332 (2009).

[16] Leonhardt U *Quantum-state tomography and discrete Wigner function* Phys. Rev. Lett. **74** 4101–4105 (1995).

[17] Song G Z, Wu F Z, Zhang M and Yang G J *Heralded quantum repeater based on the scattering of photons off single emitters using parametric down-conversion source.* Scientific reports **6** 28744 (2016).

[18] Sangouard N, Simon C, de Riedmatten H and Gisin N *Quantum repeaters based on atomic ensembles and linear optics* Rev. Mod. Phys. **83**(1) 33–80 (2011).

[19] DiVincenzo D P *Two-bit gates are universal for quantum computation* Phys. Rev. A **51**(2) 1015–1022 (1995).

[20] Knill E, Laflamme R and Milburn G J *A scheme for efficient quantum computation with linear optics* Nature **409** 46–52 (2001).

[21] Adami C and Cerf N J "Quantum Computation with Linear Optics" Lecture Notes in Computer Science (LNCS) (Berlin, Heidelberg: Springer Berlin Heidelberg) pp 391–401 (1999).

[22] Lukin M D and Imamoğlu A *Nonlinear Optics and Quantum Entanglement of Ultraslow Single Photons* Phys. Rev. Lett. **84**(7) 1419–1422 (2000).

[23] Lukin M D *Colloquium : Trapping and manipulating photon states in atomic ensembles* Rev. Mod. Phys. **75**(2) 457–472 (2003).

[24] Pritchard J D, Weatherill K J and Adams C S Nonlinear optics using cold Rydberg atoms Annual Review of Cold Atoms and Molecules (World Scientific) chap 8, pp 301–350 (2012).

[25] Häffner H, Roos C and Blatt R *Quantum computing with trapped ions* Physics Reports **469** 155 – 203 (2008).

[26] Jaksch, Cirac, Zoller, Rolston, Cote and Lukin *Fast quantum gates for neutral atoms* Phys. Rev. Lett. **85** 2208–11 (2000).

[27] Bloch I *Ultracold quantum gases in optical lattices* Nature Physics **1** 23–30 (2005).

[28] Dicke R H *Coherence in Spontaneous Radiation Processes* Phys. Rev. **93**(1) 99–110 (1954).

[29] Duan L M and Kimble H J *Scalable Photonic Quantum Computation through Cavity-Assisted Interactions* Phys. Rev. Lett. **92**(12) 127902 (2004).

[30] Harris S E, Field J E and Imamoglu A *Nonlinear optical processes using electromagnetically induced transparency* Phys. Rev. Lett. **64** 1107–1110 (1990).

[31] Schmidt H and Imamoglu A *Giant Kerr nonlinearities obtained by electromagnetically induced transparency* Opt. Lett. **21** 1936–1938 (1996).

[32] Heinze G, Hubrich C and Halfmann T *Stopped Light and Image Storage by Electromagnetically Induced Transparency up to the Regime of One Minute* Phys. Rev. Lett. **111**(3) 033601 (2013).

[33] Friedler I, Petrosyan D, Fleischhauer M and Kurizki G *Long-range interactions and entanglement of slow single-photon pulses* Phys. Rev. A **72**(4) 043803 (2005).

[34] Weimer H, Müller M, Lesanovsky I, Zoller P and Büchler H P *A Rydberg quantum simulator* Nature Physics **6** 382–388 (2010).

[35] Pritchard J D, Gauguet A, Weatherill K J and Adams C S *Optical nonlinearity in a dynamical Rydberg gas* J. Phys. B: At. Mol. Opt. Phys. **44** 184019 (2011).

[36] Dudin Y O and Kuzmich A *Strongly Interacting Rydberg Excitations of a Cold Atomic Gas* Science **336** 887–889 (2012).

[37] Peyronel T, Firstenberg O, Liang Q Y, Hofferberth S, Gorshkov A V, Pohl T, Lukin M D and Vuletić V *Quantum nonlinear optics with single photons enabled by strongly interacting atoms* Nature **488** 57–60 (2012).

[38] Firstenberg O, Peyronel T, Liang Q Y, Gorshkov A V, Lukin M D and Vuletić V *Attractive photons in a quantum nonlinear medium* Nature **502** 71–75 (2013).

[39] Baur S, Tiarks D, Rempe G and Dürr S *Single-Photon Switch Based on Rydberg Blockade* Phys. Rev. Lett. **112**(7) 073901 (2014).

[40] Tiarks D, Baur S, Schneider K, Dürr S and Rempe G *Single-Photon Transistor Using a Förster Resonance* Phys. Rev. Lett. **113** 053602 (2014).

[41] Gorniaczyk H, Tresp C, Schmidt J, Fedder H and Hofferberth S *Single-Photon Transistor Mediated by Interstate Rydberg Interactions* Phys. Rev. Lett. **113**(5) 053601 (2014).

[42] Gorniaczyk H, Tresp C, Bienias P, Paris-Mandoki A, Li W, Mirgorodskiy I, Büchler H P, Lesanovsky I and Hofferberth S *Enhancement of Rydberg-mediated single-photon nonlinearities by electrically tuned Förster Resonances* Nature Communications **7** 12480 (2016).

[43] Shapiro J H *Single-photon Kerr nonlinearities do not help quantum computation* Phys. Rev. A **73** 062305 (2006).

[44] Gea-Banacloche J *Impossibility of large phase shifts via the giant Kerr effect with single-photon wave packets* Phys. Rev. A **81** 043823 (2010).

[45] Distante E, Padrón-Brito A, Cristiani M, Paredes-Barato D and de Riedmatten H *Storage Enhanced Nonlinearities in a Cold Atomic Rydberg Ensemble* Phys. Rev. Lett. **117** 113001 (2016).

[46] Grankin A, Brion E, Bimbard E, Boddeda R, Usmani I, Ourjoumtsev A and Grangier P *Quantum statistics of light transmitted through an intracavity EIT Rydberg medium* New Journal of Physics **16** 1–15 (2014).

[47] Grankin A, Brion E, Bimbard E, Boddeda R, Usmani I, Ourjoumtsev A and Grangier P *Quantum-optical nonlinearities induced by Rydberg-Rydberg interactions: A perturbative approach* Phys. Rev. A **92**(4) 043841 (2015).

[48] Parigi V, Bimbard E, Stanojevic J, Hilliard A J, Nogrette F, Tualle-Brouri R, Ourjoumtsev A and Grangier P *Observation and Measurement of Interaction-Induced Dispersive Optical Nonlinearities in an Ensemble of Cold Rydberg Atoms* Phys. Rev. Lett. **109** 233602 (2012).

[49] Boyd R W "Quantum-Mechanical Theory of the Nonlinear Optical Susceptibility" Nonlinear Optics (Elsevier) chap 3, pp 135–206 (2008).

[50] Puri R R The Electromagnetic Field Mathematical Methods of Quantum Optics (Berlin, Heidelberg: Springer Berlin Heidelberg) pp 119–136 (2001).

[51] Walls D and Milburn G J Quantum Optics Walls and Milburn (Berlin, Heidelberg: Springer Berlin Heidelberg) (2008).

[52] Keaveney J *Collective Atom - Light Interactions in Dense Atomic Vapours* Ph.D. thesis Durham University (2014).

[53] Saleh B E A and Teich M C Photon Optics Fundamentals of Photonics (John Wiley & Sons, Inc.) pp 384–422 (2001).

[54] Szöke A, Daneu V, Goldhar J and Kurnit N A *Bistable optical element and it's applications* Applied Physics Letters **15** 376–379 (1969).

[55] Gibbs H M, McCall S L and Venkatesan T N C *Differential Gain and Bistability Using a Sodium-Filled Fabry-Perot Interferometer* Phys. Rev. Lett. **36**(19) 1135–1138 (1976).

[56] Rosenberger A T, Orozco L A and Kimble H J *Observation of absorptive bistability with two-level atoms in a ring cavity* Phys. Rev. A **28**(4) 2569–2572 (1983).

[57] Lugiato L A Theory of Optical Bistability (Progress in Optics vol 21) ed Wolf E (Elsevier) pp 69 – 216 (1984).

[58] Rosenberger A T, Orozco L A, Kimble H J and Drummond P D *Absorptive optical bistability in two-state atoms* Phys. Rev. A **43** 6284 (1991).

[59] Fleischhauer M, Imamoglu A and Marangos J P *Electromagnetically induced transparency: Optics in coherent media* Rev. Mod. Phys. **77**(2) 633–673 (2005).

[60] Gea-Banacloche J, Li Y q, Jin S z and Xiao M *Electromagnetically induced transparency in ladder-type inhomogeneously broadened media: Theory and experiment* Phys. Rev. A **51**(1) 576–584 (1995).

[61] Hau L V, Harris S E, Dutton Z and Behroozi C H *Light speed reduction to 17 metres per second in an ultracold atomic gas* Nature **397** 594–598 (1999).

[62] Harshawardhan W and Agarwal G S *Controlling optical bistability using electromagnetic-field-induced transparency and quantum interferences* Phys. Rev. A **53**(3) 1812–1817 (1996).

[63] Wang H, Goorskey D and Xiao M *Controlling light by light with three-level atoms inside an optical cavity* Opt. Lett. **27** 1354–1356 (2002).

[64] Wang H, Goorskey D and Xiao M *Enhanced Kerr Nonlinearity via Atomic Coherence in a Three-Level Atomic System* Phys. Rev. Lett. **87**(7) 073601 (2001).

[65] Boller K J, Imamoğlu A and Harris S E *Observation of electromagnetically induced transparency* Phys. Rev. Lett. **66**(20) 2593–2596 (1991).

[66] Zibrov A S, Lukin M D, Nikonov D E, Hollberg L, Scully M O, Velichansky V L and Robinson H G *Experimental demonstration of laser oscillation without population inversion via quantum interference in Rb* Phys. Rev. Lett. **75** 1499–1502 (1995).

[67] Gheri K M, Walls D F and Marte M A *Quantum noise reduction close to an optically bistable dark resonance* Phys. Rev. A **50**(2) 1871–1876 (1994).

[68] Sautenkov V A, Rostovtsev Y V and Scully M O *Switching between photon-photon correlations and Raman anticorrelations in a coherently prepared Rb vapor* Phys. Rev. A **72** 065801 (2005).

[69] Alzar C L G, Cruz L S, Gómez J G A, Santos M F and Nussenzveig P *Super-Poissonian intensity fluctuations and correlations between pump and probe fields in Electromagnetically Induced Transparency* EPL (Europhysics Letters) **61** 485 (2003).

[70] Gallagher T F Rydberg Atoms (Cambridge University Press) cambridge Books Online (1994).

[71] Comparat D and Pillet P *Dipole blockade in a cold Rydberg atomic sample* Journal of the Optical Society of America B **27** A208 (2010).

[72] Lukin M D, Fleischhauer M, Cote R, Duan L M, Jaksch D, Cirac J I and Zoller P *Dipole Blockade and Quantum Information Processing in Mesoscopic Atomic Ensembles* Phys. Rev. Lett. **87** 37901 (2001).

[73] Grankin A *Theoretical studies of optical non-linear effects in ultracold Rydberg gases* Ph.D. thesis University of Paris-saclay (2016).

[74] Tong D, Farooqi S M, Stanojevic J, Krishnan S, Zhang Y P, Côté R, Eyler E E and Gould P L *Local Blockade of Rydberg Excitation in an Ultracold Gas* Phys. Rev. Lett. **93**(6) 063001 (2004).

[75] Weimer H, Löw R, Pfau T and Büchler H P *Quantum Critical Behavior in Strongly Interacting Rydberg Gases* Phys. Rev. Lett. **101** 250601 (2008).

[76] Tresp C, Bienias P, Weber S, Gorniaczyk H, Mirgorodskiy I, Büchler H P and Hofferberth S *Dipolar Dephasing of Rydberg D-State Polaritons* Phys. Rev. Lett. **115**(8) 083602 (2015).

[77] Liebisch T C, Reinhard A, Berman P R and Raithel G *Atom Counting Statistics in Ensembles of Interacting Rydberg Atoms* Phys. Rev. Lett. **95**(25) 253002 (2005).

[78] Bimbard E *Production and interaction of photons using atomic polaritons and Rydberg interactions* Ph.D. thesis Institut d'Optique Graduate School (2014).

[79] Hankin A M, Jau Y Y, Parazzoli L P, Chou C W, Armstrong D J, Landahl A J and Biedermann G W *Two-atom Rydberg blockade using direct 6S to nP excitation* Phys. Rev. A **89**(3) 033416 (2014).

[80] Ludlow A D, Huang X, Notcutt M, Zanon-Willette T, Foreman S M, Boyd M M, Blatt S and Ye J *Compact, thermal-noise-limited optical cavity for diode laser stabilization at 1×10−15* Opt. Lett. **32** 641–643 (2007).

[81] Burghardt B, Jitschin W and Meisel G *Precise rf tuning for cw dye lasers* Applied physics **20** 141–146 (1979).

[82] Kübler H, Shaffer J P, Baluktsian T, Löw R and Pfau T *Coherent excitation of Rydberg atoms in micrometre-sized atomic vapour cells* Nature Photonics **4** 112–116 (2010).

[83] Raab E L, Prentiss M, Cable A, Chu S and Pritchard D E *Trapping of Neutral Sodium Atoms with Radiation Pressure* Phys. Rev. Lett. **59**(23) 2631–2634 (1987).

[84] Pritchard D E, Raab E L, Bagnato V, Wieman C E and Watts R N *Light Traps Using Spontaneous Forces* Phys. Rev. Lett. **57**(3) 310–313 (1986).

[85] Lu Z T, Corwin K L, Renn M J, Anderson M H, Cornell E A and Wieman C E *Low-Velocity Intense Source of Atoms from a Magneto-optical Trap* Phys. Rev. Lett. **77**(16) 3331–3334 (1996).

[86] Dalibard J and Cohen-Tannoudji C *Laser cooling below the Doppler limit by polarization gradients: simple theoretical models* J. Opt. Soc. Am. B **6** 2023–2045 (1989).

[87] Lett P D, Watts R N, Westbrook C I, Phillips W D, Gould P L and Metcalf H J *Observation of Atoms Laser Cooled below the Doppler Limit* Phys. Rev. Lett. **61**(2) 169–172 (1988).

[88] Ketterle W, Davis K B, Joffe M A, Martin A and Pritchard D E *High densities of cold atoms in a dark spontaneous-force optical trap* Phys. Rev. Lett. **70**(15) 2253–2256 (1993).

[89] Stanojevic J, Parigi V, Bimbard E, Ourjoumtsev A, Pillet P and Grangier P *Generating non-Gaussian states using collisions between Rydberg polaritons* Phys. Rev. A **86** 1–5 (2012).

[90] Kimble H J, Dagenais M and Mandel L *Photon Antibunching in Resonance Fluorescence* Phys. Rev. Lett. **39**(11) 691–695 (1977).

[91] Brown R H and Twiss R Q *Correlation between Photons in two Coherent Beams of Light* Nature **177** 27–29 (1956).

[92] Sperling J, Vogel W and Agarwal G S *True photocounting statistics of multiple on-off detectors* Phys. Rev. A **85**(2) 023820 (2012).

[93] Bimbard E, Boddeda R, Vitrant N, Grankin A, Parigi V, Stanojevic J, Ourjoumtsev A and Grangier P *Homodyne Tomography of a Single Photon Retrieved on Demand from a Cavity-Enhanced Cold Atom Memory* Phys. Rev. Lett. **112**(3) 033601 (2014).

[94] Pritchard J D *Cooperative Optical Non-linearity in a blockaded Rydberg Ensemble* Ph.D. thesis Durham University (2011).

[95] Maxwell D, Szwer D J, Paredes-Barato D, Busche H, Pritchard J D, Gauguet A, Weatherill K J, Jones M P A and Adams C S *Storage and Control of Optical Photons Using Rydberg Polaritons* Phys. Rev. Lett. **110**(10) 103001 (2013).

[96] Stanojevic J, Parigi V, Bimbard E, Ourjoumtsev A and Grangier P *Dispersive optical nonlinearities in a Rydberg electromagnetically-induced-transparency medium* Phys. Rev. A **88**(5) 053845 (2013).

[97] Sevincli S, Henkel N, Ates C and Pohl T *Nonlocal Nonlinear Optics in Cold Rydberg Gases* Phys. Rev. Lett. **107**(15) 153001 (2011).

[98] Drever R W P, Hall J L, Kowalski F V, Hough J, Ford G M, Munley A J and Ward H *Laser phase and frequency stabilization using an optical resonator* Applied Physics B **31** 97–105 (1983).

[99] Grimm R, Weidemüller M and Ovchinnikov Y B Optical Dipole Traps for Neutral Atoms (Advances In Atomic, Molecular, and Optical Physics vol 42) ed Bederson B and Walther H (Academic Press) pp 95 – 170 (2000).

[100] Kuppens S J M, Corwin K L, Miller K W, Chupp T E and Wieman C E *Loading an optical dipole trap* Phys. Rev. A **62** 1–13 (2000).

[101] Hansch T and Couillaud B *Laser frequency stabilization by polarization spectroscopy of a reflecting reference cavity* Optics Communications **35** 441 – 444 (1980).

[102] Mücke M, Figueroa E, Bochmann J, Hahn C, Murr K, Ritter S, Villas-Boas C J and Rempe G *Electromagnetically induced transparency with single atoms in a cavity* Nature **465** 755–758 (2010).

[103] Albert M, Dantan A A and Drewsen M *Cavity electromagnetically induced transparency and all-optical switching using ion Coulomb crystals* Nature Photonics **5** 633–636 (2011).

[104] Ningyuan J, Georgakopoulos A, Ryou A, Schine N, Sommer A and Simon J *Observation and characterization of cavity Rydberg polaritons* Phys. Rev. A **93**(4) 041802 (2016).

[105] Singer K, Stanojevic J, Weidemüller M and Côté R *Long-range interactions between alkali Rydberg atom pairs correlated to the ns-ns,np-np and nd-nd asymptotes* J. Phys. B: At. Mol. Opt. Phys. **38** S295 (2005).

[106] Neukammer J, Rinneberg H, Vietzke K, König A, Hieronymus H, Kohl M, Grabka H J and Wunner G *Spectroscopy of Rydberg Atoms at $n \approx 500$: Observation of Quasi-Landau Resonances in Low Magnetic Fields* Phys. Rev. Lett. **59**(26) 2947–2950 (1987).

[107] Holloway C L, Gordon J A, Jefferts S, Schwarzkopf A, Anderson D A, Miller S A, Thaicharoen N and Raithel G *Broadband Rydberg Atom-Based Electric-Field Probe for SI-Traceable, Self-Calibrated Measurements* IEEE Transactions on Antennas and Propagation **62** 6169–6182 (2014).

[108] Beguin L *"Measurement of the van der Waals interaction between Rydberg atoms"* Ph.D. thesis Université Paris-Sud (2013).

[109] Saffman M, Walker T G and Mølmer K *Quantum information with Rydberg atoms* Rev. Mod. Phys. **82**(3) 2313–2363 (2010).

[110] Barredo D, Ravets S, Labuhn H, Béguin L, Vernier A, Nogrette F, Lahaye T and Browaeys A *Demonstration of a Strong Rydberg Blockade in Three-Atom Systems with Anisotropic Interactions* Phys. Rev. Lett. **112**(18) 183002 (2014).

[111] Boddeda R, Usmani I, Bimbard E, Grankin A, Ourjoumtsev A, Brion E and Grangier P *Rydberg-induced optical nonlinearities from a cold atomic ensemble trapped inside a cavity* Journal of Physics B: Atomic, Molecular and Optical Physics **49** 084005 (2016).

[112] Stefanucci G and van Leeuwen R Nonequilibrium Many-Body Theory of Quantum Systems (Cambridge University Press) cambridge Books Online (2013).

[113] Hofmann C S, Günter G, Schempp H, Müller N L M, Faber A, Busche H, Robert-de Saint-Vincent M, Whitlock S and Weidemüller M *An experimental approach for investigating many-body phenomena in Rydberg-interacting quantum systems* Frontiers of Physics **9** 571–586 (2014).

[114] Hodgson, Norman, Weber H Laser Resonators and Beam Propagation (Springer Series in Optical Sciences vol 108) (New York: Springer-Verlag) (2005).

[115] Brion E, Pedersen L H and Mølmer K *Adiabatic elimination in a lambda system* J. Phys. A: Math. Theor **40** 1033–1043 (2007).

[116] Vuletic V *Quantum networks: When superatoms talk photons* Nature Physics **2** 801–802 (2006).

[117] Guerlin C, Brion E, Esslinger T and Mølmer K *Cavity quantum electrodynamics with a Rydberg-blocked atomic ensemble* Phys. Rev. A **82** (2010).

[118] Tavis M and Cummings F W *Exact solution for an N-molecule-radiation-field Hamiltonian* Phys. Rev. **170** 379–384 (1968).

[119] Ourjoumtsev A *Coherent Interactions between optical photons using single atoms and atomic vapors* Memoire d'habilitation à diriger les recherches Institut d'Optique (2015).

[120] Das S, Grankin A, Iakoupov I, Brion E, Borregaard J, Boddeda R, Usmani I, Ourjoumtsev A, Grangier P and Sørensen A S *Photonic controlled-phase gates through Rydberg blockade in optical cavities* Phys. Rev. A **93**(4) 040303 (2016).

[121] Choi M D *Completely positive linear maps on complex matrices* Linear Algebra and Its Applications **10** 285–290 (1975).

[122] Jamiołkowski A *Linear transformations which preserve trace and positive semidefiniteness of operators* Reports on Mathematical Physics **3** 275–278 (1972).

[123] Gorshkov A V, Nath R and Pohl T *Dissipative Many-Body Quantum Optics in Rydberg Media* Phys. Rev. Lett. **110**(15) 153601 (2013).

[124] Carusotto I and Ciuti C *Quantum fluids of light* Rev. Mod. Phys. **85**(1) 299–366 (2013).

[125] Schine N, Ryou A, Gromov A, Sommer A and Simon J *Synthetic Landau levels for photons* Narure **534** 671–675 (2015).

[126] Steck D A *"Rubidium 87 D Line Data"* Available online at `http://steck.us/alkalidata` (2008).

[127] Zimmerman M L, Littman M G, Kash M M and Kleppner D *Stark structure of the Rydberg states of alkali-metal atoms* Phys. Rev. A **20**(6) 2251–2275 (1979).

Author's Publications

[1] Boddeda R, Usmani I, Bimbard E, Grankin A, Ourjoumtsev A, Brion E and Grangier P *Rydberg-induced optical nonlinearities from a cold atomic ensemble trapped inside a cavity* Journal of Physics B: Atomic, Molecular and Optical Physics **49** 084005 (2016).

[2] Grankin A, Brion E, Bimbard E, Boddeda R, Usmani I, Ourjoumtsev A and Grangier P *Quantum statistics of light transmitted through an intracavity EIT Rydberg medium* New Journal of Physics **16** 1–15 (2014).

[3] Grankin A, Brion E, Bimbard E, Boddeda R, Usmani I, Ourjoumtsev A and Grangier P *Quantum-optical nonlinearities induced by Rydberg-Rydberg interactions: A perturbative approach* Phys. Rev. A **92**(4) 043841 (2015).

[4] Das S, Grankin A, Iakoupov I, Brion E, Borregaard J, Boddeda R, Usmani I, Ourjoumtsev A, Grangier P and Sørensen A S *Photonic controlled-phase gates through Rydberg blockade in optical cavities* Phys. Rev. A **93**(4) 040303 (2016).

[5] Bimbard E, Boddeda R, Vitrant N, Grankin A, Parigi V, Stanojevic J, Ourjoumtsev A and Grangier P *Homodyne Tomography of a Single Photon Retrieved on Demand from a Cavity-Enhanced Cold Atom Memory* Phys. Rev. Lett. **112**(3) 033601 (2014).

[6] Grankin A, Brion E, Boddeda R, Ćuk S, Usmani I, Ourjoumtsev A and Grangier P *Inelastic Photon Scattering via the Intracavity Rydberg Blockade* Phys. Rev. Lett. **117**(25) 253602 (2016).

université PARIS-SACLAY
ÉCOLE DOCTORALE
Ondes et Matière (EDOM)

Titre :Absorptive non-linearities using Rydberg excitations in a Cavity
Mots clés : Rydberg, Cavité, Atomes
Résumé : Le contrôle des états quantiques de la lumière est une étape nécessaire pour la transmission et le traitement quantiques des informations. Un nuage d'atomes froids constitue un milieu optiquement non-linéaire très intéressant pour créer et manipuler des états photoniques. Le sujet de cette thèse est l'étude expérimentale de telles non-linéarités, induites entre des photons optiques par leur couplage avec des atomes de Rydberg. Les états de Rydberg sont des états atomiques très excités (n>30), qui permettent de créer des interactions photon-photon par l'intermédiaire de leurs interactions dipôle-dipôle à longue distance (>10μm). Nous utilisons une cavité de faible finesse pour transformer ces interactions en effets observables sur un faisceau de très faible intensité, ce qui peut permettre de produire des états non-classiques de lumière.

Title :Absorptive non-linearities using Rydberg excitations in a Cavity
Keywords : Rydberg, Cavity, Atoms
Abstract : The control of quantum states of light is a necessary step for quantum information transportation and processing. Cold atomic memories are one of the prime candidates for storing and manipulating photonic states. This thesis is a study of optical non-linear effects created using Rydberg states. Rydberg states are highly excited states (n>30) of atoms, which are useful in realizing photon-photon interactions because of their long distance (>10μm) dipole-dipole interactions. We utilize a low finesse cavity to transform phase shifts into intensity correlations which would allow one to generate arbitrary non-classical states of light.

Université Paris-Saclay
Espace Technologique / Immeuble Discovery
Route de l'Orme aux Merisiers RD 128 / 91190 Saint-Aubin, France